



# materialstoday

[www.materialstoday.com](http://www.materialstoday.com)

APRIL 2012 | VOLUME 15 | NUMBER 4

## Take a closer look

Advanced materials characterization

Yugang Sun looks at  
nanoparticle kinetics

Don't stop using rare  
earths!

Michael Miller reflects  
on the future of APT

# Raman power

On the frontiers of research, **Raman** is gaining popularity due to its outstanding power and utility. Now we've tapped Raman user input to design even more flexible, uncomplicated instruments. Forensics, pharmaceutical and analytical labs can tailor their analyses, and arrive at fast, reliable answers without all the work. Put Raman to work for you, not the other way around. It's Raman where you're in charge.

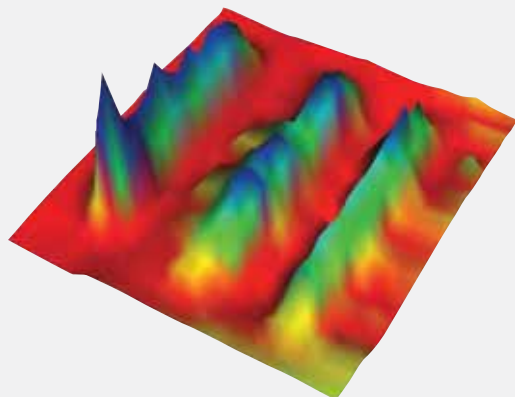
## without the work

• see the bold progress in Raman instruments at • [thermoscientific.com/raman](http://thermoscientific.com/raman)



### DXR Raman Microscope

- From our full line of Raman instruments
- OMNIC software family suite
- Patented automated data optimization
- Research grade performance



Germanium lines on Chromium ranging from 500 to 900nm wide

**Thermo**  
S C I E N T I F I C

**Published by**

Elsevier Ltd.  
The Boulevard, Langford Lane,  
Kidlington, OX5 1GB, UK

**Editorial**

Editor Stewart Bland  
E-mail: s.bland@elsevier.com  
Editorial Assistant Zara Preston  
E-mail: z.preston@elsevier.com  
Production Support Manager Lin Lucas  
E-mail: llucas@elsevier.com

**Advertising**

Advertisement Sales  
Guy Plowman  
E-mail: g.plowman@elsevier.com

**Free circulation enquiries**

Lucy Rodzynska  
E-mail: lucy.rodzynska@elsevier.com  
Elsevier Ltd.  
The Boulevard, Langford Lane,  
Kidlington, OX5 1GB, UK

**Subscription orders & payments**

*Materials Today* (ISSN 1369-7021) is published 10 times per year by Elsevier Ltd. The Boulevard, Langford Lane, Kidlington, OX5 1GB, UK

Price: €325 / US\$364 / ¥43,300  
Europe/ROW Tel: (+44) 1865 843434  
USA Tel: (+1) 314 447 8878

Online: www.materialstoday.com/magazine-subscription  
© Elsevier Ltd. 2012

All material published in *Materials Today* is copyright Elsevier Ltd.

Annual subscription price in the USA US\$ 325 (valid in North, Central and South America), including air speed delivery. Periodical postage paid at Rahway NJ and additional mailing offices.

Please send payment to: *Materials Today*

USA Postmaster send all USA address corrections to:

Customers in Europe, Middle East and Africa:  
Elsevier Ltd, Journals Customer Service & Fulfillment Department,  
The Boulevard, Langford Lane, Kidlington, OX5 1GB, UK  
Tel: (+44) (0) 1865 843434  
Fax: (+44) (0) 1865 843912  
Email: JournalsCustomerServiceEMEA@elsevier.com

Customers in Asia and Australasia:

Elsevier, Journals Customer Service & Fulfillment Department, 3  
Killiney Road # 08-01, Winsland House 1, SINGAPORE 239519  
Tel: (+65) 6349 0222  
Fax: (+65) 6733 1510  
Email: JournalsCustomerServiceAPAC@elsevier.com

Customers in the United States & Canada:

Elsevier, Journals Customer Service & Fulfillment Department,  
3251 Riverport Lane, Maryland Heights, MO 63043, USA  
Tel: (+1) 314 447 8878  
Toll: (+1) 877 839 7126  
Fax: (+1) 314 447 8077  
Email: Journalcustomerservice-usa@elsevier.com

Customers in Japan:

Elsevier, Journals Customer Service & Fulfillment Department,  
Higashi Azabu Bldg. 4F, 1-9-15 Higashi-Azabu, Minato-Ku,  
Tokyo, 106-0044 JAPAN  
Tel: (+81) 3 55615037  
Fax: (+81) 3 55615047  
Email: JournalsCustomerServiceJapan@elsevier.com

Periodicals postage is paid at Rahway, NJ and additional mailing offices.

Missing issues: Responsibility cannot be accepted by the Publishers after six months.

This journal and the individual contributions contained in it are protected under copyright by Elsevier Ltd, and the following terms and conditions apply to their use:

Photocopying: Single photocopies of single articles may be made for personal use as allowed by national copyright laws. Permission of the Publisher and payment of a fee is required for all other photocopying, including multiple or systematic copying, copying for advertising or promotional purposes, resale, and all forms of document delivery. Special rates are available for educational institutions that wish to make photocopies for non-profit educational classroom use.

Permissions may be sought directly from Elsevier Global Rights Department, P.O. Box 800, Oxford OX5 1DX, UK; phone: (+44) 1865 843830, fax: (+44) 1865 853333, e-mail: permissions@elsevier.com. You may also contact Global Rights directly through Elsevier's homepage (www.elsevier.com), by selecting 'Obtaining Permissions'.

In the USA, users may clear permissions and make payments through the Copyright Clearance Center, Inc., 222 Rosewood Drive, Danvers, MA 01923, USA; phone: (+1) (978) 7508400, fax: (+1) (978) 7504744, and in the UK through the Copyright Licensing Agency Rapid Clearance Service (CLARCS), 90 Tottenham Court Road, London W1P 0LP, UK; phone: +44 (0)20 7631 5555, fax: +44 (0)20 7631 5500. Other countries may have a local reprographic rights agency for payments.

Derivative Works: Subscribers may reproduce tables of contents or prepare lists of articles including abstracts for internal circulation within their institutions. Permission of the Publisher is required for resale or distribution outside the institution. Permission of the Publisher is required for all other derivative works, including compilations and translations.

Electronic Storage or Usage: Permission of the Publisher is required to store or use electronically any material contained in this journal, including any article or part of an article.

Except as outlined above, no part of this publication may be reproduced, stored in a retrieval system or transmitted in any form or by any means, electronic, mechanical, photocopying, recording or otherwise, without prior written permission of the Publisher.

Address permissions requests to: Elsevier Global Rights Department, at the mail, fax and e-mail addresses noted above. Notice: No responsibility is assumed by the Publisher for any injury and/or damage to persons or property as a matter of products liability, negligence or otherwise, or from any use or operation of any methods, products, instructions or ideas contained in the material herein. Because of rapid advances in the medical sciences, in particular, independent verification of diagnoses and drug dosages should be made.

Although all advertising material is expected to conform to ethical (medical) standards, inclusion in this publication does not constitute a guarantee or endorsement of the quality or value of such product or of the claims made of it by its manufacturer.

Printed by Headley Brothers Ltd, Kent, UK  
ISSN 1369-7021  
Journal number: 03069

# Dreams of electric sheep



## What's next for the virtual world?

Stewart Bland | Editor, *Materials Today* | s.bland@elsevier.com

Last month we hosted our third Virtual Conference here at *Materials Today*, focusing on the frontiers of microscopy. We'd like to thank all of the presenters, delegates, and sponsors who helped make the event a success. But if you weren't able to attend on the day, fear not, as all of the content will remain available to view for the next 12 months; just visit [www.materialstoday.com/virtualconference](http://www.materialstoday.com/virtualconference).

The virtual conference serves to raise the question of what aspect of scientific life will be the next to embrace the digital format, and make the virtual world its home? In our last issue [*Mater Today* (2012) 3, 78], Brian Owens commented on how the internet has completely transformed the way papers are published, and made open access feasible. There's no doubt that computers and the web have revolutionized the submission, distribution, and indexing of papers; speeding up the whole process and making locating papers easier. All (or perhaps almost all) journals now have electronic versions, with many only existing in a digital format.

But journals aren't alone in having made the transition to a principally electronic platform. Powerful, affordable computers, and the ability to connect over the web, have turned what would be prohibitively time and labor intensive methods into practical, fast analysis and modeling tools.

So what's next, and will the effect be as profound as the areas discussed above? Given the rise in social media, perhaps lectures and tutorials could become fully virtual affairs. Lectures can be recorded and played back online, and by integrating these presentations with interactive elements and supplementary materials, it's possible to produce the kind

of virtual conferences we host here at *Materials Today*. And for smaller meetings, it's not uncommon to use telepresence systems. However, it's hard to imagine that these solutions could ever completely replace actual meetings, as they lack some of the intimacy of physical encounters; which can be critical in an area where communication is key.

At any rate, given the pace at which online environments evolve, we may not have long to wait until we experience the next leap forward.

Whether you're reading this month's issue of *Materials Today*, online, via our iPad app, or in good old print, we hope you'll find the content equally engaging. Following on from the conference on microscopy, this issue of the magazine takes a look at a range of characterization techniques. Yugang Sun and Harald Ade discusses how novel x-ray techniques can be used to study nanoparticle dynamics and image synthetic organic materials, respectively. Mike Miller considers the future of atom probe tomography and the prospect of examining every atom in a sample. And branching out, Shelley Minter discusses new materials for bio-fuel cells.

Finally on a separate note, I'd like to take this opportunity (on behalf of everyone here at *Materials Today*) to say farewell to our outgoing Editor, Jonathan Agbenyega, and wish him the best of luck in his new position.

### Editorial Advisory Panel

Caroline Baillie  
Queens University, Canada

Zhenan Bao

Stanford University, USA

Alejandro Lopez Brisenio

University of Massachusetts, USA

Chris Ewels

CNRS, France

Alan Heeger  
University of California, USA

Suwan Jayasinghe

University College London, UK

Mark Johnson

Naval Research Laboratory, USA

David Kisailus

University of California

Steven Lenhart  
Florida State University, USA

Tae Won Noh

Seoul National University, Korea

Aleksandr Noy

University of California, USA

Stephen Pearton

University of Florida, USA

David N. Seidman  
Northwestern University

Helena Van Swygenhoven

Paul Scherrer Institute, Switzerland

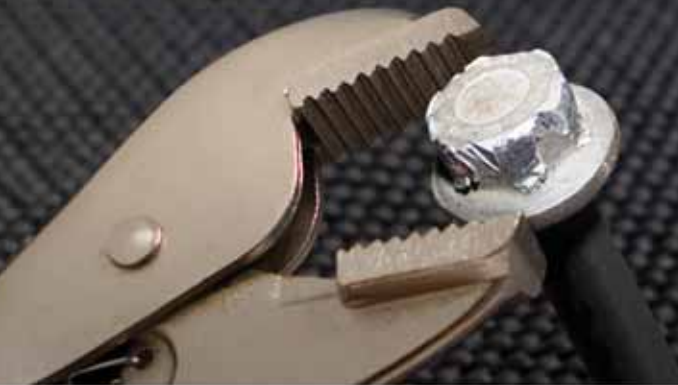
George Whitesides

Harvard University, USA

Jackie Yi-Ru Ying

Institute of Bioengineering and Nanotechnology, Singapore

# One Tool Does Not Fit All



## Get the Right Tools for the Job

More AFM techniques for nanomechanics



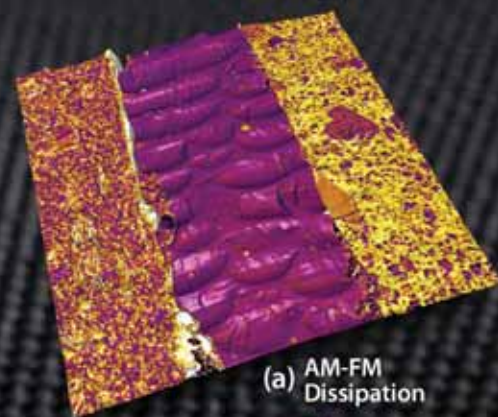
## Introducing the NanomechPro™ Toolkit

Accurate tools to reveal intrinsic properties of diverse materials

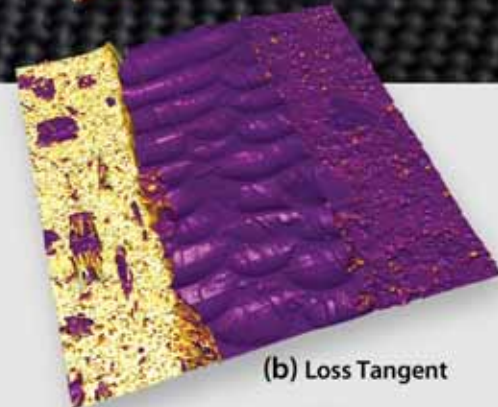
See our Webinar May 23 – Register at [www.AsylumResearch.com/webinars](http://www.AsylumResearch.com/webinars)  
*“Opportunities, Challenges and Frontiers of Nanomechanical Measurements”*



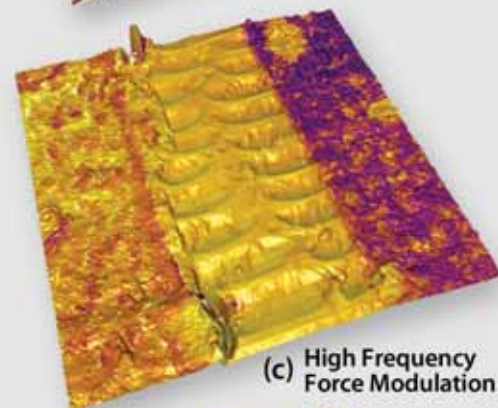
The Technology Leader in Scanning Probe and Atomic Force Microscopy  
[sales@AsylumResearch.com](mailto:sales@AsylumResearch.com) | 805-696-6466 | [www.AsylumResearch.com](http://www.AsylumResearch.com)



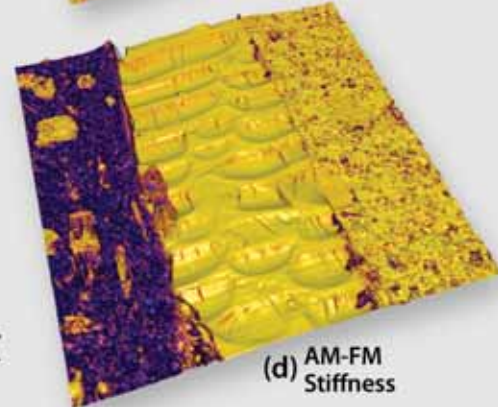
(a) AM-FM Dissipation



(b) Loss Tangent



(c) High Frequency Force Modulation



(d) AM-FM Stiffness

Images of a Viton®/epoxy/EPDM (left to right) sandwich. The tip-sample dissipation measured by AM-FM is shown in (a) and the quantitative loss tangent data shown in (b) clearly indicates the higher loss modulus of the Viton. The elasticity is measured with two independent techniques in (c) and (d), both of which resolve the subtle difference in the elastic moduli of the Viton (40MPa) and the EPDM (43MPa).

# Contents

materialstoday

## Regulars

### ■ Editorial 129

Dreams of electric sheep  
What's next for the virtual world?

### ■ Comment | Frances Wall 134

Don't stop using rare earths  
It's not a question of limited natural resources, it's just a matter of time.

### ■ News 136

From coffee grounds to quantum dots | New handheld imaging devices just over the rainbow | Laser beam technology to detect explosives | Liquid power for your PC and phone | E. coli detection? there's an app for that! | Breakthrough could benefit spintronic performance | Nanocrystal diodes for medicine | Refuting the Shuttleworth equation

### ■ Uncovered | Sergey V. Balakhonov *et al.* 175

An inorganic puzzle

This month's cover image features an SEM micrograph of a vanadia aerogel. Balakhonov *et al.* explain why these materials may be the key to the future of miniature Li-ion cells.

*Sergey V. Balakhonov, Eugene A. Goodilin, Anton I. Gavrilov, Daria Y. Gavrilova, and Bulat R. Churagulov*

### ■ Events diary 176

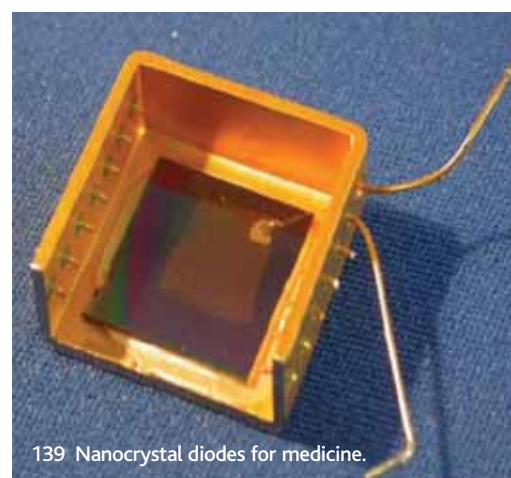
This year's cover competition is brought to you in association with Carl Zeiss. Visit [www.zeiss.com/nts](http://www.zeiss.com/nts).



136 From coffee grounds to quantum dots.

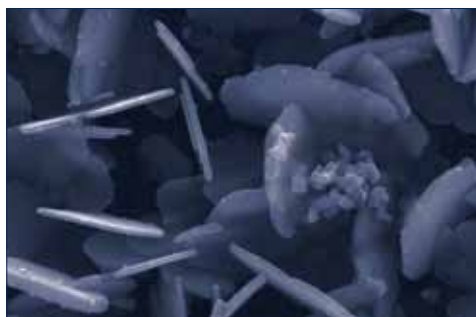


138 E. coli detection? There's an app for that!



139 Nanocrystal diodes for medicine.

## Research

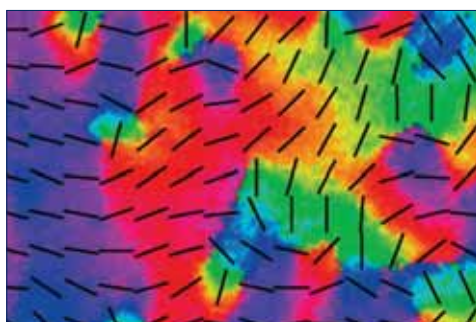


### ■ Review 140

#### Watching nanoparticle kinetics in liquid

Real-time monitoring of the reaction kinetics involved in nanoparticle growth and transformation in liquid environments is crucial for understanding the complex chemical and physical events associated with nanophase evolution. Yugang Sun takes a look at novel x-ray scattering techniques, highlighting their capabilities for studying the dynamic processes of nanoparticles

*Yugang Sun*

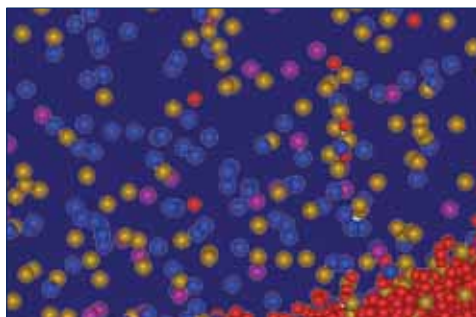


### ■ Review 148

#### NEXAFS imaging of synthetic organic materials

Watts and Ade illustrate the basic operating principles of near edge x-ray absorption fine structure spectroscopy (NEXAFS) spectroscopy, scanning transmission x-ray microscopy, and resonant soft x-ray scattering, with a focus on applications involving semi-conducting polymers.

*Ben Watts and Harald Ade*

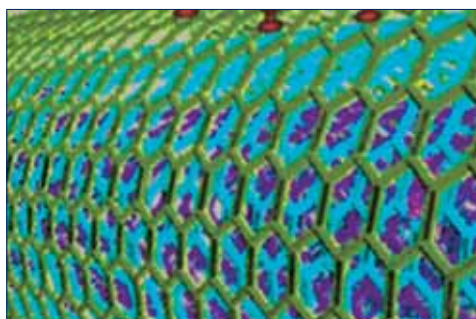


### ■ Review 158

#### The future of atom probe tomography

The dream of the microscopy and materials science communities is to see, identify, accurately locate, and determine the fundamental physical properties of every atom in a specimen. The technique of atom probe tomography is the closest to fulfilling this dream but is still significantly short of the goal. Here, Miller *et al.* consider the future of atom probe tomography, and the prospects for achieving this ultimate goal.

*Michael K. Miller, Thomas F. Kelly, Krishna Rajan, and Simon P. Ringer*



### ■ Review 166

#### New materials for biological fuel cells

Major improvements in biological fuel cells over the last ten years have been the result of the development and application of new materials. These new materials include: nanomaterials, materials that provide improved stability, materials that increase the conductivity and surface area of the electrodes, and materials that aid facile mass transport. Minteer and co-workers describe how this progress has improved the performance of biological fuel cells to yield feasible technologies.

*Shelley D. Minteer, Plamen Atanassov, Heather Luckarift, and Glenn Johnson*

A close-up of a Bruker detector probe, showing the "BRUKER" logo and a "123 eV" label.

# QUANTAX – Ultimate EDS for SEM and TEM



- Data collection at the highest speed and at the best resolution you can get – first class results no matter the circumstance
- Excellent light element performance with Mn  $K\alpha \leq 123$  eV (F  $K\alpha \leq 54$  eV, C  $K\alpha \leq 46$  eV) even at 100,000 cps
- Best acquisition conditions for sensitive and rough samples through unique multi-detector systems and optimum geometry using VZ-Adapters
- Genuine standardless P/B-ZAF quantification for rough samples and VZ applications, Cliff-Lorimer quantification for TEM

[www.bruker.com/microanalysis](http://www.bruker.com/microanalysis)

# Don't stop using rare earths



## It's not a question of limited natural resources, it's just a matter of time

Professor Frances Wall | University of Exeter, Cornwall Campus | f.wall@exeter.ac.uk

Don't stop using rare earths – that is the message from me as a geologist. Although the headlines recently have been about supply restrictions, volatile prices, and a rush to find substitutes; on behalf of the geological community, I can reassure materials scientists that there are plenty of rare earths and a wide variety of potential new deposits. It is just a matter of patience (please) whilst the challenges of developing new deposits are overcome.

Rare earth elements (scandium, yttrium and the 15 elements of the lanthanide series) are used in a wide range of environmental technologies. Examples include low energy light bulbs, catalytic converters and magnets in large wind turbines<sup>1</sup>. Rare earths also turn up inside every computer, mobile phone, and TV. The applications of rare earths rely on distinct properties that result from their complex electronic structures and so substitution is difficult. Despite the fact that rare earths have so many applications, most of them require only small amounts of material and the global market, of about 130 000 tonnes per year, is small compared with more common metals, such as copper or zinc.

Rare earths and several other so-called 'technology metals' are required in such small quantities that they come from only a few mines, and one or two countries in the world. If supply were to be disrupted, even at just one mine, world supply could be seriously affected. The European Union published a report in June 2010 correlating uses and the difficulty of substitution with supply risk, and this led to the definition of fourteen materials as 'critical' for Europe<sup>2</sup>. Rare earths (counting as one of the fourteen) are high on the critical list. Other critical materials include platinum group elements, tungsten, niobium and tantalum. To compound the problem, recycling rates of many of these metals are low.

So, coming back to my headline, there are plenty of potential economic deposits of rare earths, in alkaline igneous rocks and carbonatites, hydrothermal veins, sedimentary placers, as by-products of fertilizer production, or reworking of mineral wastes, and,

looking further to the future, from ocean floor deposits. So why then are there problems with supply? Well, the answer is that although there are many potential deposits to consider (822 according to one report<sup>3</sup>) it is not easy to bring them to production. Whilst China was supplying cheap and plentiful rare earths, there was little incentive for companies to explore or develop new deposits, or even to keep running existing mines, and we have reached a stage where China supplies 97 % of the world's requirement. Following the restriction of exports from China, and the rise in prices, there are now hundreds of rare earth exploration projects, and two mines, at Mountain Pass, USA and Mt Weld, Western Australia, on their way to full production. Mountain Pass was for many years the World's main supplier of rare earths; Mt Weld is a new mine.

Exploration and development teams looking for new deposits have a number of challenges to overcome. Challenges in addition to the usual technical, financial, environmental, and social constraints of setting up a new mine! The first is that although the rare earths form a series, most deposits contain large amounts of the light rare earths, lanthanum and cerium, which are as abundant in the crust as copper<sup>4</sup>. Finding geological environments that produce high concentrations of the less abundant, higher atomic number 'heavy rare earths' is much more difficult. Another geological problem is that individual rare earths do not form minerals (let alone ore deposits) of their own. For example, dysprosium may be particularly valuable at the moment but there are no known dysprosium minerals. Instead, dysprosium sits alongside yttrium, which is far more abundant, in other minerals such as xenotime (YPO<sub>4</sub>), or is adsorbed in small amounts onto clays with other similar heavy rare earths. A third challenge is that the radioactive elements thorium and uranium often substitute into rare earth minerals. The handling of radioactive ores or the generation of radioactive waste is not desirable. Some deposits of the rare earth mineral, monazite, are not mined for

this reason. Predicting which geological environments will concentrate rare earths but select against thorium and uranium is an important role for geologists. Moving on to mineralogy, there is the challenge that some deposits contain minerals that have not been commercially exploited before. I now have an excuse to list some exotic sounding mineral names, here goes: ancylite, eudialyte, and steenstrupine, all require new metallurgical processes for beneficiation and extraction. The subsequent separation of the rare earths from each other is also a difficult process; some methods contain 1000 steps! Innovation here is also crucial to widening the number of potential suppliers.

Few economic geologists have studied such 'strange' elements as the rare earths. However, we now find materials scientists are using a wider range of these kinds of elements in new technologies. It is timely to pay more geological attention to a wider range of elements. The Natural Environment Research Council has published a Theme Action Plan that includes security of supply of minerals and will be encouraging more research. Elements such as the rare earths are, however, unlikely to secure the interest of the multinational mining companies. The markets are still too small. Support is coming from higher up in the supply chain, with more vertical integration from mines to manufacturers, encouraging links from geologists through to materials scientists.

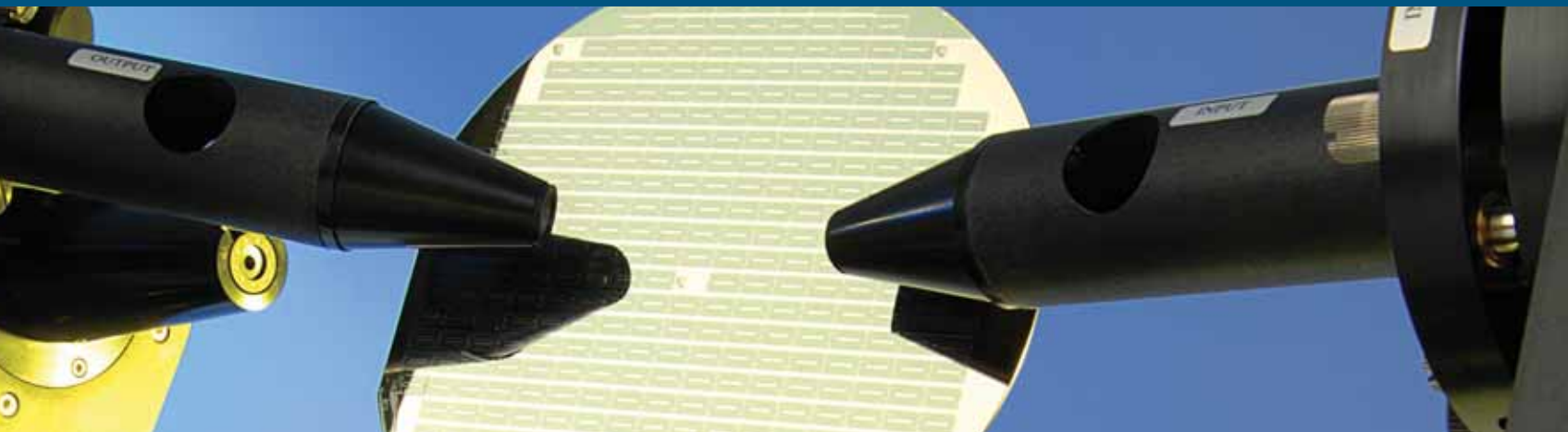
### FURTHER READING

1. Rare Earth Elements Mineral Profile (2011), British Geological Survey, Keyworth, Nottingham, UK, [www.mineralsUK.com](http://www.mineralsUK.com), 54 pp.
2. Critical raw materials for the EU. (2010) The *ad-hoc* Working Group sub-group of the Raw Materials Supply Group, European Commission, June 2010, 85 pp. [http://ec.europa.eu/enterprise/policies/raw-materials/files/docs/report-b\\_en.pdf](http://ec.europa.eu/enterprise/policies/raw-materials/files/docs/report-b_en.pdf)
3. Orris, G.J. and Grauch, R.I. (2002) Rare Earth Element Mines, Deposits, and Occurrences USGS Open-File Report 02-189.
4. Geological Society (2011) Rare Earth Elements Briefing Note 13 pp [www.geolsoc.org.uk/ree](http://www.geolsoc.org.uk/ree)



# J.A. Woollam Co., Inc.

Ellipsometry Solutions<sup>sm</sup> for your Thin Film Characterization.



J.A. Woollam Co. has the world's widest variety of **Spectroscopic Ellipsometers** with **8** different models to non-destructively characterize thin film thickness and optical constants. After twenty-four years, over **15,000** samples characterized in our lab, and over **140** patents – we are the Ellipsometry Experts.

Ellipsometry Solutions



### alpha-SE<sup>®</sup>

A great solution for routine measurements of thin film thickness and refractive index. Designed for ease-of-use: simply mount a sample, choose the model that matches your film, and press "Measure". Results are yours within seconds.



### AccuMap-SE<sup>®</sup>

Characterize thin film uniformity of large panels with ease. The AccuMap-SE combines a high-speed M-2000 ellipsometer, wide spectral range, and fast mapping for large panels. Perfect for photovoltaic or flat panel display thin films.



### M-2000<sup>®</sup>

The M-2000 line of ellipsometers is engineered to meet the diverse demands of thin film characterization. An advanced optical design, wide spectral range, and fast data acquisition make it extremely powerful for in situ, in-line and ex situ applications.



### VASE<sup>®</sup>

The VASE is our most accurate and versatile research ellipsometer for all types of materials: semiconductors, dielectrics, organics, metals, multi-layers, and more. Now available with the widest spectral range from ultraviolet to infrared.

## From coffee grounds to quantum dots

### NANOTECHNOLOGY

Until recently perhaps the best use for used coffee grounds was the lowest of low-tech: to top up the compost pile. Now, researchers in Taiwan have used the waste material as a novel carbon source for synthesizing high-tech nanodots. The developers suggest that approach could be a viable alternative to semiconductor quantum dots that might be used as photoluminescent materials for sensing, imaging, in photovoltaic solar cells and in optoelectronic devices [P-C Hsu *et al.*, *Green Chem* (2012) doi: 10.1039/c2gc16451e].

Huan-Tsung Chang of the National Taiwan University, Taiwan and colleagues have obtained carbon-dots with an average diameter of about 5 nanometres, which provide a quantum yield of 3.8 %. The team has tested the viability of these materials in cell imaging studies and surface-assisted laser desorption/ionization-mass spectrometry (SALDI-MS) of important proteins, including insulin and angiotensin I.

Quantum dots have gained enormous visibility in recent years as photostable materials for use in putative optoelectronics devices and other applications, including sensing and imaging for biomedical research, environmental monitoring and medical diagnostics. However, the toxic heavy



metal cadmium is the usual base for selenide and sulfide semiconductors in this field. As such, there are numerous safety and environmental concerns regarding these early quantum dots not least in medical applications.

Various approaches, such as coating quantum dots with a polymer or developing gold and silver alternatives, have been investigated as alternatives to cadmium semiconductors. Finding alternatives that retain the strong emission profile, are stable, and inexpensive remains high on the agenda. Of course, little can be as cost effective as re-using waste material and so it was that Chang and colleagues turned to used coffee grounds to make carbon nanodots. Other

researchers have exploited graphite powders, oxidation of nanotubes and other materials for making C-dots. The Taiwanese team found that grinding, dehydration, polymerization, and carbonization of coffee grounds were sufficient to produce C-dots in large quantities.

Spectroscopic and x-ray analysis as well as high-resolution electron microscopy revealed the nature of their C-dots and the broad range of sizes produced (averaging 5 nm +/- 2 nm. The emission spectra of the C-dots range from blue (400 nm wavelength) to red (600 nm), depending on the wavelength of the incident excitatory light.

The team describes their approach to C-dots as "green" not only because it recycles a waste materials but also because it avoids the strong acid and passivation steps needed in other approaches to these materials.

"The C-dots can be further used to prepare sensors, drugs, and catalysts," Chang told *Materials Today*. "For example, we can conjugate C-dots with various aptamers for sensing of metal ions, proteins, and DNA." He adds that functionalised C-dots might also be used to target cancer cells for imaging and therapy.

David Bradley

## New handheld imaging devices just over the rainbow

### POLYMERS AND SOFT MATERIALS

Scientists at the University at Buffalo have developed a rainbow-colored polymer that could help bring about a new generation of portable, multi-spectral imaging devices. Their one-step, low-cost approach fabricates a polymer that, from a single viewing angle, is seen to be rainbow-colored and able to reflect many different wavelengths of light, mimicking the structured color already present in nature, such as in the wings of butterfly and peacock feathers.

The method, outlined in *Advanced Materials* [Liu, *et al.* *Adv Mater* (2012) doi: 10.1002/adma.201104628], could directly lead to new imaging devices that can identify the true color of different objects. Team leader Alexander Cartwright said "Such portable technology could have applications in a wide range of fields, from home improvement, like matching paint colors, to biomedical imaging, including analyzing colors in medical images to detect disease."

The single-step fabrication approach involved positioning a photosensitive pre-polymer syrup between two glass slides, before aiming a laser beam through a curved lens



placed above the solution. The lens separated and bent the beam into light of continuously varying wavelengths. When the light hits the syrup, monomers in the solution start combining into polymers, forming a continuous pattern of structures forming ridges, with the bigger ridges arising where the light hits with the greatest intensity. What remains is a thin filter that is rainbow-colored when viewed under white light, due to the periodic polymer layers reflecting a continuous spectrum of colors.

The team, having worked on nanostructured optical elements, was keen to develop a structure that

provided broadband optical response in a single and compact structure from the same viewing angle. Such structures are in the holographic patterns of credit cards and driving licenses, where different colors can be seen depending on the observation angle. The novel and simple concept of integrating multiple reflection filters in a very compact manner uses a designed pattern for the fabrication process, so that it is possible to develop functional photonic elements to manipulate light flow that offers potential for transformation optics.

The team now hopes to apply the research in miniaturized spectral analysis, biomedical sensing, biomimetic photonics, and anti-counterfeiting techniques. The technique used is scalable, allowing for filters of different sizes to be developed by shining the laser through lenses of different sizes. They will now try to improve the quality of the low-cost rainbow filter, and look at ways of integrating it with portable electronic devices such as laptops and cell phones, to realize the idea of handheld spectroscopic analyzers.

Laurie Donaldson

## Laser beam technology to detect explosives

### OPTICAL MATERIALS

A team of scientists at the Vienna University of Technology in Austria has presented a new method for detecting enclosed chemicals and explosives from a distance of over 100 meters. The approach uses the light from laser beams to look through non-transparent container walls, and could offer a range of military and security applications, as the laser light can be scattered in a specific way by different substances.

The new technology uses Raman spectroscopy to produce a chemical fingerprint where a sample is irradiated with a laser beam and the light is scattered by the molecules of the sample. Such an action alters the light's wavelength, and also therefore its color; the color spectrum of the resulting scattered light bouncing off the individual molecules can then be analyzed, yielding information about molecular vibrations in the material.

As the hundreds of millions of photons hit a sample, they are scattered uniformly in all directions; only a



small number actually penetrate the sample container and trigger a Raman-scattering process in the sample. However, with a highly efficient telescope and extremely sensitive light detector, the team was able to determine which molecules are from the light signal of the container as opposed to that of the sample inside. As the light entering the container is scattered over a much larger area, they achieved this by directing the laser beam onto a small, well-defined spot, so that the light signal emitted from the container comes from just a small area

and not the container itself. As researcher Bernhard Lendl points out, "The challenge is to distinguish the container's light signal from the sample signal."

In this EU-funded study, the scientists collaborated with private companies as well as interested parties involved in public safety, such as the Austrian military and the Spanish Guardia Civil, with the more hazardous testing on commonly used explosives even being carried out on military sites.

It is hoped the new approach could find a range of applications in the military and in airport security, but also be more widely used to identify substances where it is difficult to get sufficiently close to the subject, such as in the study of icebergs or for geological analysis in space research. In addition, the chemical industry could also show an interest in exploring other possible applications.

**Laurie Donaldson**

## Liquid power for your PC and phone

### ENERGY

Liquid crystals comprising alternating layers of hydrophobic and hydrophilic materials can act as a framework for a new kind of liquid photogalvanic cell. Devices based on such an approach could be more than five times as cost effective as photovoltaic solar cells, according to the system's UK developers. Moreover, the same system can act as an electrochemical capacitor for high voltage installations [Halls, J. E., and Wadhawan, J. D., *Energy Environ Sci* (2012) doi: 10.1039/c2ee03169h].

The bane of our modern digital lives is the limited capacity of the ubiquitous rechargeable batteries we carry in almost every portable electronic gadget from smart phone and digital camera to media player and tablet PC. Moreover, from the manufacturing perspective, solid lithium batteries are effectively limited to construction as solid rectangular blocks precluding more imaginative device form factors.

Efficient, readily rechargeable and lightweight power sources that could be molded to fit whatever geometry and volume a designer requires could revolutionize the industry, especially if they could be recharged using sunlight.

Now, Jonathan Halls and Jay Wadhawan of the University of Hull, UK, have developed just such an alternative. They have sandwiched a photoredox-active



*Liquid power. Courtesy of Jonathan Halls.*

material embedded within a non-ionic surfactant subphase and a second redox reagent in the aqueous pseudophase of a lamellar lyotropic liquid crystal framework between two electrodes. This system is what

the team refers to as quasi-biphasic and represents an entirely new concept for electrochemical cells based on electron transfer rather than ion transfer.

The team has demonstrated that the system, under violet light, acts as a photogalvanic device. The maximum light-to-electrical power conversion efficiency is about 2 %, the team says. The fill factor, the ratio of maximal power to the product of open-circuit voltage and short-circuit current is 15 %. Moreover, it has the ability to act as an electrically rechargeable electrochemical capacitor of voltage with a power efficiency of 80 % and an energy density of 1 W h per kg at a power density of 1 kW per kg. "The next stage in this work is to increase power conversion efficiency and to use more of the visible light spectrum, especially close to green light whilst simultaneously improving the energy density of these systems, so that they can perform either as energy storage media, or solar-to-electrical conversion systems directly," Wadhawan told *Materials Today*. "We are confident that we can do this, work is currently being written up which shows almost a doubling of the power conversion efficiency, with backing via analysis through mathematical modeling of the system."

**David Bradley**

## E. coli detection? There's an app for that!

### TOOLS AND TECHNIQUES

US researchers are exploiting the unique properties of a mobile phone camera to detect the pathogenic bacterium *Escherichia coli* in food and drink samples with the aim of developing a quick and easy testing system for water- and food-associated diseases. A compact and cost-effective device hooked up to the mobile phone could be of great use in the developing world where there is an ongoing need for sensitive, portable and inexpensive testing tools. [Zhu, H., *et al.*, *Analyst* (2012) doi: 10.1039/c2an35071h] Aydogan Ozcan and colleagues at the University of California, Los Angeles have developed an attachment for a mobile phone based on a quantum dot based assay that exploits the phone's camera as a fluorescent microscope to detect bacteria. The device carries antibodies to *E. coli* O157:H7 in functionalized glass capillaries with a quantum dot payload. The antibodies attach to any bacteria in a liquid sample and bring with them the quantum dots. Battery-powered light-emitting diodes (LEDs) excite/pump the particles and emission is readily detected by the camera unit through an



*E. coli, on hold. The desktop detection kit. Ozcan Research Group at UCLA, <http://innovate.ee.ucla.edu/>.*

additional lens placed between the capillary and the camera lens.

The team has tested the technology using samples spiked with *E. coli*, a potentially lethal pathogen that can cause irreparable kidney damage even at very low initial levels of contamination. They found that by quantifying the fluorescent light emission from each capillary tube they are able to determine the concentration of *E. coli* in a given sample.

The approach utilizes the benefits of quantum dot fluorescence, which the team explains is brighter and more stable than traditional organic dyes, and combines this with existing mobile phone technology and software to provide an inexpensive and portable test kit for pathogenic bacteria. The antibodies used need only be modified to offer detection of other pathogens. While high-tech laboratories are not necessarily accessible in the developing world, mobile phones have become an almost ubiquitous technology even in remote, rural areas where they serve not only the primary function as communication devices, but represent the currency of a barter system across certain parts of Africa and elsewhere. As such, access to mobile phones is far less limited and would not represent an additional investment to enable this technology for testing food and water.

"As for the next steps, there is a start-up company (<http://holomic.com>) that aims to commercialize this platform," Ozcan told *Materials Today*.

**David Bradley**

## Breakthrough could benefit spintronic performance

### MAGNETIC MATERIALS

A new study has apparently resolved a long-standing issue over the use of the semiconductor gallium manganese arsenide (GaMnAs) that could lead to major improvements in the performance of spintronic devices. With a focus on the use of electron spin rather than charge, smaller, faster and cheaper devices could one day be produced for storing and processing data.

In semiconductor electronics, electron properties are crucial, and characterized by either charge or spin. To date, semiconductor device applications have benefitted from the charge, although many researchers have been exploring the possibility of harnessing electron spin to increase functionality in computer memory and information processing. Now scientists from the Lawrence Berkeley National Laboratory and Notre Dame University in the US, whose work was published in the journal *Nature Materials* [Dobrowolska *et al.*, *Nature Materials* (2012) doi: 10.1038/nmat3250], have shown that the spintronic properties of GaMnAs are due to holes in an impurity band created by manganese doping, which depletes the valence band as well as shifting



the Fermi level. The team revealed that the holes, positively charged spaces, in GaMnAs are positioned in an impurity energy band not a valence energy band, as previously believed.

When some of the gallium atoms in gallium arsenide are swapped with manganese atoms, this produces a ferromagnetic semiconductor that works well in spintronic devices. For semiconductors, as well as other solid-state materials, the valence band is the range of energies in which the movement of charge is resolved by the presence of holes. When gallium arsenide is doped with manganese it can bring about an impurity band that reduces the valence band and moves the *Fermi level* (the energy level below which the electronic

states are filled). They achieved the breakthrough by monitoring the concentrations of manganese atoms and holes relevant to the ferromagnetic order in GaMnAs, before integrating their findings with magnetization, transport and magneto-optical data. The results offer the potential for fabricating GaMnAs to extend the width and occupation of the impurity band, which would improve the Curie temperature and therefore the spintronic potential.

If electronic and magnetic properties can be combined in one integrated device, it would provide a greater functionality and could make miniaturization easier. With GaMnAs being both a semiconductor and a ferromagnet, it is an ideal material for achieving this goal. The team now aims to improve the understanding of materials where the electron spin plays a crucial role, and which can be used in spintronic applications. The researchers are also looking into increasing the Curie temperature of GaMnAs to above room temperature, and manipulating the defects that occur in the lattice of GaMnAs, such as interstitials and antisites.

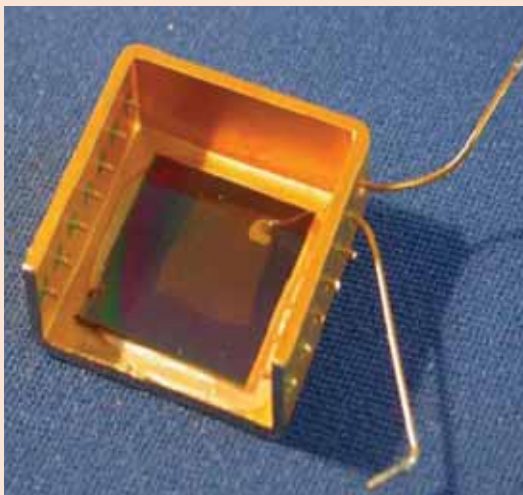
**Laurie Donaldson**

## Nanocrystal diodes for medicine

### NANOTECHNOLOGY

Considerable research time has been dedicated to designing light-emitting diode (LED) devices that can be applied in biomedical diagnostics and medical devices; the holy grail has been to produce them cheaply and so that they can be integrated into existing technologies. Now a new study, by scientists at the Los Alamos National Laboratory and colleagues at the University of Milano–Bicocca in Italy, has pushed back the boundaries of nanocrystal science by producing a new glass-based, inorganic material that can emit light in the ultraviolet spectrum and be integrated onto silicon chips common in most electronic technologies.

The team, whose work has been published in *Nature Communications* [Brovelli *et al.*, *Nature Comms* (2012) doi: 10.1038/ncomms1683], developed a process for creating such nanocrystal LEDs that produce light in the ultraviolet range and have the potential to become implantable products. It is hoped that the devices could be fabricated cheaply and robustly, and be sufficiently scalable for use in activating specific light-sensitive drugs to improve medical treatment, as active components of wearable health monitors and even for identifying fluorescent markers in medical diagnostics. The new synthesis strategy allows for the production of the LEDs through a wet-chemistry



*The nanocrystal device.*

approach involving simple chemical reactions, and which emits in the ultraviolet range due to how the nanocrystals are embedded in the glass. The devices have both chemical inertness and the mechanical stability of glass, as well as having electric conductivity and electroluminescence, allowing them to be utilized in difficult environments, including in bodily implants and immersion into physiologic solutions. With regular LEDs, the light emission occurs at the interface between two semiconductors; however, with this design the material is

produced to act as an ensemble of semiconductor junctions distributed in the glass, with the active part consisting of tin dioxide nanocrystals that have been overlaid with a shell of tin monoxide embedded in standard glass. When the thickness of the shell is tuned, the electrical response of the whole material can be manipulated. Incorporating the tin dioxide nanocrystals in silica has been useful for the research, and required the design of new synthesis routes starting from molecular precursors. This was achievable because the solubility of tin in silica is so low that the use of conventional melting processes results in the complete precipitation of tin. The group therefore designed a modified sol-gel synthesis procedure that allows for the controlled segregation of tin oxide nanocrystals in a glass matrix.

The next task is to optimize the material and device structure, crucial to moving from proof of principle to practical application, and they are also looking to exploit the other features of the nanostructured glasses, such as its photorefractivity. The team feels that the oxide-in-oxide motif is only a small part of its potential, and plan to explore how the concept can also be applied to other materials of different structure and composition.

Laurie Donaldson

## Refuting the Shuttleworth equation

### SURFACE SCIENCE

For over 60 years it has been believed that there is excess surface tension on a solid material in a similar way to that on a liquid, as described by the Shuttleworth equation. However, in 2009, two Finnish scientists, Lasse Makkonen and Kari Kolari, and a British colleague, David Bottomley, presented a paper in the journal *Surface Science* that claimed the long-held equation about the relation between surface tension and surface energy on an unstrained solid wasn't actually compatible with thermodynamics, which provoked a fair amount of controversy in the field.

Now Lasse Makkonen, a researcher at the VTT Technical Research Centre of Finland, has published a study in *Scripta Materialia* [Makkonen, L., *Scripta Mat* (2012) doi: 10.1016/j.scriptamat.2012.01.055], which has returned to the subject to revise our understanding of surface tension on solids, claiming that this finally closes the debate on the applicability of the equation. His new

study has mathematically shown that the Shuttleworth equation reduces to the definition of surface tension derived from mechanics, and that surface tension on a solid material is unconnected to the energy needed to create a new, unstrained surface. Consequently, the excess surface tension on a solid does not really exist as we usually understand the concept.

In showing mathematically that the Shuttleworth equation reduces to the definition of mechanical surface stress, Makkonen argues instead that the existence and nature of surface tension on a solid should only be assessed by molecular dynamics at the surface layer.

As a geophysicist by background, Makkonen originally came across the Shuttleworth equation in a book on applied surface thermodynamics in 1998, thinking then that there was a potential problem with the equation. He returned to the problem in a 2002 study

and then again later when he realized that he was not the only one to have doubts about the veracity of the equation. As he points out, his new paper is intended to "remove from people's mind the false analogy between the surface tension of a solid and that of a liquid. In fact, in the traditional sense, surface tension does not exist on a solid, and this is important to understand conceptually."

Makkonen hopes that this development will be useful in achieving a better understanding of phenomena in micromechanics and electrocapillarity, and perhaps lead to new interpretations of some microelectronic measurements, thus improving the measurement technology in that field. He now expects to leave such problems of surface stress to others, and return to his usual role in researching the use of thermodynamics in modeling micro- and nanoscale phenomena.

Laurie Donaldson

# Watching nanoparticle kinetics in liquid

Real-time monitoring of reaction kinetics involved in nanoparticle growth and transformation in liquid environments is crucial for understanding the complex chemical and physical events associated with nanophase evolution. Accordingly, *in situ* techniques that can “see through” liquids to probe nanomaterial variation are in high demand, as they will help us understand reaction mechanisms and design better synthetic strategies for building nanoparticles with precisely tailored properties. In this review, *in situ* transmission x-ray microscopy and time-resolved high-energy x-ray scattering techniques are discussed, highlight their capabilities in studying the dynamic processes of nanoparticles.

Yugang Sun\*

Center for Nanoscale Materials, Argonne National Laboratory, 9700 South Cass Avenue, Argonne, IL 60439, USA

\*E-mail: ygsun@anl.gov

Scalable solution-phase synthesis of colloidal nanoparticles with precisely tailored properties represents the most critical foundation towards implanting nanoscale science and technology in a variety of areas related to energy and the environment, such as catalysis, solar energy conversion, energy storage, etc.<sup>1-6</sup>. The properties of a nanoparticle are determined by a set of physical parameters, including its composition, size, shape, crystallinity, surface modification, and the surrounding environment.

Materials scientists have witnessed, in the last couple of decades, the success in synthesis of nanoparticles made of a broad range of materials. However, the reproducibility and homogeneity of the synthesized nanoparticles still needs to be significantly improved for practical applications with optimized performance<sup>7,8</sup>. For example, current shape-controlled metal nanoparticle synthesis always results in relatively poor control over the uniformity of the absolute shape and aspect ratio of the resulting nanoparticles, as compared, for instance, to the level of

size monodispersity achieved in spherical nanoparticle synthesis<sup>9,10</sup>. The drawbacks are ascribed to a poor understanding of the complex nucleation and growth steps involved in the synthesis of colloidal nanoparticles. The absence of sufficient knowledge regarding nanoparticle formation in liquid media is due to the difficulty in developing effective tools to see *through* solvents and probe chemical and physical events in the liquid. This situation also leads to challenging barriers that prevent the synthesis of functional nanoparticles with precisely tailored properties and a better understanding of the dependence of nanoparticles' performance on their physical parameters.

Research in developing techniques for the real-time probing of colloidal nanoparticle growth in liquid media is becoming increasingly important for discerning the structural information about the intermediates of nanoparticles. Although conventional characterization techniques including scanning electron microscopy (SEM) and transmission electron microscopy (TEM) have been extensively

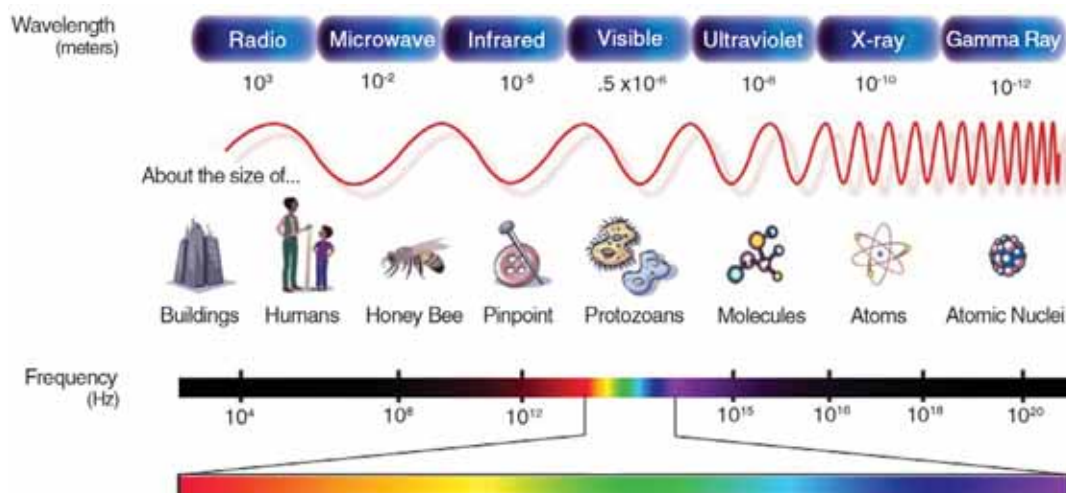


Fig. 1 Diagram of the electromagnetic spectrum, showing the type, wavelength (with comparable objects), and frequency of the radiation. Adapted and reproduced with permission from NASA.

used to study stable, dry nanocrystals, they are not compatible with the direct observation of nanocrystals dispersed in liquid because of the requirement of a high vacuum<sup>11</sup>. Significant progress has been made most recently in developing TEM liquid cells for *in situ* studies<sup>12-17</sup>. However, crystalline structures and internal defects of the nanoparticles, which are critical for shape selection and the improvement of nanoparticles' performance, are difficult to analyze using *in situ* TEM due to the weak penetration of electrons into liquids and the strong background interference. Furthermore, the electrons are negatively charged and may induce unwanted reducing reactions with precursors<sup>18</sup>. In contrast, electromagnetic waves are free of charge and may represent an ideal class of probes for *in situ* studies of solution-phase reactions, which may eliminate side reactions. Depending on the energy of the electromagnetic radiation, the electromagnetic spectrum consists of radio waves, microwaves, infrared (IR) radiation, visible light, ultraviolet (UV) radiation, x-rays, and gamma rays. As shown in Fig. 1, the wavelengths of different electromagnetic radiations vary in a very broad range from thousands of meters to sub-picometers. Within this spectrum, near-infrared (NIR)-visible-UV light has been employed to monitor the growth of plasmonic nanoparticles and quantum dots, because of the strong absorption/scattering and fluorescence in this spectral region<sup>19,20</sup>.

For example, a yellowish dispersion of Ag nanowires undergoes a significant color change when it galvanically reacts with an aqueous solution of  $\text{HAuCl}_4$ <sup>21</sup>. As shown in Figs. 2a-d, the major peaks of the absorption spectra of the nanostructures vary in the visible-NIR region depending on the volume of the  $\text{HAuCl}_4$  solution added to the dispersion of Ag nanowires. However, structural and morphological variation of the resulting nanoparticles cannot be predicted simply according to the absorption spectra because optical properties of metal nanoparticles can be influenced by many parameters such as composition<sup>22</sup>, morphology<sup>9,23-26</sup>, surface chemistry<sup>10</sup>, surrounding environment<sup>27</sup>,

aggregation<sup>28</sup>, etc. In general, *ex situ* characterization, such as electron microscopy, is necessary to assist the interpretation of the *in situ* spectral observations. Fig. 2e presents TEM images of the Ag nanowires before and after they react with different amounts of  $\text{HAuCl}_4$ , clearly showing that the solid Ag nanowires (top panel) are converted to hollow nanotubes with smooth walls (middle panel) and porous walls (bottom panel). The hollowing process accounts for the redshift of absorption peaks. On the other hand, optical imaging microscopy cannot provide similar spatial resolution to TEM for analyzing nanoparticles on the nanometer scale because of the Abbe diffraction limit that is described by

$$d = \frac{\lambda}{2 \times \text{NA}}, \quad (1)$$

where  $\lambda$  and NA are wavelength of the light and numerical aperture of the optics, respectively. The imaging spatial resolution can be improved by either increasing NA or decreasing  $\lambda$ . The theoretical maximum NA of an optic lens operating with air as the imaging medium ("dry" microscope objectives) is 1. As a result, decreasing the light wavelength represents the most effective means to enable a microscope for imaging objects with atomic resolution. As shown in Fig. 1, x-rays have wavelengths comparable with the size of atoms and thus the corresponding x-ray techniques are suitable for imaging nanoscale objects with improved resolution. In addition, many techniques based on the use of x-rays including scattering methods (e.g., small-angle x-ray scattering or SAXS<sup>29-34</sup>, wide-angle x-ray scattering or WAXS<sup>35-40</sup>, energy dispersive x-ray diffraction or EDXRD<sup>41-45</sup>, etc.) and spectroscopy (e.g., x-ray absorption fine structure spectroscopy or XAFS<sup>46-50</sup>, x-ray absorption near edge structure or XANES<sup>51,52</sup>, x-ray fluorescence spectroscopy<sup>53</sup>, x-ray Raman spectroscopy<sup>54</sup>, etc.) are also being explored for studying nanomaterials in liquid environments. Here, we will focus on the *in situ* transmission x-ray microscopy (TXM) and time-resolved high-energy x-ray scattering recently developed at the Advanced Photon Source (APS) at Argonne National Laboratory. Real

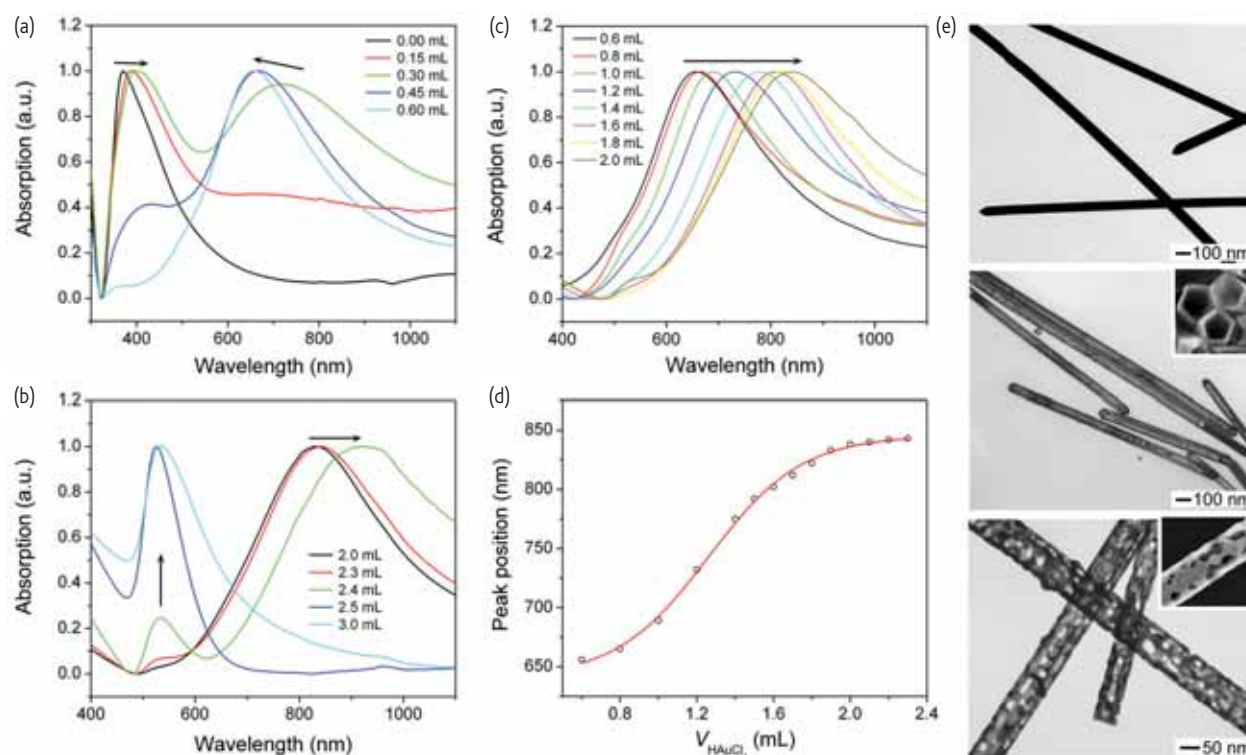


Fig. 2 (a–c) UV-visible-NIR absorption spectra of dispersions of Ag nanowires (equal amount) before and after they reacted with different volumes of  $\text{HAuCl}_4$  (1 mM) aqueous solution. All spectra were normalized against the intensities of the strongest peaks. (d) Absorption peak position of the products as a function of the volume of  $\text{HAuCl}_4$  solution. (e) TEM images of the Ag nanowires before (top) and after they reacted with 0.60 mL (middle) and 2.3 mL (bottom) of  $\text{HAuCl}_4$  solution. Adapted with permission from<sup>21</sup>, © 2004 American Chemical Society.

examples will be discussed to show their promise in real-time probing of variations of morphology, crystallinity, and dimension of nanoparticles involved in solution-phase reactions.

### Transmission x-ray microscopy (TXM)

A spatial resolution of sub-100 nm can be achieved for a hard x-ray microscope by using a Fresnel lens or a short-focus compound refractive lens<sup>55–57</sup>. With current fabrication technology, the achievable NA for a Fresnel lens is in the range of several mrad with a multi-keV hard x-ray radiation, leading to a spatial resolution of 10 – 15 nm but extended depth of focus of tens of micrometers<sup>58</sup>. Depending on the configuration, an x-ray microscope can be operated in either full-field transmission mode or scanning mode. Although a scanning x-ray microscope usually offers higher spatial resolution and better imaging contrast<sup>59</sup>, the corresponding imaging process is slow and is not suitable for probing the kinetics involved in solution-phase reactions. Here we will concentrate on TXM that can image the fast transition stages of nanoparticles in real time by using high-speed detectors but not significantly scarify the spatial resolution determined by the Fresnel lenses. A typical TXM microscope works similarly to a conventional optical microscope. Fig. 3a gives the schematic configuration of a TXM microscope that consists of a condenser lens, a beam stop, a pinhole (optional), an objective lens (i.e., Fresnel zone plate), and a CCD detector. Fig. 3b presents a photo of an

assembly of apparatus of a TXM microscope in combination with a flow cell for *in situ* studying solution-phase reactions in the flow cell.

### Advantages of TXM

The spatial resolution (10 – 15 nm) of the TXM is between that of optical microscopy (hundreds of nanometers) and electron microscopy (0.1 nm). As a result, TXM represents an ideal technique for imaging objects with lateral dimensions ranging from 50 nm to 2  $\mu\text{m}$  that are difficult to be properly characterized by other imaging techniques. In addition, the TXM method is more suitable for studies with solution-phase reactions due to its advantages:

- (1) The entire TXM microscope can be operated in ambient environment conditions (Fig. 3b) due to the strong penetration of hard x-ray in air and solvents, leading to the compatibility with solution-phase reactions.
- (2) The open system design and the large working distance (for example, over 5 cm in the system shown in Fig. 3b) enables the easy integration of reaction vessels and easy access to the reaction vessels to manipulate complicated reaction conditions.
- (3) TXM is capable of controlling image contrast of different elements by tuning the x-ray energy. For instance, individual elemental compositions can be mapped by using their characteristic absorption

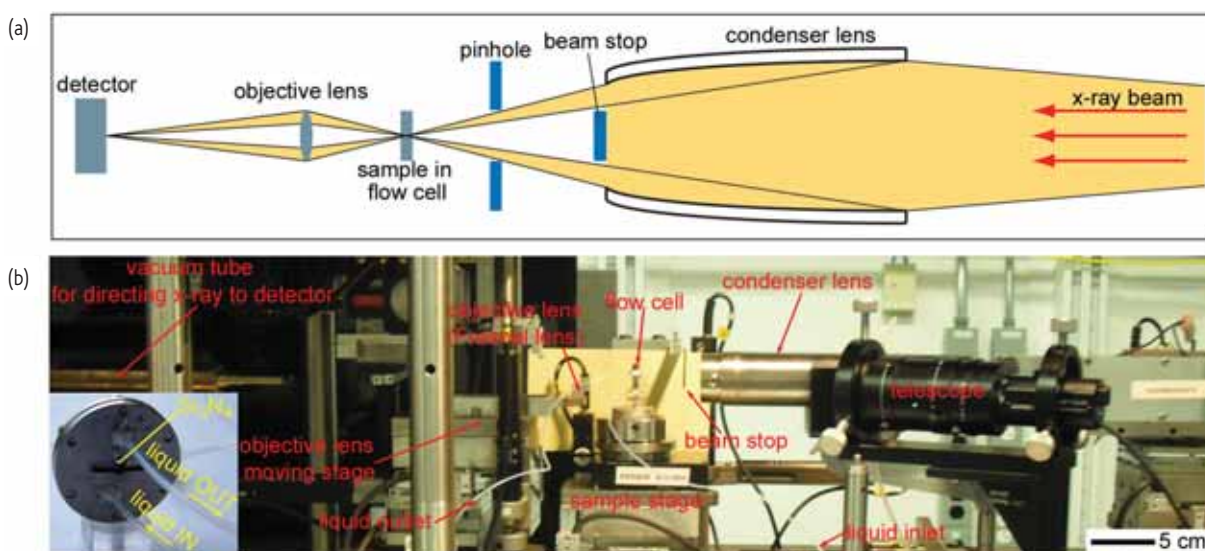


Fig. 3 Schematic illustration of the typical configuration (top) and a photograph (bottom) of a transmission x-ray microscope. Adapted with permission from<sup>62</sup>, © 2011 American Chemical Society.

edges, and furthermore XANES spectra can be used to map the chemical states of individual elements<sup>60,61</sup>.

- (4) TXM is also capable of taking tomographic images of objects with complex geometries<sup>55</sup>.
- (5) The spatial resolution of TXM can, in theory, be pushed down below the nanometer scale, if fabrication techniques are advanced enough to create Fresnel lenses with larger NAs<sup>55</sup>.

### ***In situ* flow-cell TXM**

Chemical reactions, in general, are quickly triggered once the precursors are mixed in solutions. For example, the Ag nanowires shown in Fig. 2e immediately react with HAuCl<sub>4</sub> through a galvanic replacement reaction when an aqueous solution of HAuCl<sub>4</sub> is added to the dispersion of the nanowires<sup>21</sup>. However, a period of time is usually required for setting up instrument, sample alignment, etc. after the reaction vessel is placed in the TXM system. As a result, reaction precursors cannot be mixed until the TXM system is ready for imaging. Flow-cell reactors represent a promising class of reaction vessel because the precursors can be remotely delivered into the reactors at desirable times to trigger the corresponding chemical reactions. As shown in the inset of Fig. 3b, a flow cell chamber is formed in a sandwich structure by sealing two parallel Si<sub>3</sub>N<sub>4</sub> membranes that are supported with two stainless steel disks with a rubber O-ring. Because of the excellent mechanical strength (e.g., high strength, high fracture toughness, high hardness) of Si<sub>3</sub>N<sub>4</sub>, the Si<sub>3</sub>N<sub>4</sub> membranes can be very thin (50 – 100 nm), leading to a minor attenuation of the x-rays. The good chemical resistance of Si<sub>3</sub>N<sub>4</sub> means that the membranes are compatible with a large variety of solution-phase reactions. Two Teflon tubes are connected to the cell for delivering a precursor solution into the cell and discharging the waste solution out of the cell, respectively. If multiple precursor solutions are necessary, more tubes can be connected to the cell for delivering the solutions into the cell to initiate chemical

reactions. As a result, the integration of a flow cell and a TXM microscope is ideal for monitoring variations of nanoparticles involved in the solution-phase reactions in real time. In a typical experiment, precursor solutions can be pumped into the flow cell to either trigger the growth of nanoparticles or react with nanoparticles pre-loaded in the flow cell. For example, morphological variation of the Ag nanowires (Fig. 2e) attached to the Si<sub>3</sub>N<sub>4</sub> membrane can be *in situ* monitored as an aqueous solution of 1 mM HAuCl<sub>4</sub> is continuously pumped into the flow cell<sup>62</sup>.

### **Morphological evolution of Ag nanowires**

The Ag nanowires are first deposited on the surface of one Si<sub>3</sub>N<sub>4</sub> membrane through a drop-casting process. The imaging process is initiated immediately before the HAuCl<sub>4</sub> solution is continuously injected into the flow cell by a syringe pump to trigger the galvanic replacement reaction. The nanowires in the imaging field are continuously monitored in real time. Fig. 4 presents a series of images of a partial Ag nanowire with a diameter of ~160 nm in the course of the replacement reaction, clearly showing the transformation of the solid nanowire into a nanotube. The reaction initiates the formation of pits at some spots (as highlighted by the blue arrows) that have surface energy higher than other surface areas of the nanowires. A continuous reaction etches out the Ag nanowire and deposits an Au layer on the surface of the nanowire. With the protection of the Au layer, the nanowire is etched along its longitudinal axis and eventually converted to a hollow nanotube at ~34 s. The Au layer can alloy with the Ag nanowire underneath to form an Au/Ag alloy during the galvanic reaction because of the similar lattice constants between Ag (4.0862 Å) and Au (4.0786 Å)<sup>21</sup>. Further reaction of the Au/Ag alloy nanotube with HAuCl<sub>4</sub> forces a dealloying process to dissolve the Ag atoms in the nanotube, leading to the formation of pores (as highlighted by the red arrows) in the wall of the nanotube. The schematic illustration (bottom panel, Fig. 4) summarizes the *in situ* TXM observations that clearly

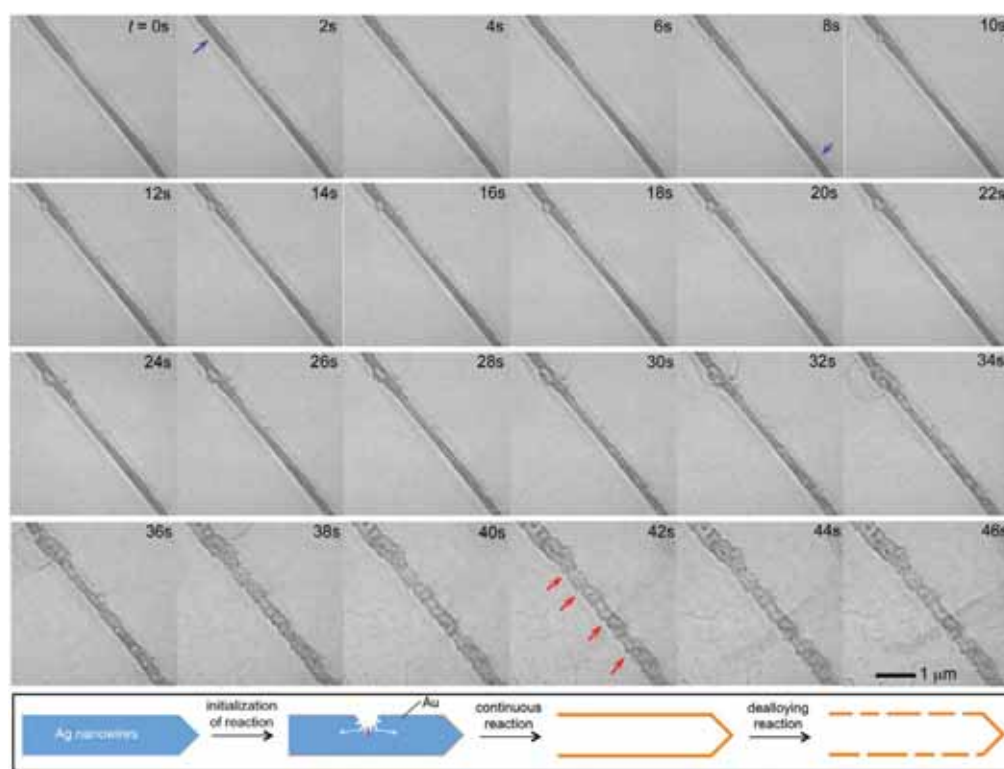


Fig. 4 A series of TXM images of a partial Ag nanowire with a diameter of  $\sim 160$  nm before and after they reacted with an aqueous solution of  $\text{HAuCl}_4$  for different times. The scale bar applies to all images. The schematic illustration in the bottom frame summarizes the major steps involved in the morphological evolution of the Ag nanowire during the galvanic replacement reaction. Adapted with permission from<sup>62</sup>, © 2011 American Chemical Society.

show the morphological evolution of single Ag nanowires in the course of the galvanic replacement reaction between the nanowires and aqueous solution of  $\text{HAuCl}_4$ . The morphological evolution of the Ag nanowires revealed by the *in situ* TXM studies is consistent with the *ex situ* electron microscopic studies shown in Fig. 2e. This example demonstrates the capability of *in situ* flow-cell TXM in probing morphological variations of nanoparticles involved in different reactions such as synthesis, catalysis, surface modification, assembly, etc.<sup>60–64</sup>

### Time-resolved x-ray scattering

Scattering signals with different reciprocal spaces (i.e.,  $Q$  values) can be recorded by placing two-dimensional (2D) detectors (e.g., GE<sup>®</sup> amorphous Si area detectors, Pilatus<sup>®</sup> detectors) at different positions related to samples. Depending on the  $Q$  values of diffraction patterns, x-ray scattering techniques include SAXS (with very low  $Q$ ), WAXS (also called x-ray diffraction or XRD, with intermediate range of  $Q$ ), and total scattering pair distribution function (PDF, with very high  $Q$ ). Fig. 5 summarizes the possible integration layout of different scattering techniques and their distinguished capabilities in characterizing structure, size, and morphology of nanoparticles. The high temporal resolution (down to several microseconds) of state-of-art x-ray detectors permits the use of time-resolved x-ray scattering techniques to help us understand the intermediate processes involved in nanoparticle growth and transformation.

### Time-resolved small-angle x-ray scattering (SAXS)

SAXS is a small-angle scattering technique in which one monitors the elastic scattering of x-rays by a sample with inhomogeneities in the nanometer range. It is recorded at very low angles, e.g., typically in the range of  $0.1 - 10^\circ$  depending on the energy of the x-rays. In principle, SAXS can be used for determining microscale or nanoscale particles in terms of such parameters as averaged sizes, shapes, distribution, and surface-to-volume ratio regardless of the dispersion media, which host the particles. A small-angle scattering pattern can be fitted with intensities calculated from different model shapes when the size distribution is known. If the shape is known, a size distribution may be fitted to the intensity. The latter case is the assumption used in the *in situ* study of nanoparticle growth as reported in the few available papers<sup>29–34</sup>. For example, the shape of nanocrystals is assumed to be spherical in the study of nucleation and growth of colloidal Au nanoparticles, and the spherical shape remains the same throughout the reactions<sup>34</sup>. In the case of Au nanorods, their shape is assumed to be cylindrical with a circular cross section, which remains unchanged during the entire growth<sup>33</sup>. These studies lead to an insightful understanding on the growth process of metal nanocrystals. For instance, the growth parameters along the longitudinal and traverse axes of Au nanorods are independently in a “seed-mediated” approach and a crossover exists from 1D (anisotropic) to 3D (isotropic) growth mode. The appearance of the crossover point without the need of a switch for the growth mode allows us to finely tune the shape of the nanorods.

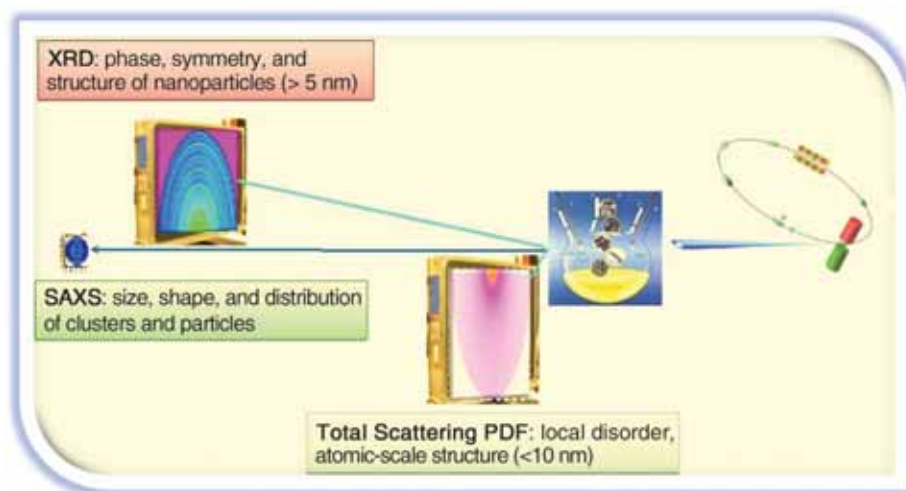


Fig. 5 Possible assembly of a number of time-resolved x-ray scattering techniques for *in situ* monitoring nanoparticle variations in solution-phase reactions.

In real reaction systems dimensions and shapes of the nanocrystals with small sizes do change, however, not independently. As a result, it is necessary to combine SAXS with additional information derived from other measurements, such as total scattering PDF and high-resolution XRD, to help us determine the precise sizes and shapes of nanocrystals.

#### Time-resolved total scattering pair distribution function (PDF)

The total x-ray scattering and diffraction features from small objects with sizes less than 5 nm in liquid media includes broadened Bragg peaks, diffuse components of the diffraction pattern, and solution effects, which correspond to local structural imperfections, interactions between nanocrystals, and solvent molecules, respectively. As a result, it is difficult to precisely determine the 3D structures of small nanocrystals by using traditional x-ray diffraction with the 'Rietveld Method'<sup>65</sup>. Recent advancement in x-ray diffraction proves that high-energy (e.g., > 60 keV) x-ray total scattering in combination with the atomic PDF data analysis can be used to determine the 3D structures of materials with reduced structural coherence, such as clusters of atoms and nanocrystals<sup>66,67</sup>. The key of this technique is that high-energy x-ray total scattering enables the collection of scattering signals in the high reciprocal space.

#### Time-resolved high-resolution x-ray diffraction (XRD)

When nanocrystals have sizes above ~5 nm, the x-ray diffraction patterns contain well-defined Bragg peaks, which can be analyzed by using the conventional powder diffraction technique. High angular-resolution XRD experiments are important for revealing the long-range structural coherence, internal strain, distortion-induced phase variation, possible symmetry change, and nano-twin formation. The availability of high-flux hard x-rays from the APS, a third generation synchrotron source, has significantly advanced the real-time investigation of solid-state materials in working conditions, although probing nanocrystals in solution is still challenging because of the large liquid volume versus the small fraction of nanocrystallite volume. As a result, the successful development of a time-resolved high-resolution XRD

technique compatible with solution-phase reactions can significantly benefit mechanistic understanding of nanophase evolutions.

We have successfully explored the focused high-energy x-ray beam at beamline 1-ID of APS as probe for *in situ* monitoring of the nanophase evolution at liquid/solid interfaces formed between an aqueous solution of  $\text{AgNO}_3$  and *n*-type GaAs wafers (Fig. 6a)<sup>68</sup>. The success is ascribed to the high photon intensity of a focus beam and low absorption of high-energy x-rays in liquid solvents (i.e., water for this case). Formation of the liquid/solid interfaces can induce immediate galvanic reactions between  $\text{AgNO}_3$  and GaAs, leading to the formation of nanoparticles at room temperature<sup>69</sup>. Figs. 6b, c compares the XRD patterns recorded at different reaction times, clearly showing the development of new crystalline phases along with the reaction. When the reaction time is short (< 30 s), only metallic Ag nanoparticles (i.e., nanoplates) are deposited on the GaAs surface through the reaction between  $\text{AgNO}_3$  and GaAs. The formation of pure Ag is confirmed by the appearance of Bragg diffraction peaks consistent with face-centered cubic (f.c.c.) Ag. New diffraction peaks corresponding to f.c.c.  $\text{Ag}_7\text{NO}_{11}$  (silver oxy salt) and simple cubic (s.c.)  $\text{Ag}_3\text{AsO}_4$  nanocrystals start to appear when the reaction time is longer than 30 s. Formation of these compounds is ascribed to the oxidation reactions initiated by the x-ray induced holes in the GaAs: (i) oxidation of  $\text{AgNO}_3$  to form  $\text{Ag}_7\text{NO}_{11}$  nanoparticles, and (ii) oxidation of GaAs to release  $\text{AsO}_4^{3-}$  ions into the  $\text{AgNO}_3$  solution, leading to a precipitation reaction between  $\text{AsO}_4^{3-}$  and  $\text{Ag}^+$  ions to form  $\text{Ag}_3\text{AsO}_4$  nanoparticles. Time-dependent variations of XRD peak areas follow sigmoidal functions for Ag and  $\text{Ag}_7\text{NO}_{11}$  and a second order polynomial regression model for  $\text{Ag}_3\text{AsO}_4$ , respectively, indicating that the growth of Ag and  $\text{Ag}_7\text{NO}_{11}$  nanoparticles occurs on solid surfaces and the growth of  $\text{Ag}_3\text{AsO}_4$  occurs in the solution phase. Fig. 6d presents a typical SEM image of the product formed at 200 s. The image clearly shows the formation of three different types of particles: nanoplates made of Ag, small nanodots of  $\text{Ag}_7\text{NO}_{11}$  on the surfaces of the Ag nanoplates, and aggregates of  $\text{Ag}_3\text{AsO}_4$  nanoparticles (highlighted by

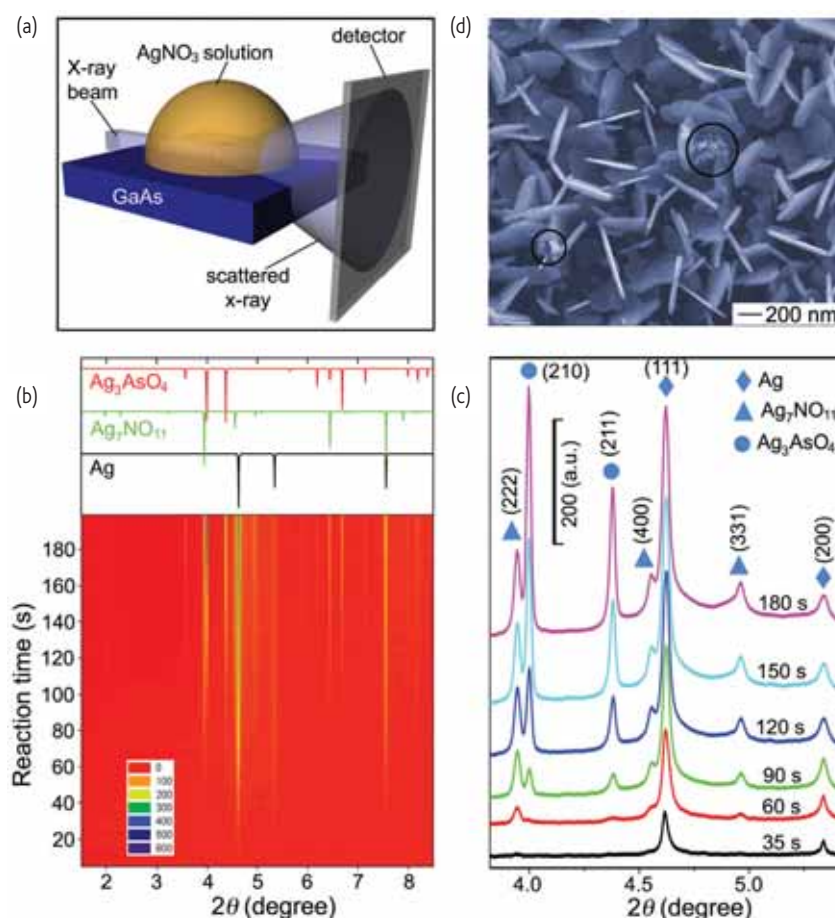


Fig. 6 (a) Schematic illustration of the experimental configuration for *in situ* monitoring of the evolution of nanoparticle growth at the liquid/solid interface formed between an *n*-type GaAs wafer and an aqueous solution of  $\text{AgNO}_3$ . (b,c) XRD patterns of the nanoparticles formed at the interface, recorded at different times. Standard powder XRD patterns of f.c.c. Ag, f.c.c.  $\text{Ag}_7\text{NO}_{11}$ , and s.c.  $\text{Ag}_3\text{AsO}_4$  are plotted as references. (d) SEM image of nanoparticles formed at 200 s. Adapted with permission from<sup>68</sup>, © 2010 American Chemical Society.

the black circles). It is believed that this time-resolved high-energy XRD technique is practically feasible for probing nanoparticle growth in homogenous liquid environments.

In addition to the angular-dispersive XRD (ADXRD) shown in Fig. 6, time-resolved energy-dispersive XRD (EDXRD) has also been used for real-time probing variations of crystalline phases involved in the formation of technologically and industrially relevant materials, such as zeolites, thiometallates, perovskite oxides (e.g.,  $\text{NaNbO}_3$ ). Detailed information regarding EDXRD can be found in a number of reviews<sup>42,70</sup>. The instruments of EDXRD are simpler and cheaper than ADXRD, but the resolution of EDXRD is lower.

### Future challenges and outlook

As discussed above, each x-ray method has specific advantages and disadvantages in probing nanoparticles of different length scales and other parameters. It is difficult (or even impossible) to formulate a complete picture of a nanophase evolution mechanism involved in a solution-phase reaction according to the *in situ* measurements based on a single method. As a result, the integration of different methods

represents one promising direction to collect more kinetic information of chemical reactions that are expected to help us better understand the complex chemical and physical events associated with nanophase evolution. The ideal solution is to couple as many as possible *in situ* x-ray techniques that can probe different aspects of nanoparticles, e.g., morphology, dimension, structure, composition, etc. to one beamline. However, the compatibility between different techniques should be thoroughly considered to maximize the information we can simultaneously record from the same reactions. For instance, the TXM requires an x-ray beam to be focused into a cone shape while the high-resolution XRD technique requires a collimated beam. It is difficult to integrate both the TXM and XRD technique together without a sophisticated design and methods for data analysis. In addition, the cost of experimental setups may dramatically increase with the inclusion of additional probing techniques. The level of expenditure compared to the value of the results should be carefully considered and balanced at the planning stage. Fig. 5 may represent an excellent example of how different x-ray scattering techniques including SAXS, high-resolution XRD, and total scattering PDF can be integrated with a high-energy

x-ray beamline for the real-time probing of nanoparticles in different reciprocal spaces. In this case, high-resolution XRD patterns can provide information about the structural evolution (e.g., nano-twin patterns, distortion, and lattice strains) and precise crystallographic phases of large nanoparticles (with sizes > 5 nm). The high-energy total scattering PDF is particularly suitable for determining the atomic-scale structures of small nanocrystals (< 10 nm) in solution phase. SAXS is capable of tracking variations of the sizes and shapes of nanoparticles. As a result, *in situ* observations from these three scattering techniques may provide information for comprehensively understanding the nanophase evolution of nanoparticles in liquid environments.

The synchrotron x-ray beams are usually focused to small areas for enhancing sensitivity of the *in situ* techniques. The high photon intensity may influence chemical reactions in unexpected ways, that can induce redox reactions with reaction precursors, even though the x-rays are free of charge. For example, photo-sensitive components involved in chemical reactions can absorb x-rays to drive charge separation

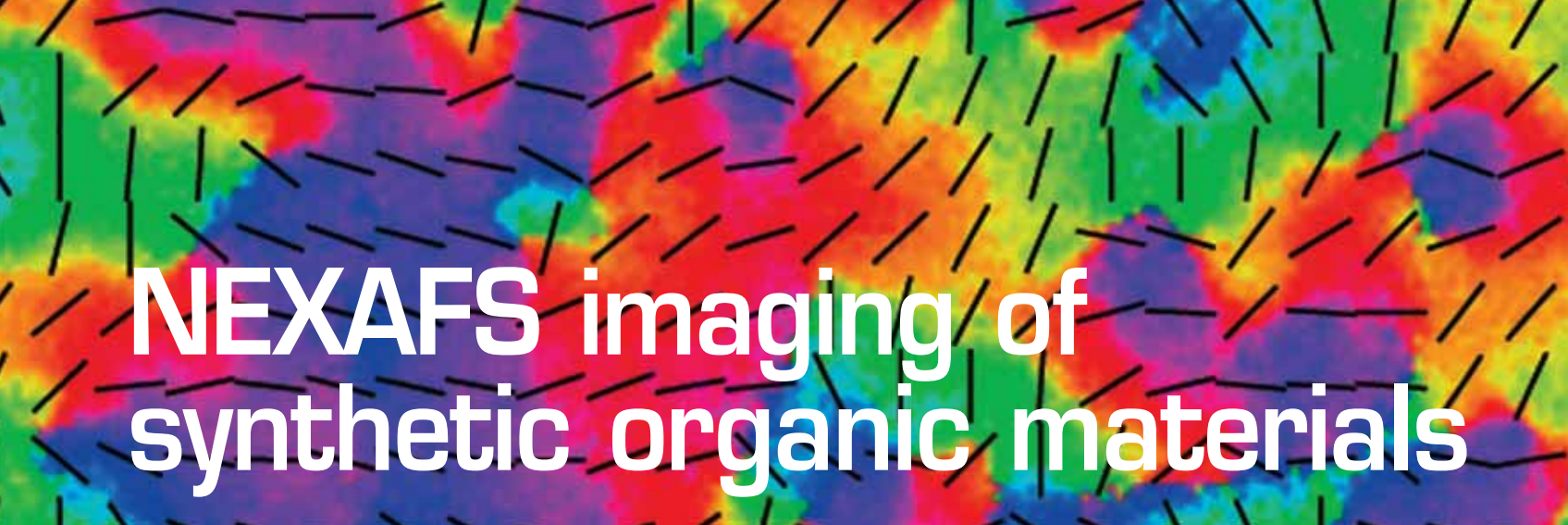
processes and the resulting charges can induce unexpected reactions. The formation of Ag<sub>7</sub>NO<sub>11</sub> and Ag<sub>3</sub>AsO<sub>4</sub> nanoparticles shown in Fig. 6 represents such an example. In general, high-intensity x-rays can break chemical bonds of solvent molecules and precursors in solution-phase reactions, resulting in the formation of very reactive radicals<sup>71</sup>. This process is called photodissociation, photolysis, or photodecomposition. Apparently, x-rays with higher intensity can induce the formation of more radicals that influence chemical reactions more significantly. As a result, achieving better probing sensitivity and avoiding unwanted side reactions should be carefully balanced for *in situ* studying nanophase evolutions in different reactions. 

## Acknowledgements

Use of the Center for Nanoscale Materials, Advanced Photon Source, and Electron Microscopy Center for Materials Research at Argonne National Laboratory was supported by the U.S. Department of Energy, Office of Science, Office of Basic Energy Sciences, under contract No. DE-AC02-06CH11357.

## REFERENCES

1. Arico, A. S., *et al.*, *Nature Mater* (2005) **4**, 366.
2. Atwater, H. A., and Polman, A., *Nature Mater* (2010) **9**, 205.
3. Grätzel, M., *Nature* (2001) **414**, 338.
4. Gur, I., *et al.*, *Science* (2005) **310**, 462.
5. Ji, L., *et al.*, *Energy Environ Sci* (2011) **4**, 2682.
6. Tian, N., *et al.*, *Science* (2007) **317**, 732.
7. Tao, A., *et al.*, *Nature Nanotechnol* (2007) **2**, 435.
8. Lee, I., *et al.*, *Proc Natl Acad Sci USA* (2008) **105**, 15241.
9. Xia, Y., *et al.*, *Angew Chem Int Ed* (2009) **48**, 60.
10. Peng, S., *et al.*, *Proc Natl Acad Sci USA* (2010) **107**, 14530.
11. de Jonge, N., and Ross, F. M., *Nature Nanotechnol* (2011) **6**, 695.
12. Williamson, M. J., *et al.*, *Nature Mater* (2003) **2**, 532.
13. Zheng, H., *et al.*, *Science* (2009) **324**, 1309.
14. Grogan, J. M., and Bau, H. H., *J Microelectromechanical systems* (2010) **19**, 885.
15. Evans, J. E., *et al.*, *Nano Lett* (2011) **11**, 2809.
16. Zheng, H., *et al.*, *Nano Lett* (2009) **9**, 2460.
17. Zheng, H., *et al.*, *Science* (2011) **333**, 206.
18. Goessens, C., *et al.*, *Ultramicroscopy* (1992) **40**, 151.
19. Dagrepe, P., *et al.*, *J Phys Chem C* (2007) **111**, 14977.
20. Zhang, Q., *et al.*, *Nano Lett* (2010) **10**, 5037.
21. Sun, Y., and Xia, Y., *J Am Chem Soc* (2004) **126**, 3892.
22. Liu, S., *et al.*, *Chem Mater* (2011) **23**, 4098.
23. Kelly, K. L., *et al.*, *J Phys Chem B* (2003) **107**, 668.
24. Murphy, C. J., and Jana, N. R., *Adv Mater* (2002) **14**, 80.
25. Tao, A., *et al.*, *Small* (2008) **4**, 310.
26. Jin, R., *et al.*, *Nature* (2003) **425**, 487.
27. Haes, A. J., *et al.*, *J Phys Chem B* (2004) **108**, 6961.
28. Kim, Y., *et al.*, *Nano Lett* (2001) **1**, 165.
29. Takesue, M., *et al.*, *J Am Chem Soc* (2011) **133**, 14164.
30. Harada, M., *et al.*, *J Phys Chem C* (2011) **115**, 14081.
31. Manocchi, A. K., *et al.*, *Langmuir* (2011) **27**, 7052.
32. Polte, J., *et al.*, *ACS Nano* (2010) **4**, 1076.
33. Henkel, A., *et al.*, *J Phys Chem C* (2009) **113**, 10390.
34. Abécassis, B., *et al.*, *Nano Lett* (2007) **7**, 1723.
35. Chen, J., *et al.*, *J Phys Chem Lett* (2011) **2**, 1874.
36. Pein, A., *et al.*, *Inorg Chem* (2011) **50**, 193.
37. Cheong, S., *et al.*, *J Am Chem Soc* (2009) **131**, 14590.
38. Bremholm, M., *et al.*, *Angew Chem Int Ed* (2009) **48**, 4788.
39. Middelkoop, V., *et al.*, *Chem Mater* (2009) **21**, 2430.
40. Jørgensen, J.-E., *et al.*, *J Solid State Chem* (2008) **181**, 1925.
41. Terry, A. E., *et al.*, *Synchrotron Radiation News* (2002) **15**, 4.
42. Kämpfe, B., *et al.*, *Part Part Syst Charact* (2005) **22**, 391.
43. Rehan, M., *et al.*, *Cryst Eng Comm* (2011) **13**, 3725.
44. Walton, R. I., *et al.*, *Chem Mater* (1999) **11**, 3201.
45. Evans, J. S. O., *et al.*, *Rev Sci Instrum* (1995) **66**, 2442.
46. Oyanagi, H., *et al.*, *J Synchrotron Rad* (2011) **18**, 272.
47. Newton, M. A., and van Beek, W., *Chem Soc Rev* (2010) **39**, 4845.
48. Uehara, M., *et al.*, *Appl Phys Lett* (2009) **94**, 063104.
49. Harada, M., and Inada, Y., *Langmuir* (2009) **25**, 6049.
50. Harada, M., *et al.*, *J Colloid Interf. Sci.* (2009) **337**, 427.
51. Chen, C.-H., *et al.*, *ACS Nano* (2007) **1**, 114.
52. Abécassis, B., *et al.*, *Langmuir* (2010) **26**, 13847.
53. West, M., *et al.*, *J Anal At Spectrom* (2011) **26**, 1919.
54. Liu, H., *et al.*, *Nano Lett* (2007) **7**, 1919.
55. Sakdinawat, A., and Attwood, D., *Nature Photon* (2010) **4**, 840.
56. Wang, Y., *et al.*, *Nature* (2003) **424**, 50.
57. Bosak, A., *et al.*, *Adv Mater* (2010) **22**, 3256.
58. Chao, W., *et al.*, *Opt Exp* (2009) **17**, 17669.
59. Burke, K. B., *et al.*, *Nanotechnology* (2011) **22**, 265710.
60. de Groot, F. M. F., *et al.*, *Chem Phys Chem* (2010) **11**, 951.
61. Zhou, J., *et al.*, *J Mater Chem* (2011) **21**, 5944.
62. Sun, Y., and Wang, Y., *Nano Lett* (2011) **11**, 4386.
63. Kuo, C.-H., *et al.*, *Adv Funct Mater* (2011) **21**, 792.
64. van Schooneveld, M. M., *et al.*, *Small* (2011) **7**, 804.
65. Rietveld, H. M., *J Appl Cryst* (1969) **2**, 65.
66. Petkov, V., *Mater Today* (2008) **11**(11), 28.
67. Petkov, V., *et al.*, *Phys Rev B* (2005) **72**, 195402.
68. Sun, Y., *et al.*, *Nano Lett* (2010) **10**, 3747.
69. Sun, Y., *Chem Mater* (2007) **19**, 5845.
70. Pienack, N., and Bensch, W., *Angew Chem Int Ed* (2011) **50**, 2014.
71. Mesu, J. G., *et al.*, *J Phys Chem B* (2005) **109**, 4042.



# NEXAFS imaging of synthetic organic materials

The utilization of near edge x-ray absorption fine structure spectroscopy (NEXAFS) in achieving strong, novel contrast for soft x-ray microscopy and scattering methods has been afforded significant success in elucidating outstanding issues in organic materials systems due to the unique combination of high sensitivity to chemical functionality and thus composition, moderately high spatial resolution and moderate radiation damage. We illustrate the basic operating principles of NEXAFS spectroscopy, scanning transmission x-ray microscopy, and resonant soft x-ray scattering, and exemplify the impact by discussing a few recent applications. The focus of this perspective will be the characterization of synthetic organic materials, with a further emphasis on applications involving semi-conducting polymers. We also provide a brief perspective of future instrument and method developments.

Ben Watts<sup>a</sup> and Harald Ade<sup>b,\*</sup>

<sup>a</sup>Swiss Light Source, Paul Scherrer Institute, 5232 Villigen PSI, Switzerland

<sup>b</sup>Department of Physics, NCSU, Raleigh, NC 27596, USA

\*Email: harald\_ade@ncsu.edu

**Synthetic organic materials play an increasingly important role in many aspects of life and areas of the economy, ranging from the use of block copolymers in shoes to semiconducting molecules and polymers used in lightweight and flexible electronics.**

Generally, the utilization of high performance materials requires the combination of multiple components with complementary properties that are naturally or intentionally nano-structured for optimal properties and performance. In most cases, these multiple components have unique chemical composition and functionality. Bulk heterojunction organic solar cells, composed of electron-donating and electron-accepting semi-conducting polymers, are a great example: the complementary nature of the two components greatly enhances power conversion efficiency

over a single material cell<sup>1</sup>. Similarly, the diffusion, flammability, and/or mechanical properties of polymers can be greatly improved with the inclusion of various additives such as clays, silica or nanofibers to homopolymers or polymer blends<sup>2</sup>. The desired nanostructures can be engineered by either top-down methods such as lithography and various deposition techniques or through bottom-up approaches that rely on self-assembly or directed self-assembly. Blending polymers in the presence of compatibilizers and creating well defined nano-structures with block copolymers (polymer chains composed of two or more sections of differing repeat units having desirable characteristics such as persistence length, hydrophobicity, etc.) are classic examples of self-assembly. Spin-casting of two component organic solar cells with or without processing

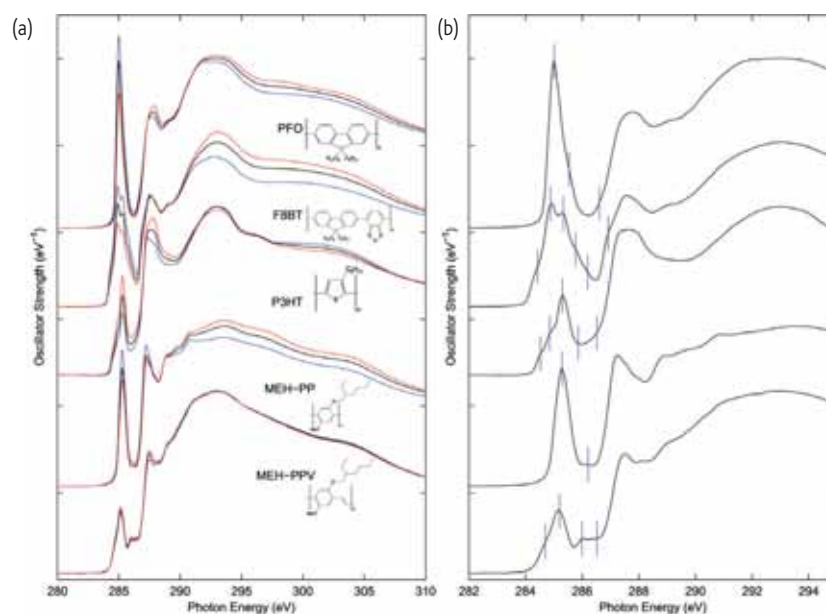


Fig. 1 (a) C 1s NEXAFS spectra of poly(9,9-dioctylfluorenyl-2,7-diyl) (PFO), poly[(9,9-dioctylfluorenyl-2,7-diyl)-co-(1,4-benzo-{2,1',3}-thiadiazole)] (F8BT), poly(3-hexylthiophene-2,5-diyl) (P3HT), poly[2-methoxy-5-(2-ethylhexyloxy)-1,4-phenylene] (MEH-PP) and poly[2-methoxy-5-(2-ethylhexyloxy)-1,4-phenylenevinylene] (MEH-PPV) at 20° (blue), 50° (black), and 90° (normal, red) x-ray incidence. (b) Expanded low energy regions of the same spectra with vertical lines marking fitted resonance positions. Adopted from<sup>26</sup>.

aids, or with subsequent thermal or vapor annealing is another example where the self-organization of nano-structures is utilized.<sup>1</sup>

To fully understand the structure-property or structure-performance relationships in engineered multicomponent systems, quantitative compositional analysis and morphological or structural characterization at the sub-100 nm or even the ~1 nm length scale is required. This need is generally addressed by various microscopy or scattering methods and the particular contrast mechanism exploited defines the utility of these methods<sup>3,4</sup>. Additional factors of importance that impact the suitability of a given method to answer the scientific questions at hand include the intrinsic spatial resolution achievable, the radiation dose delivered to the sample<sup>5-7</sup>, and the ease with which sample environments can be controlled<sup>8-10</sup>. During the last decade, near edge x-ray absorption fine structure (NEXAFS) microscopy has been shown to provide a combination of attributes that makes it ideally suited to investigate organic materials<sup>11-13</sup> and, more generally, materials with elements that have K- or L-edges in the 200 – 900 eV energy range<sup>8-10,14,15</sup>. We will delineate the general strengths of NEXAFS microscopy and exemplify it by highlighting a number of recent applications. An exclusive focus will be placed on the characterization of synthetic organic materials. Further emphasis will be placed on the scanning transmission x-ray microscopy (STXM)<sup>11,16,17</sup> implementation of NEXAFS microscopy, as it has the best combination of spectroscopy and imaging capabilities with low radiation dose and thus been used most frequently for the characterization of organic systems. The major competing methods in the field include full-field transmission x-ray microscopy (TXM)<sup>8,9,15</sup> and photoelectron emission microscopy (PEEM)<sup>12</sup>. While TXM holds a significant speed advantage over STXM, the prevailing TXM design makes recording of spectra problematic and the extra optical element introduces inefficiencies

that lead to higher radiation doses. Thus TXM has mostly been used for biological samples (de-emphasizing the spectroscopy requirements) and magnetic materials (de-emphasizing the radiation dose limitations)<sup>18-20</sup>. Similarly, PEEM is generally considered a poor choice for imaging organic materials because of low efficiencies leading to high radiation doses through a combination of low electron production by light elements and the need to select a narrow energy window (thereby discarding some of the available NEXAFS signal). Resonant soft x-ray scattering (R-SoXS)<sup>21,22</sup> from organic matter will also be discussed in the context of a reciprocal space complement to real space imaging, while still utilizing the principles of NEXAFS spectroscopy for contrast mechanisms in synthetic organic materials.

### Contrast mechanism with soft x-rays

The physical basis of NEXAFS and the soft x-ray contrast mechanism between polymers has been described previously and the reader is referred to the literature for the more subtle details<sup>12</sup>. We review here only some of the basic aspects in order to provide context for the applications discussed. The effects of the interaction of x-rays with matter is encoded in the complex index of refraction  $n(E) = 1 - \delta(E) + i\beta(E)$ , where  $E$  is the photon energy,  $\delta$  is the index decrement, and  $\beta$  is the extinction coefficient. An abrupt rise in  $\beta$  occurs at absorption edges, i.e., when the photon energy becomes large enough to excite deeper electronic levels. These absorption edges are intrinsically element specific. More importantly, strong and moiety specific variations in  $\beta$  are observed near an edge for most organic materials, resulting in a unique spectral fingerprint. We show in Fig. 1 some common semiconducting polymers to exemplify the sensitivity of NEXAFS to chemical functionality. NEXAFS

can also be sensitive to intermolecular interactions and the degree of order, yielding, for example, slightly different spectra for crystalline and amorphous phases of the same polymer<sup>23,24</sup>. The spectra presented in Fig. 1 also demonstrate systematic variations in intensity with changes in the angle of incidence of the linearly polarized x-rays. This effect is referred to as “linear dichroism” and the observed intensity of such a dichroic NEXAFS resonance depends on the squared cosine of the angle between the electric field vector of the incident x-ray beam and the transition dipole moment<sup>25</sup>. The NEXAFS final states (and the orientation of the transition dipole moment) are closely related to the anti-bonding orbitals, which provide information on molecular orientation and order<sup>25</sup>.

Since NEXAFS spectroscopy is a key underlying aspect exploited by many applications of x-ray microscopy, compilations of NEXAFS spectra from polymers have been provided by Dhez *et al.*<sup>27</sup>, Kikuma and Tonner<sup>28</sup>, and Watts *et al.*<sup>26</sup> and small molecules used in solar cells<sup>29</sup>. Additionally, inner shell electron energy loss spectroscopy (ISEELS) is the electron beam analogue to NEXAFS and so the small molecule ISEELS spectrum database provided by Hitchcock and Mancini is also useful<sup>30</sup>. The wide range of functional groups in these compilations are complemented by a series of NEXAFS spectra that illuminate the evolutionary trend of the spectral signature of a single functional group, the carbonyl group, as the nearest neighbor environment is changed progressively and systematically from a ketone to a carbonate group<sup>31</sup>. Even isomeric differences can be detected in favorable cases<sup>32</sup>. These functional-group-specific spectroscopic variations, along with the comparatively small radiation dose,<sup>5,6,33</sup> provide much of the advantages of NEXAFS microscopy as an analytical tool<sup>11,17</sup>. This is irrespective of whether the samples are investigated in transmission or in a surface sensitive mode<sup>34–36</sup>. Similarly, linear dichroism can be utilized as a contrast mechanism in NEXAFS microscopy in order to map molecular orientation within a material<sup>16,37</sup> and differentiate between amorphous and crystalline material<sup>38</sup>, as well as image domain patterns and the preferred molecular orientation within those domains<sup>39–41</sup>.

Microscopy methods are often complemented by scattering methods and the use of soft x-rays affords unique advantages for use of reciprocal space methods as well. Conventional small angle x-ray scattering (SAXS) generally relies on electron density differences<sup>4</sup> unless energies near an absorption edge are used to exploit “anomalous” enhancements<sup>42</sup>. In the soft x-ray energy range, these enhancements are referred to as resonant scattering, often referred to as R-SoXS. The primary appeal can be understood readily. The real and imaginary components of  $n$ , i.e.  $1-\delta$  and  $\beta$ , are related to each other by a Kramers-Kronig transform. Consequently,  $\delta$  also shows strong moiety specific energy dependence, as demonstrated in Fig. 2. Because the quantity  $\Delta\delta^2 + \Delta\beta^2$  determines the materials contrast and scattering strength  $I(q) \propto E^4(\Delta\delta^2 + \Delta\beta^2)$ , “bond-specific” contrast can be achieved in R-SoXS in a manner similar to NEXAFS microscopy<sup>21,22,43</sup>. In addition,  $\Delta\delta^2 + \Delta\beta^2$  overcomes the  $E^4$  factor and orders of magnitude larger scattering intensity can be achieved near the carbon edge relative to  $E \sim 10$  keV as used in conventional SAXS<sup>44</sup>. More recently, it has been demonstrated that R-SoXS furthermore has unique contrast to bond

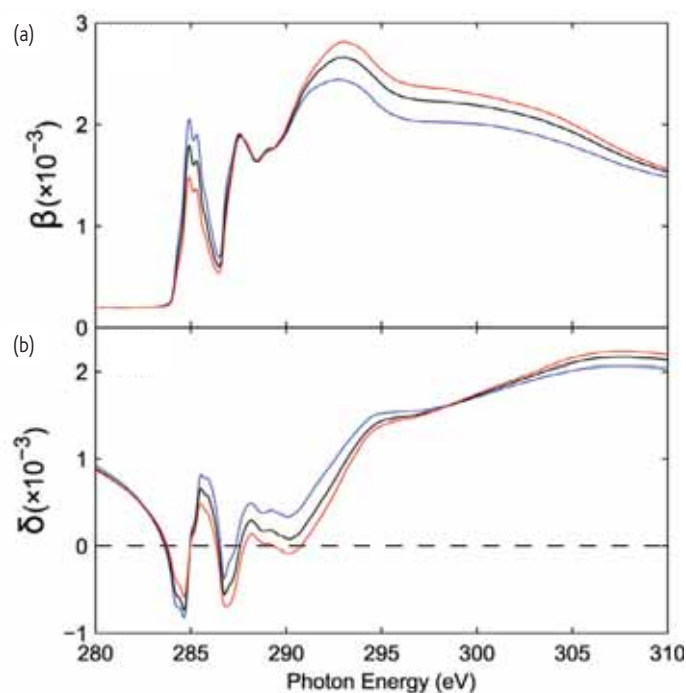


Fig. 2 (a) Absorption and (b) dispersive parts of the complex index of refraction of the polymer F8BT in the vicinity of the C K-edge at 20° (blue), 50° (black), and 90° (normal, red) x-ray incidence. Adopted from<sup>26</sup>.

orientation if polarization control of the incident photons is possible<sup>45</sup>. This is possible because the linear dichroism effect described above affects both  $\beta$  and  $\delta$  (see Fig. 2) and thus dichroic contrast mechanisms can be exploited by both microscopy and scattering methods.

## Principles and methods of scanning transmission x-ray microscopy

The basic operating principle of a STXM is illustrated in Fig. 3. A nanoscopic x-ray beam is produced with a zone plate (a transmission diffraction lens) and either the sample or the zone plate is raster scanned to acquire an image in serial fashion<sup>46–48</sup>. The zone plate produces a number of diffraction orders that would be detrimental to the imaging properties of a STXM, but can fortunately be eliminated almost completely with the use of a central stop and an order selecting aperture. The absorption of a sample as a function of location is detected with an x-ray to visible light converter based on a phosphor and final detection with a photomultiplier tube (PMT).

Several images at different energies can be acquired for (hyper) spectral imaging. In order to reduce acquisition time, data sets with reduced spatial information but increased spectral information (more energy points) are often acquired in the form of “line-scan” spectra and point spectra.<sup>47,48</sup> The requirement for high spatial resolution and spectroscopy has essentially confined the operation of a STXM to synchrotron facilities.

Images provide immediate information about shapes and length scales present in a sample, but the more interesting science is often found in discovering what those features are composed of. The soft x-ray probe

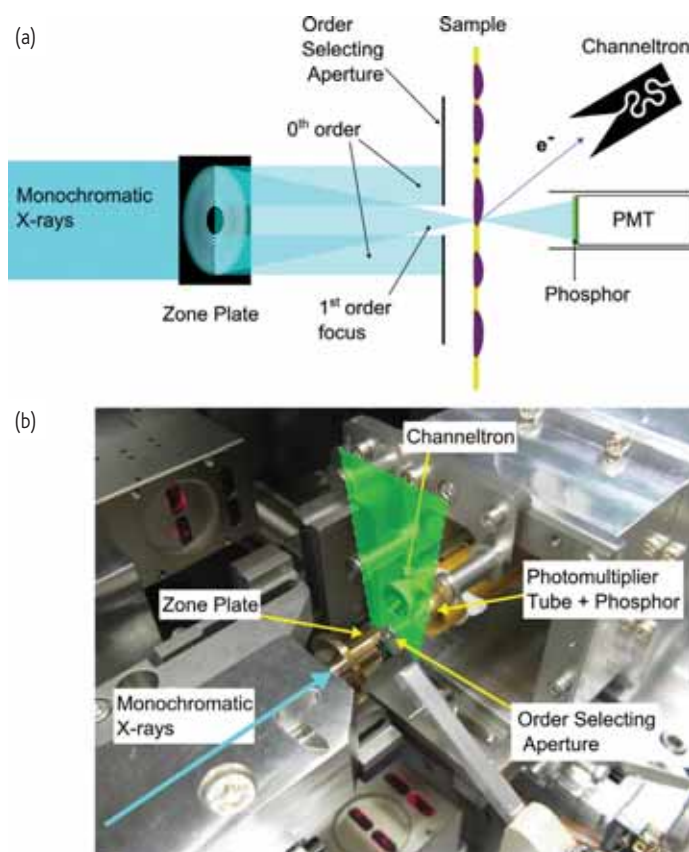


Fig. 3 (a) Schematic of basic set-up of a STXM that can also detect secondary electrons. For simplicity, only the 0<sup>th</sup> and positive 1<sup>st</sup> zone plate orders are shown. (b) Actual hardware of the PolLux STXM showing many of the key components as indicated. The sample mounting plate position is indicated in semi-transparent green and dashed outline. Elements of the position stabilizing interferometer (using a red HeNe laser) can be seen in the upper-left corner and lower-center.

utilized in STXM is highly advantageous in this respect, providing strong and tunable differentiation between materials (as discussed above) that is also relatively simple to interpret and to quantify. In a sample that consists of a mixture of materials, the spectra of the individual components

usually combine linearly to give the observed contrast. By measuring STXM images at a set of x-ray energies, one is effectively sampling the spectra at each pixel of the sample and so long as more images are recorded (i.e. energies sampled) than there are material components, then the percent composition (and total sample thickness) can be calculated at each pixel.

Two approaches are available for composition determination in STXM. One of these is to use principal component analysis (PCA), a mathematical procedure in which the unknown component spectra are estimated such that the fewest possible component spectra satisfactorily describe the observed variance in the set of measured STXM images<sup>49</sup>. This approach requires no prior knowledge of the component materials in the sample and is useful in areas such as biology and environmental science where a researcher has limited information about, and control over, the sample and possible reference compounds.

When one has access to the spectra of the pure material components, the simpler approach of composition determination by singular value decomposition (SVD; or least squares fitting) is applicable<sup>50-52</sup>. The component spectra can be measured in a STXM via pure samples or may also be available in the literature. The SVD approach is illustrated in Fig. 4, where STXM images of a blend of poly[(9,9-dioctylfluorenyl-2,7-diyl)-co-bis(N,N'-(4, butylphenyl))bis(N,N'-phenyl-1,4-phenylene)diamine] (PFB) and poly[(9,9-dioctylfluorenyl-2,7-diyl)-co-(1,4-benzo-{2,1',3}-thiadiazole)] (F8BT) recorded at x-ray energies of 284.5 eV (strong F8BT absorption) and 285 eV (strong PFB absorption) as well as 280 and 320 eV (chemically insensitive, for thickness determination) are utilized to calculate a composition map (Fig. 4 b) and corresponding thickness map (Fig. 4c). This approach is most popular for studies involving samples that are assembled from known components or where the major components are well known. The detailed knowledge gained from the study that yielded Fig. 4 will be discussed below in the context of specific scientific issues in organic solar cells.

Recent instrument developments include the use of a secondary electron detector, such as a channeltron, to allow simultaneous rear surface and transmission microscopy (see Fig. 3)<sup>36</sup>. We will present an example of this utility below in the context of a specific application.

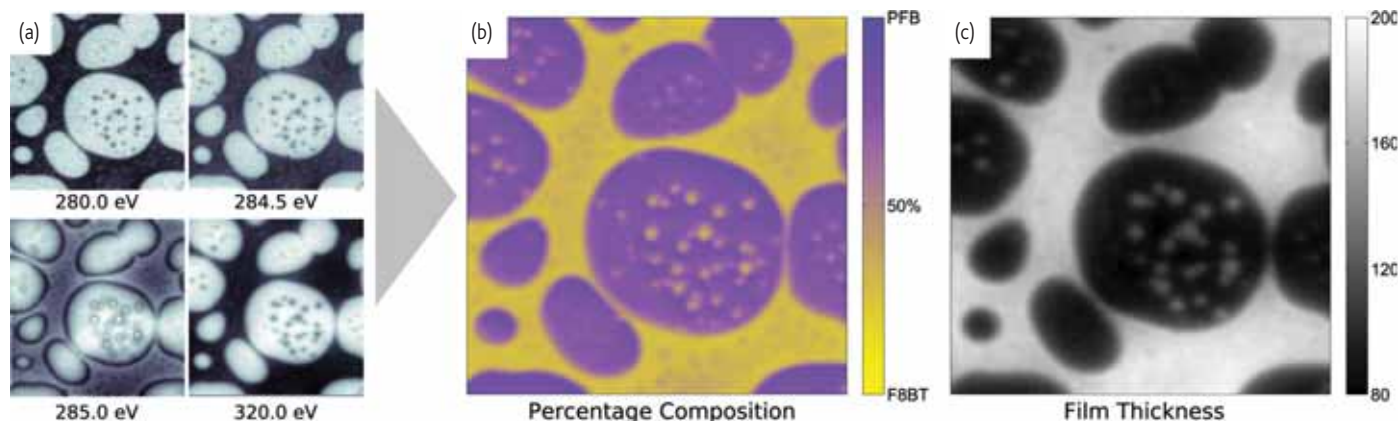


Fig. 4 (a)  $10 \times 10 \mu\text{m}$  STXM images of a polymer blend film (1:1 PFB:F8BT) recorded at individual x-ray energies. (b) Calculated composition and (c) thickness maps derived from the STXM images by singular value decomposition. Adopted from reference<sup>53</sup>.

### Insights from NEXAFS microscopy

The great appeal of organic electronic devices is the promise of low-cost production methods based on solution processing. However, solution processing produces complex structures through an intricate mix of thermodynamic and kinetic processes. This can be utilized to produce advantageous material nanostructures via strategic engineering of the material properties and tuning of the deposition and annealing parameters – but the complex and broad parameter space of the problem requires feedback information of high quality in order to make progress. In the case of bulk heterojunction polymer photovoltaics, an ideal active layer is often depicted as interdigitated domains of pure electron-donating and -accepting polymers with structures of ~10 nm width and that are each well connected to the corresponding device electrode, which reside at the top and bottom surface/interfaces of the ~100 nm thick film. Solution processing of a polymer blend film has been shown to produce polymer nanostructures tantalizingly similar to this ideal, with the ability for further tuning as discussed above. Besides producing an interconnected nanostructure, the process also needs to wet the electrodes properly. Ideally, only the hole-transporting material covers the anode and only the electron-transporting material covers the cathode.

Fig. 4 presents STXM images of a 1:1 PFB:F8BT blend film produced by spin-casting from a p-xylene solution and display a system of PFB-rich domains in a continuous F8BT-rich matrix with further F8BT-rich and PFB-rich subdomains enclosed respectively. This polymer blend system has been extensively studied as a model all-polymer active layer for photovoltaic devices via scanning probe<sup>54</sup>, x-ray<sup>55-57</sup>, and electron microscopies and x-ray scattering<sup>58,59</sup> as well as opto-electronic measurements and theoretical studies. While the STXM images in Fig. 4 provide a wealth of information on the domain sizes, shapes, and purities, these measurements integrate throughout the entire thickness of the film and thereby neglect an important aspect of the films structure in regards to its suitability in a device – the film interfaces. The polymer film is sandwiched between two electrodes and thus the top

and bottom interfaces across which electric charges must travel in order for the device to function properly are crucial components of a device. At the same time, the different surface energies of the two polymers and different solubility in the processing solvent means that these interface layers can have very different compositions and structures to that seen in the bulk of the film in Fig. 4, possibly creating large barriers to energy flow that reduce the device performance.

A number of techniques have been able to deduce various aspects of the surface layer characteristics. For instance, the outline of a partial capping layer and its charge trapping properties has been observed by scanning probe microscopy and presumed to be composed of PFB<sup>60</sup>. On the other side, a wetting layer of PFB is expected to cover the entire film/substrate interface from thermodynamic considerations and x-ray photoelectron spectroscopy measurements (averaging over relatively large areas) of a similar polymer blend system<sup>61</sup>. However, this collection of techniques require a great deal of work (and still give incomplete information) that cannot be economically and routinely repeated for the range of material combinations and processing parameters that pave the road towards performance optimized and commercially viable devices.

Now, just as in the bulk measurements, STXM also offers a solution for the imaging of surface layers. Total electron yield (TEY) mode NEXAFS measurements have long been used to produce x-ray absorption spectra of surfaces by utilizing the fact that the number of electrons emitted by an x-ray illuminated surface is proportional to the rate of x-ray absorption in the material surface, while the very short escape depth (material dependent; ~5 nm) of the ejected electrons limits the depth of the acquired information. This same method can be employed in a STXM (and also PEEM, though not in TXM), by mounting a channeltron electron detector beside the PMT detector, as shown in Fig. 3, and simultaneously measuring both the ejected electrons (channeltron) and transmitted x-rays (PMT) at each scanned pixel. Fig. 4 presents surface and bulk images of two sections of the same 1:1 PFB:F8BT film, demonstrating a unique combination of surface sensitivity and unambiguous chemical contrast.

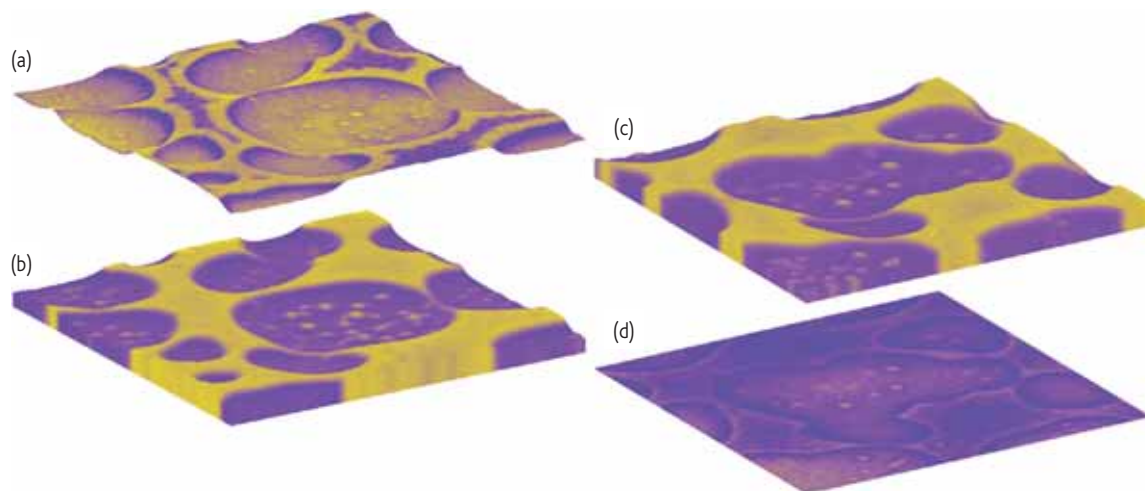


Fig. 5 Isometric rendering of two  $10 \times 10 \mu\text{m}$  sections of a PFB:F8BT blend film showing compositions and thickness variations (exaggerated by a factor of 200) of the bulk ((b), (c); from transmission data) and surface ((a) upper surface, (d) lower interface; from TEY data) layers. Adopted from reference<sup>53</sup>.

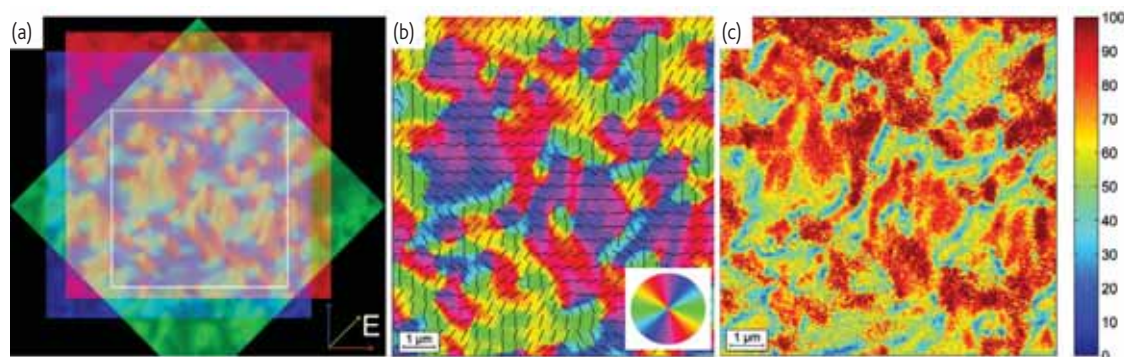


Fig. 6 (a) A series of STXM images of an annealed F8BT film measured at 285 eV displaying linear dichroic contrast due to the relative angle between the electric field vector of the x-ray beam and the C 1s  $\rightarrow$   $\pi^*$  transition moment of the F8BT molecules. (b) Plot of the in-plane orientation of the F8BT C 1s  $\rightarrow$   $\pi^*$  resonance at 285 eV (color) and the inferred orientation (and estimated fully extended length) of the F8BT backbone (black lines). (c) Plot of the calculated percentage of local molecular order, including inferred information from the out-of-plane direction. Adopted from<sup>39</sup>.

These images confirm the presence of the PFB-rich wetting and capping layers previously deduced by a combination of techniques while also providing valuable new information that show how the films structure reduces performance in photovoltaic devices. The PFB-rich partial capping layer appears blotchy in the TEY STXM images, with the more intense regions coinciding with the bulk PFB-rich subdomains; indeed, it appears that the partial capping layer is pinned by the bulk PFB-rich subdomains. This tells us that the capping layer has a thickness similar to the electron escape depth ( $\sim 2.5$  nm)<sup>62</sup> and that the partial capping layer is connected to the bulk PFB-rich subdomains. Combined with the PFB-rich wetting layer, this indicates that the PFB-rich subdomains are connected to both electrodes and thus constitute a short between the electrodes. Similarly, the F8BT-rich subdomains are observed to be connected to the upper surface as well as punching through the PFB-rich wetting layer and thus also constitute a short that reduces the device efficiency. Armed with a new source of comprehensive information via TEY STXM, researchers can now follow a systematic and rational design strategy to further optimize polymer nanostructures and polymer photovoltaic device performance.

Many organic materials exhibit strongly anisotropic mechanical, optical and/or electrical properties. In these cases, the ability to image their orientational texture can enable the engineering of improved methods of exploiting the unique properties of these materials. A number of methods have been recently developed to image the orientational texture of organic materials utilizing optical, electron (transmission), scanning probe and also soft x-ray microscopies<sup>63</sup>. In soft x-ray STXM, such materials tend to show linear dichroism effects whereby the x-ray absorption of the material varies depending on the orientation of the molecules with respect to the electric field vector of the linearly polarized x-ray probe beam. Such linear dichroism contrast is exemplified in Fig. 6a with overlaid images of an annealed F8BT film measured at azimuthal rotations of 0° (red), 45° (green), and 90° (blue). Fitting this data to a physical model allows the extraction of a molecular orientation map as presented in Fig. 6b. Further analysis allows one to also elucidate the out-of-plane components and thus map the molecular conformation in a three dimensional sense, including the local degree of molecular order, as shown in Fig. 6c. This information will be

valuable in engineering F8BT based devices such as field effect transistors, where control of the molecular orientation has been shown to improve device performance<sup>64</sup>, and lasers, where changes in refractive index due to domain orientations cause scattering losses in the laser light<sup>65</sup>. Similar orientational analysis of organic devices has been performed on pentacene devices by Hub *et al.*<sup>41</sup> and Brauer *et al.*<sup>40,66</sup>

In addition to organic devices, blends of polymers with complementary properties offer a general opportunity of creating materials with enhanced performance. While traditional methods have used copolymer compatibilizers to strengthen polymer blends, recent advances in nanoengineering have resulted in the development of nanosized inorganic components that can be used to improve, for example, the flammability and mechanical properties of the blends<sup>2,67-69</sup>. When using such nanosized additives, sophisticated characterization methods are required to establish structure-property relationships. A recent study by Zhang *et al.*<sup>70</sup> utilized STXM and other methods to demonstrate that inorganic, nanosized filler additives can serve as a universal, non-specific compatibilizer that can localize to the interface between the polymers. A series of nanosized fillers with varying aspect ratios, ranging from nanotubes to nanoclays, were used to modify the morphology of polystyrene (PS)/poly(methyl methacrylate) (PMMA) model blends and bilayers. A particularly instructive experiment involved the comparison of PS/PMMA bilayer evolution as a function of processing, in which 7 % clay was dispersed in the PMMA. In Fig. 7, quantitative PS maps of such bilayers are presented after annealing at 170°C for 72 hr. In one case, the mixed PMMA:clay layer was pre-annealed and subsequently showed much coarser morphologies than the bilayer without pre-annealing. This directly indicates that the clay surfaces are saturated with strongly adsorbed PMMA when pre-annealed and thus lose their ability to compatibilize the unstable bilayer system. In contrast, the single post-annealing protocol allowed for the creation of some PMMA/clay/PS block copolymer-like nano-grafts that exhibited compatibilization properties as evidenced by the smaller domains observed. These results indicate that the compatibilization is a general phenomenon that should occur with all large aspect ratio nanofiller additives<sup>70</sup>.

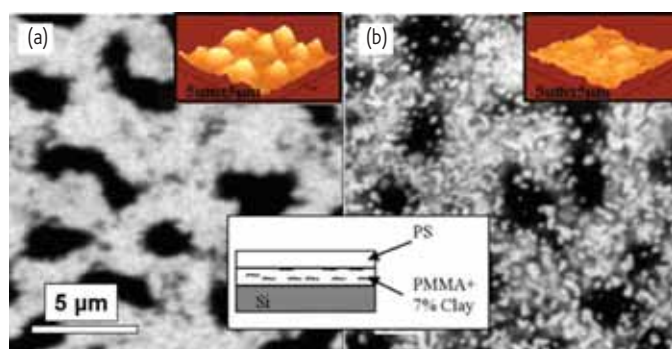


Fig. 7 STXM maps of the PS concentration and corresponding scanning probe microscopy topographs (insets) for bilayer films of PS and PMMA with 7 % Cloisite 6A clay annealed at 170 °C for 72 hr. (a) The PMMA/clay layer was pre-annealed for 24 hr at 170 °C before being covered with the PS layer. (b) The PMMA/clay layer was spun cast onto Si and the PS layer was floated immediately on top of it. STXM images are 15 mm × 15 mm. Adopted from<sup>70</sup>.

In some instances, materials systems are very complex and it is well advised to use many tools to characterize them. Due to their complexity, sometimes no specific, well formulated scientific hypothesis exists when characterization is undertaken and unexpected surprises are often discovered. Similarly, industrial processes are invented or modified and analytical methods are used to simply figure out what has been produced. One such example is FT30-type thin film composite membranes used for reverse osmosis water purification. This membrane consists of three primary layers. First, a paper-like non-woven support layer of poly(ethylene terephthalate) (PET). The second layer is a polysulfone grown over the PET by a process that forms pores. Finally, a layer of polyamide is grown on top of the polysulfone by interfacial polymerization. This third layer provides the discrimination between water and solutes. With a remarkably thin polyamide layer in use these days and further surface modifications of the polymers, these membranes are very difficult to analyze. Mitchell *et al.*<sup>71</sup> have shown that STXM can determine the spatial distribution of polyamide and polysulfone in such membranes. They have also reported the detection of an unexpected phases that was identified as a homopolymer of metaphenylene diamine (MPD) that forms in MPD solutions and can be

incorporated into the discrimination layer during the interfacial reaction with the trimesic acid chloride that is used to produce the nominal polyamide layer. The detection of this polyMPD contamination in the polyamide was only made possible by STXM: at less than 8 % of the membrane's active layer, this second phase had no effect on the flux or salt passage. At higher levels, however, a change in the membrane properties would most likely occur and the presence of the polyMPD would have to be controlled and could be monitored with STXM.

Characterization of synthetic soft matter with transmission NEXAFS microscopy in a STXM are broad ranging. Studies other than those highlighted above have encompassed crystallization and bond orientation in various homo-materials such as polyethylene thin films<sup>72-74</sup> and various fibers/nanotubes<sup>37,38,75,76</sup>, as well as compositional characterization of organic and organic/inorganic blends<sup>2,51,70,77-81</sup>, organic devices<sup>82,83</sup>, carbon nanotubes<sup>84</sup>, microballoons/sphere<sup>85-88</sup>, nanoparticles<sup>21,55,89</sup>, and gels/micro-gels<sup>90-92</sup>. Some microcapsules have also been investigated with TXM using primarily elemental contrast<sup>93,94</sup>.

X-rays are ionizing radiation and radiation damage can prevent the acquisition of high quality data even in a STXM in some special cases of particular sensitive materials. Explicit studies of damage as a function of chemical function group<sup>6</sup> and in comparison to electron microscopy<sup>5,7</sup> have been performed. Polyol based materials are particularly sensitive<sup>80</sup> as are materials dispersed in solutions<sup>90</sup>. While damage is not yet a major issue presently for STXM characterization, as the spatial resolution improves, so does the dose required to acquire the data.

A promising, but not yet frequently employed method is spectro-tomography in a STXM, which has excellent spectroscopic resolution and the ability to analyze wet specimens<sup>95</sup>. The dose required for a STXM tomograph is ~200 MGy, which is considerably lower than what is required for TXM tomography (typically 1 – 10 GGy), albeit at the cost of much longer acquisition times. It is important to note that cryo-techniques will not be successful in preserving the NEXAFS of polymers. Cryo only prevents mass loss, but the spectroscopic changes due to chemical damage are essentially unmitigated by cryo techniques<sup>96</sup>.

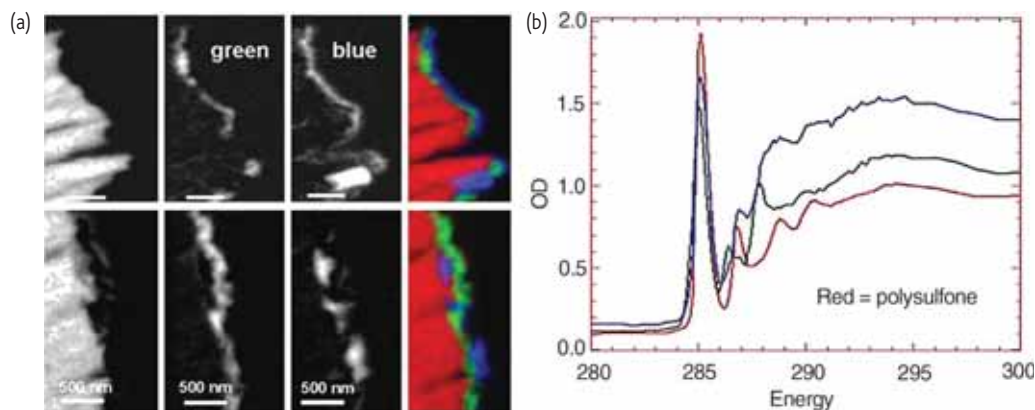


Fig. 8 (a) STXM maps of two different regions of a FT30 membrane. The spectra in the graph in (b) were extracted from selected areas and used to calculate the composition maps. The red spectrum indicates the polysulfone layer. The blue and green areas are different phases of the polyamide coating. Reproduced from<sup>71</sup> with permission from Elsevier.

## Insights from soft x-ray scattering

Unfortunately, NEXAFS microscopy does not always have the spatial resolution required to assess the finer details that might be present at the nanometer scale in many organic materials. In isolated cases on high contrast samples and use of high photon energy, the visibility limit of STXM has been pushed to  $\sim 10$  nm<sup>97</sup>. For quantitative analysis and lower contrast organic materials, the practically achievable spatial resolution is typically  $\sim 50$  nm. This depends somewhat on the precision required. Generally, the modulation transfer function of the microscope suppresses the contrast and hence impacts the composition computed even for features larger than 200 nm. In a number of cases, R-SoXS has proven to be an invaluable complement to NEXAFS microscopy by extending the spatial resolution of the compositionally sensitive soft x-ray methods down to the few nm range without suffering from the complications introduced by a modulation transfer function. The reasons for using R-SoXS rather than conventional SAXS for these applications is enhanced compositional sensitivity and contrast, mirroring the general advantages of NEXAFS microscopy. The sensitivity of scattering to the small length scale is particularly pronounced in  $\theta$ - $2\theta$  reflectometry geometry, where 0.1 nm sensitivity to interfacial roughness can be achieved<sup>43,58,98,99</sup>. After the initial demonstrations and applications involving nanoparticles and bilayer model systems<sup>21,22,43</sup>, most of the recent applications of these methods have focused on characterizing organic devices<sup>58,59,98,100-102</sup>. Another application of R-SoXS is the characterization of block copolymers (BCP)<sup>103,104</sup>, which we will use here to demonstrate the energy dependent selective contrast of R-SoXS.

In BCPs, compositionally distinct blocks of polymers are covalently joined, which can self-assemble into ordered structures, including lamellae, hexagonally packed cylinders, body-centered cubic packed spheres, and bicontinuous gyroids. These structures, which can be reliably and precisely reproduced, allow the use of BCPs as templates and scaffolds by selective removal of one component. ABC-type triblock copolymers offer a wealth of periodic morphologies, however have been little studied, due to the demanding synthesis and the complexity of their morphologies. Yet to fully realize the potential of ABC BCPs, it is essential to understand their morphologies and the parameters that control their ordering.

R-SoXS was a critical tool in revealing a novel morphology of the triblock copolymer poly(1,4-isoprene)-block-polystyrene-block-poly(2-vinyl pyridine) (IS2VP) in the bulk and in thin films. Panels (a) and (b) of Fig. 9 display  $\delta$  and  $\beta$  of poly(1,4-isoprene) (PI - blue solid line), polystyrene (PS - red dashed line), and poly(2-vinyl pyridine) (P2VP - green dotted line), the constituent blocks of IS2VP. Since the x-ray scattering power is proportional to  $\Delta\delta^2 + \Delta\beta^2$ , the relative scattering contribution of the different blocks can be isolated by judicious choice of photon energy. Consequently, the R-SoXS data of an IS2VP bulk sample exhibits rather different profiles at 250, 280, and 284 eV (Fig. 9c). At 280 eV, three scattering peaks are observed that can be assigned to a hexagonally packed structure. At 250 and 284 eV, a single strong scattering peak is observed at  $0.16$  nm<sup>-1</sup> and  $0.27$  nm<sup>-1</sup>, respectively.

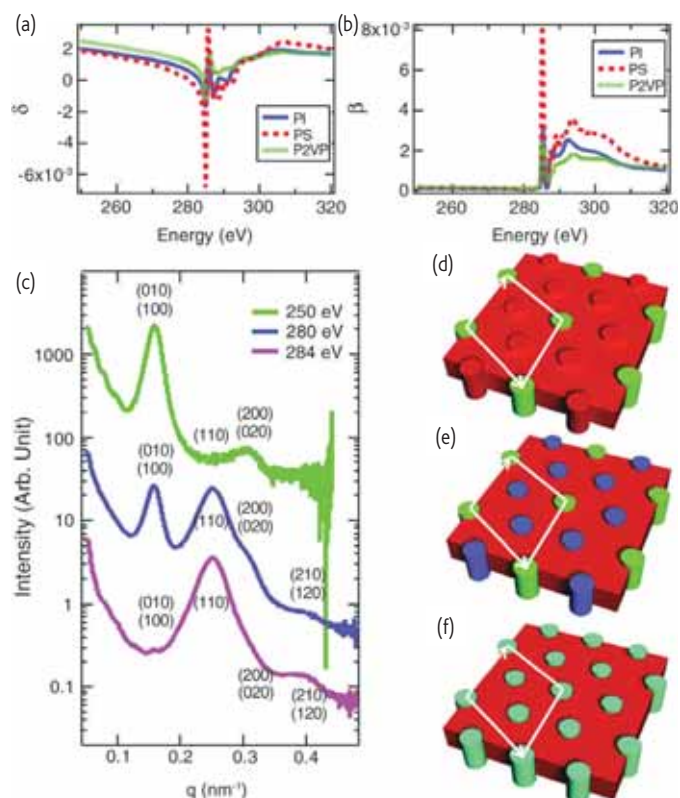


Fig. 9 (a, b) Index decrement ( $\delta$ ) and imaginary ( $\beta$ ) part of the complex index of refraction of poly(1,4-isoprene) (blue solid line), polystyrene (red dashed line), and poly(2-vinyl pyridine) (green dotted line), respectively. (c) Scattering intensity at 250, 280, and 284 eV as indicated. (d-f) Schematic illustration of hexagonally packed cylindrical morphology of IS2VP triblock copolymer as sensed by R-SoXS using 250, 280, and 284 eV photon. Reproduced from reference<sup>104</sup>.

Two lattices with rather different spacing were observed at these two energies. At 250 eV, "index-matching" between these two constituent components yields a very small x-ray scattering contrast between PS and PI. Consequently, only the lattice of the P2VP in the "PI-PS" matrix is detected (Fig. 9d). Conversely, at 284 eV, the contrast between P2VP and PI domains is minimized (Fig. 9f). At 280 eV, the index of refraction of all three polymers is different enough to yield significant contrast between any two components (Fig. 9d). By modulating the scattering profiles in this way and considering form factor effects, R-SoXS revealed two nested, hexagonal arrays of P2VP and PI cylindrical microdomains residing in the PS matrix. The cylindrical microdomains of one component are located at the interstitial sites of the hexagonal array with the larger  $d$  spacing than is formed by the other component<sup>104</sup>.

## Conclusions and perspectives

NEXAFS microscopy has made major contributions to a number of fields and material systems, including synthetic organic materials as highlighted here. Currently, soft x-ray STXMs are available at the Advanced Light Source (Berkeley, U.S.A.)<sup>48</sup>, at the Canadian Light Source (Saskatoon, Canada)<sup>105</sup>, the PolLux facility at the Swiss Light Source

(Villigen, Switzerland)<sup>47</sup>, MAXYMUS at BESSY-II (Berlin, Germany)<sup>106</sup>, at SSRF (Shanghai, China)<sup>107</sup>, and at SSRL (Menlo Park, U.S.A.). Additional facilities are planned at Soleil (Saint-Aubin, France), NSRRC (Hsinchu, Taiwan), UV-SOR (Okazaki, Japan), and Max-Lab (Lund, Sweden). These efforts should continue to improve the capabilities by pushing the spatial resolution, by further increasing the information content through novel methods (tomography<sup>95</sup>, dichroism, etc.), and by improved control of the sample environment. They will also provide increased capacity and thus improved access to a larger user community.

A method under development that should provide substantial practical improvements for the characterization of materials is x-ray ptychography<sup>108-110</sup>. In this method, diffraction patterns are recorded in a STXM at each point along the specimen (Fig. 10). Since the diffraction pattern is recorded to high scattering angles, it encodes information from features that are much smaller than the beam size. This is the same "high spatial resolution" advantage of R-SoXS. Most importantly, when diffraction patterns from overlapping sample areas are used, the phase problem of the reconstruction of the diffraction pattern can be overcome and the complete real space information, and not just the ensemble averages, can be recovered. A significant advantage of x-ray ptychography will also be that differences in  $\delta$  can be exploited, thus essentially providing efficient phase imaging at energies below an absorption edge. This will be critically important for organic materials as higher spatial resolution is increasingly needed and the radiation dose in absorption contrast would become too large. Thus, x-ray ptychography provides the opportunity for low dose phase-contrast, with high resolution real space information. It should also be well suited to the characterization of materials by being able to switch with ease the field of view, or magnification by several factors<sup>111</sup>.

Another approach to achieve "super-resolution" NEXAFS microscopy is the combination of a STXM with an AFM, as has been constructed at the NanoXAS beamline<sup>112</sup>. In this instrument, a zone plate focuses an x-ray beam onto a thin sample mounted on a rastered scanning stage. The x-rays pass through the sample, generating electrons with each absorption event and the electrons generated close to the rear surface of the sample are able to escape the sample and be collected by the nearby tip. As illustrated schematically in Fig. 11, shielding of the tip with a biased metallic coating will allow the tip to only collect electrons emitted from a restricted area, which can be smaller than the x-ray illuminated area. Thus, the NanoXAS instrument can take advantage of the excellent x-ray derived contrast mechanisms, as well as the excellent spatial resolution of scanning probe microscopy. NanoXAS is currently in the commissioning phase and some initial data involving consecutive AFM topography and x-ray transmission images of the same area of a polystyrene (PS) and poly(methyl methacrylate) (PMMA) blend film is presented in Fig. 11.

As delineated, soft x-ray microscopy and scattering are a dynamically evolving field with unique attributes that are expanding in a number of new and exciting directions. Given the unique contrast mechanisms,

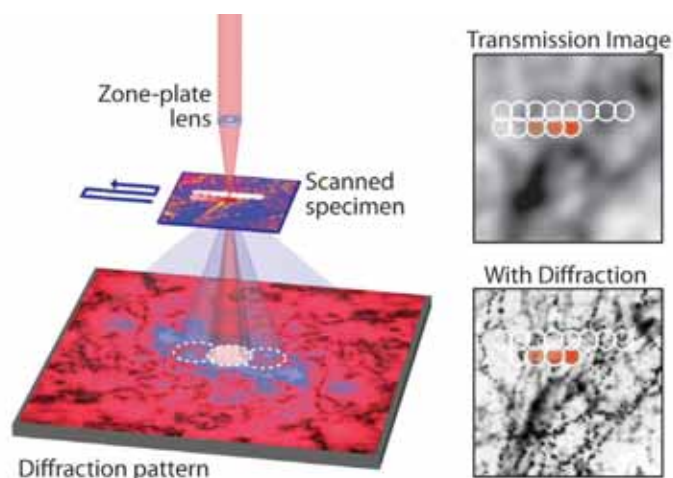


Fig. 10 Illustration of the principles of x-ray ptychography. (left) Recording of a sequence of diffraction patterns in a STXM with a pixilated detector. Simulated images when the diffraction pattern is used (lower right) and total transmission plotted as a function of beam position (upper right). The circles on the right represent the nominal spatial resolution without the diffraction enhancement. From<sup>111</sup>. Reprinted with permission from AAAS.

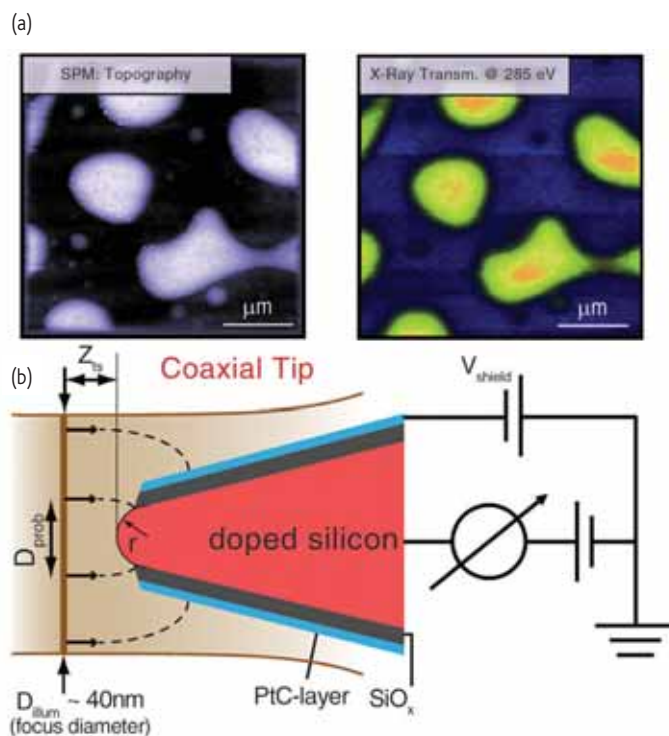
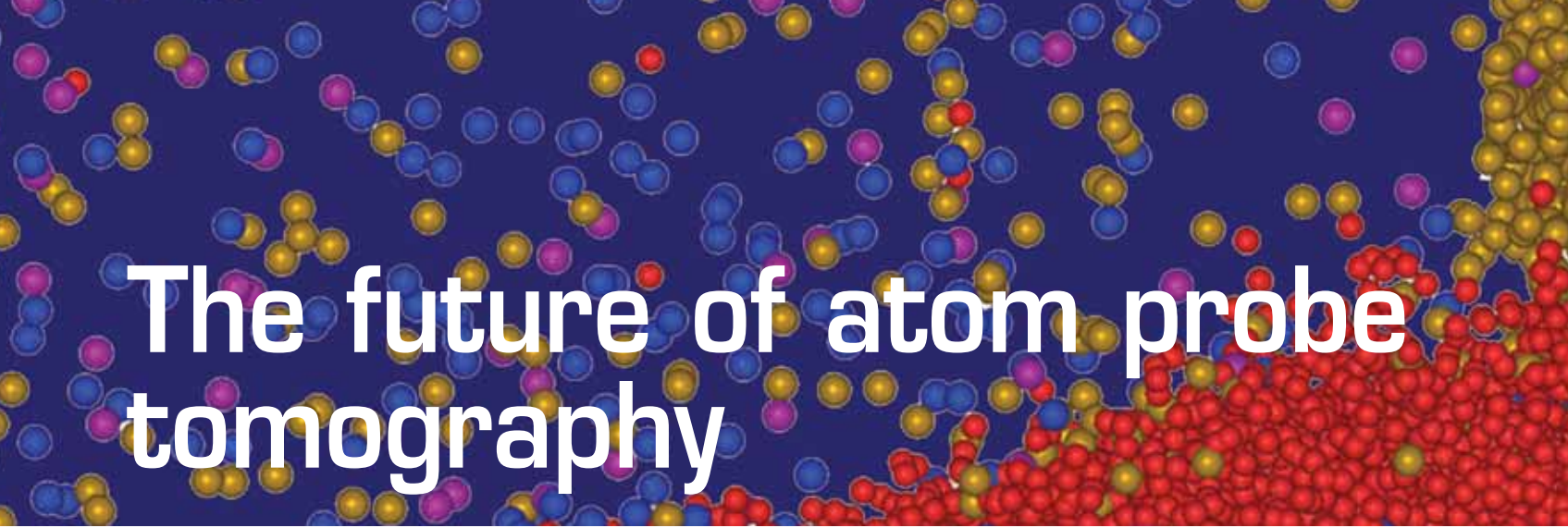


Fig. 11 (a) Consecutive AFM and STXM measurements of the same region of a PS:PMMA polymer blend film. (b) Super-resolution concept for the NanoXAS instrument using a coaxial tip to collect x-ray generated electrons from an area of the sample surface that is smaller than the x-ray illuminated area. Reproduced from reference<sup>112</sup>.

soft x-ray microscopy and scattering will remain a very powerful characterization method for a wide range of materials, and in particular for the synthetic organic materials that have been the primary focus here. 

## REFERENCES

- Günes, S., et al., *Chem Rev* (2007) **107**, 1324.
- Si, M., et al., *Macromolecules* (2006) **39**, 4793.
- Sawyer, L. C., Grubb, D. T. *Polymer Microscopy*; Chapman and Hill: New York, 1987.
- Roe, R. J., *Methods of X-Ray and Neutron Scattering in Polymer Science*; Oxford University Press: New York, 2000.
- Rightor, E. G., et al., *J Phys Chem B* (1997) **101**, 1950.
- Coffey, T., et al., *J Electron Spectrosc Relat Phenom* (2002) **122**, 65.
- Wang, J., et al., *J Phys Chem B* (2009) **113**, 1869.
- Kaulich, B., et al., *J Phys-Condens Matter* (2011) **23**, 083002.
- Falcone, R., et al., *Contemp Phys* (2011) **52**, 293.
- de Groot, F. M. F., et al., *ChemPhysChem* (2010) **11**, 951.
- Ade, H., et al., *Polymer* (1995) **36**, 1843.
- Ade, H., and Hitchcock, A. P., *Polymer* (2008) **49**, 643.
- Ade, H., and Stoll, H., *Nature Mater* (2009) **8**, 281.
- Stöhr, J., et al., *Science* (1993) **259**, 658.
- Guttmann, P., et al., *Nat Photon* (2012) **6**, 25.
- Ade, H., and Hsiao, B., *Science* (1993) **262**, 1427.
- Ade, H., et al., *Science* (1992) **258**, 972.
- Weiss, D., et al., *Ultramicroscopy* (2000) **84**, 185.
- Larabell, C., and Le Gros, M., *Biophys J* (2004) **86**, 185a.
- Fischer, P., et al., *J Phys D-Appl Phys* (1998) **31**, 649.
- Araki, T., et al., *Appl Phys Lett* (2006) **89**, 124106.
- Mitchell, G. E., et al., *Appl Phys Lett* (2006) **89**, 044101.
- Schöll, A., et al., *Chem Phys Lett* (2003) **370**, 834.
- Zou, Y., et al., *Chem Phys Lett* (2006) **430**, 287.
- Stöhr, J., *NEXAFS Spectroscopy*; Springer-Verlag: New York, 1992.
- Watts, B., et al., *J Chem Phys* (2011) **134**, 024702.
- Dhez, O., et al., *J Electron Spectrosc* (2003) **128**, 85.
- Kikuma, J., and Tonner, B. P., *J Electron Spectrosc Relat Phenom* (1996) **82**, 53.
- Cook, P. L., et al., *J Chem Phys* (2009) **131**, 2547.
- Hitchcock, A. P., and Mancini, D. C., *J Electron Spectrosc Relat Phenom* (1994) **67**, 1.
- Urquhart, S. G., Ade, H., *J Phys Chem B* (2002) **106**, 8531
- Urquhart, S. G., et al., *J Phys Chem B* (1997) **101**, 2267.
- Wang, J., et al., *J Electron Spectrosc* (2009) **170**, 25.
- Ade, H., et al., *Appl Phys Lett* (1998) **73**, 3775.
- Morin, C., et al., *J Electron Spectrosc* (2001) **121**, 203.
- Hub, C., et al., *Rev Sci Instrum* (2010) **81**, 033704.
- Smith, A. P., and Ade, H., *Appl Phys Lett* (1996) **69**, 3833.
- Rousseau, M. E., et al., *J Am Chem Soc* (2007) **129**, 3897.
- Watts, B., et al., *Adv Funct Mater* (2011) **21**, 1122.
- Brauer, B., et al., *Chem Mat* (2010) **22**, 3693.
- Hub, C., et al., *J Mater Chem* (2010) **20**, 4884.
- Materlik, G., et al. *Resonant anomalous x-ray scattering: theory and applications*; North-Holland: Amsterdam; New York, 1994.
- Wang, C., et al., *Appl Phys Lett* (2005) **87**, 214109.
- Swaraj, S., et al., *Eur Phys J - Spec Top* (2009) **167**, 121.
- Mezger, M., et al., *Phys Rev B* (2011) **83**, 155406.
- Rarback, H., et al., *Rev Sci Instrum* (1988) **59**, 52.
- Raabe, J., et al., *Rev Sci Instrum* (2008) **79**, 113704.
- Kilcoyne, A. L. D., et al., *J Synchrotron Radiat* (2003) **10**, 125.
- Lerotic, M., et al., *J Electron Spectrosc* (2005) **144**, 1137.
- Ade, H., et al., *Europhys Lett* (1999) **45**, 526.
- Slep, D., et al., *Langmuir* (1998) **14**, 4860.
- Koprinarov, I. N., et al., *J Phys Chem B* (2002) **106**, 5358.
- Watts, B., and McNeill, C. R., *Macromol Rapid Comm* (2010) **31**, 1706.
- Cadby, A. J., et al., *Adv Mater* (2007) **19**, 107.
- Burke, K. B., et al., *Nanotechnology* (2011) **22**, 265710.
- McNeill, C. R., et al., *Macromolecules* (2009) **42**, 3347.
- McNeill, C. R., et al., *Nanotechnology* (2008) **19**, 424015.
- Yan, H., et al., *Adv Funct Mater* (2010) **20**, 4329.
- Swaraj, S., et al., *Nano Lett* (2010) **10**, 2863.
- Chiesa, M., et al., *Nano Letters* (2005) **5**, 559.
- Kim, J.-S., et al., *Macromolecules* (2004) **37**, 2861.
- Chua, L.-L., et al., *Langmuir* (2006) **22**, 8587.
- McNeill, C. R., *J Polym Sci B: Polym Phys* (2011) **49**, 909.
- Zaumseil, J., et al., *Adv Funct Mater* (2008) **18**, 3630.
- Gwinner, M. C., et al., *Adv Funct Mater* (2009) **19**, 1360.
- Brauer, B., et al., *Organ Electron* (2011) **12**, 1936.
- Zhang, W., et al., *Polymer* (2003) **44**, 2109.
- Zhang, W. H., et al., *Macromolecules* (2002) **35**, 8029.
- Pack, S., et al., *Macromolecules* (2010) **43**, 5338.
- Zhang, W., et al., *Polym Advan Technol* (2011) **22**, 65.
- Mitchell, G. E., et al., *Polymer* (2011) **52**, 3956.
- Wang, Y. T., et al., *Macromolecules* (2010) **43**, 8153.
- Wang, Y., et al., *Phys Rev Lett* (2006) **96**, 028303.
- Wang, Y., et al., *Macromolecules* (2004) **37**, 3319.
- Hernández Cruz, D., et al., *Biomacromolecules* (2006) **7**, 836.
- Najafi, E., et al., *Small* (2008) **4**, 2279.
- Slep, D., et al., *Langmuir* (2000) **16**, 2369.
- Smith, A. P., et al., *Polymer* (2000) **41**, 6271.
- Smith, A. P., et al., *Macromolecules* (2000) **33**, 2595.
- Rightor, E. G., et al., *Macromolecules* (2002) **35**, 5873.
- Martin, Z., et al., *J Phys Chem B* (2009) **113**, 11160.
- Watts, B., et al., *Macromolecules* (2009) **42**, 8392.
- Collins, B. A., et al., *J Phys Chem Lett* (2010) **1**, 3160.
- Felten, A., et al., *Appl Phys Lett* (2006) **89**, 093123.
- Koprinarov, I., et al., *Macromolecules* (2001) **34**, 4424.
- Croll, L. M., et al., *Macromolecules* (2005) **38**, 2903.
- Takekoh, R., et al., *Macromolecules* (2005) **38**, 542.
- Tzvetkov, G., et al., *Micron* (2008) **39**, 275.
- Li, J., et al., *J Polym Sci A: Polym Chem* (2011) **49**, 3038.
- Mitchell, G. E., et al., *Macromolecules* (2002) **35**, 1336.
- Fujii, S., et al., *Langmuir* (2009) **25**, 2588.
- Fujii, S., et al., *J Am Chem Soc* (2005) **127**, 16808.
- Köhler, K., et al., *J Phys Chem B* (2007) **111**, 8388.
- Déjugnat, C., et al., *Adv Mater* (2007) **19**, 1331.
- Johansson, G. A., et al., *J Synchrotron Radiat* (2007) **14**, 395.
- Beetz, T., and Jacobsen, C., *J Synchrotron Radiat* (2003) **10**, 280.
- Vila-Comamala, J., et al., *Ultramicroscopy* (2009) **109**, 1360.
- Wang, C., et al., *J Am Chem Soc* (2009) **131**, 12538.
- Wang, C., et al., *J Vac Sci Technol A* (2007) **25**, 575.
- Chen, D., et al., *Nano Letters* (2011) **11**, 2071.
- Chen, W., et al., *Nano Letters* (2011) **11**, 3707.
- Yan, H., et al., *J Appl Phys* (2011) **110**, 102220.
- Virgili, J. M., et al., *Macromolecules* (2007) **40**, 2092.
- Wang, C., et al., *Nano Letters* (2011) **11**, 3906.
- Kaznatcheev, K. V., et al., *Nucl Instr Meth Phys Res A* (2007) **582**, 96.
- Nolle, D., et al., *Microsc Microanal* (2011) **17**, 834.
- Xue, C., et al., *Rev Sci Instrum* (2010) **81**, 103502.
- Miao, J. W., et al., *Nature* (1999) **400**, 342.
- Rodenburg, J. M., et al., *Phys Rev Lett* (2007) **98**, 034801.
- Thibault, P., et al., *Science* (2008) **321**, 379.
- Chapman, H. N., *Science* (2008) **321**, 352.
- Schmid, I., et al., *Ultramicroscopy* (2010) **110**, 1267.



# The future of atom probe tomography

The dream of the microscopy and materials science communities is to see, identify, accurately locate, and determine the fundamental physical properties of every atom in a specimen. With this knowledge together with modern computer models and simulations, a full understanding of the properties of a material can be determined. This fundamental knowledge leads to the design and development of more advanced materials for solving the needs of society. The technique of atom probe tomography is the closest to fulfilling this dream but is still significantly short of the goal. The future of atom probe tomography, and the prospects for achieving this ultimate goal are outlined.

Michael K. Miller<sup>a,\*</sup>, Thomas. F. Kelly<sup>b</sup>, Krishna Rajan<sup>c</sup>, and Simon P. Ringer<sup>d</sup>

<sup>a</sup>Materials Science and Technology Division, Oak Ridge National Laboratory, Oak Ridge, TN 37831-6139, USA

<sup>b</sup>Cameca Instruments, Inc. 5500 Nobel Drive, Suite 100, Madison, WI 53711-4951, USA

<sup>c</sup>Department of Materials Science and Engineering, 2240K Hoover Hall; Iowa State University, Ames, IA 50011, USA

<sup>d</sup>Australian Centre for Microscopy & Microanalysis, The University of Sydney, NSW, 2006 Australia

\*E-mail: millermk@ornl.gov

History has taught us that every time a new form of microscopy or type of microscope is introduced, major advances are made in the understanding of materials. For example, the light or optical microscope introduced the world to microbes and micro-organisms around 1600 AD, and the electron microscope to dislocations in materials over 50 years ago<sup>1-3</sup>. Today many different forms of microscopy have been developed but the ultimate goal of seeing, accurately locating, and identifying all the atoms in a specimen is still elusive. Atom probe tomography and electron microscopy are the mainstays of atomic resolution microscopy of bulk materials. However, neither technique can accomplish this goal in the bulk of a specimen at the present time.

Atom probe tomography enables us to approach this goal by providing the spatial coordinates of atoms and their identities, but its spatial resolution and detection efficiency fall short of the ultimate target. Modern electron microscopes can routinely see the individual columns of atoms in crystalline materials, aid in the identification of the crystal structures from diffraction patterns, and in special cases – with the help of simulations – identify individual atoms, as well as bonding and oxidation states, and chemical, electronic, and magnetic information. Although incremental improvements in the design of current microscopes will surely occur, this level of three-dimensional resolution cannot be achieved for all atoms in a sample of a technologically interesting or important material. The need for such a microscope is

becoming increasingly important, and is possibly already critical, for the development of nanomaterials and because of the ever decreasing length scales of semiconducting devices, where the scale of interest is at the atomic level. It will take a major breakthrough to achieve the dream of microscopists to see, identify, locate, and determine the fundamental physical properties of every atom. In this review, some of the ideas regarding how this goal may be achieved are outlined.

## The roadmap of atom probe developments

The quest along the road to this ambitious goal to detect and identify individual atoms started roughly 60 years ago with the pioneering work of Prof E. W. Müller and the field ion microscope<sup>4</sup>. With this simple glass instrument, Müller and Bahadur were able to produce the first images of individual atoms in 1955<sup>5-7</sup>. Four critical experimental parameters were needed to achieve this milestone. The specimen needed to be in the form of a very sharp needle (end radius typically 50 nm) that was cryogenically cooled to which a positive electric field was applied in the presence of a trace of an image gas ( $1 \times 10^{-3}$  Pa), such as helium or neon. When the electric field, i.e., the positive voltage, is slowly increased, the helium image gas atoms near the surface are polarized and attracted to the apex of the needle. After becoming thermally accommodated to the cryogenic temperature, an electron can be removed from these atoms by an electron tunneling process, if the electric field is sufficiently high. The resulting ion produced is immediately repelled from the specimen to a phosphor screen located a few centimeters away, where it produces visible light. This process occurs all over the surface of the specimen wherever the atoms protrude slightly from the surface and the resulting map of this intensity of light is the field ion image. If the voltage on the specimen is increased further, the surface atoms of the material can be removed by a process known as field evaporation. This process can be continuously repeated to enable not only the interior of the specimen to be analyzed, but it also allows any irregularities and contamination on the surface to be removed.

Once the individual atoms had been resolved, Müller set about identifying these atoms by exploiting the process of field evaporation. Along with his co-workers Panitz and McLane, Müller built a prototype instrument in 1967 which they called an atom-probe field ion microscope (APFIM)<sup>8</sup>. This instrument incorporated a small aperture in the center of the phosphor screen which served as the entrance to a time-of-flight mass spectrometer<sup>8</sup>. In this prototype instrument, the specimen was placed on a sliding glass seal goniometer so that the image of an atom on the surface of the specimen could be aligned with this circular aperture. Then a voltage pulse of amplitude,  $V_p$ , was superimposed on the standing voltage,  $V_t$ , to remove the atom of interest and simultaneously trigger an oscilloscope scan which was monitoring the output from the single atom sensitive detector at the end of the mass spectrometer. The mass-to-charge state ratio,  $m/n$ , and hence the identity of the atom was determined from the flight time,  $t$ , and distance,  $d$ , and the total applied voltage due to the equivalence of the potential energy of the ion just

prior to field evaporation,  $neV = ne(V_t + V_p)$ , to its kinetic energy that it acquire after leaving the specimen,  $\frac{1}{2}mv^2$ , where  $e$  is the electronic charge, and  $v$  the speed of the ion. Therefore, the mass-to-charge state ratio,  $m/n = 2e(V_t + V_p)t^2/d^2$ . The mass resolution of the early instruments was limited by small variations in the energy acquired during the field evaporation event. This limitation was solved by the incorporation of an energy-compensating lens into the mass spectrometer<sup>9,10</sup>. With this lens and the nature of the time-of-flight mass spectrometer, all elements could be detected with equal sensitivity and the instrument had sufficient mass resolving power to identify their isotopes. When small computers became available, computer-controlled digital timing systems were added to automate the experiment and data collection. The first commercial atom probe field ion microscope, the VG FIM100, was introduced in 1985<sup>11</sup>. The potential for this instrument for near atomic scale materials characterizations was immediately recognized by materials scientists<sup>12</sup>.

During this period, Kellogg and Tsong<sup>13</sup> implemented an alternative method to remove atoms from the specimen by applying a laser pulse to momentarily increase the temperature of the apex of the specimen so that the field due to the standing voltage was sufficient to promote field evaporation. This method did not introduce the energy variations of the voltage pulsed method so high mass resolutions were possible with long flight distances. More importantly, it has also enabled semiconducting<sup>14,15</sup> and poor-electrically-conducting materials<sup>16</sup> to be examined. The pulsed laser mode of operation opened up the application of the technique to all areas of materials science rather than just metallurgical studies.

The development of the 10 cm atom probe by Panitz<sup>17,18</sup> inspired the next generation of wide field-of-view three-dimensional atom probes<sup>19-24</sup>. The primary goal of atom probe tomography (APT) was to increase the field of view from the narrow 1 – 2 nm diameter cylinder of analysis produced in the APFIM to larger dimensions without sacrificing the spatial or mass resolutions. Several approaches were pursued successfully that used different types of position-sensitive detectors, including high speed video cameras<sup>20</sup>, wedge-and-strip anodes<sup>19</sup>, multi-anode variants<sup>21</sup>, and combinations thereof<sup>19-24</sup>. Due to the simple projection of the image, the lateral coordinates of the impact position on the detector are directly related to the coordinates of the atom on the surface of the specimen<sup>25</sup>. The third coordinate is derived from the order in which the atoms are detected<sup>25</sup>. In the some variants, an energy-compensating reflectron lenses<sup>10,26,27</sup> was incorporated into the mass spectrometer to improve the mass resolution.

The next generation of three-dimensional atom probes was stimulated by the scanning atom probe<sup>28</sup> introduced by Nishikawa *et al.* in which an electrode with a small aperture was moved across a two-dimensional rough surface. This configuration did not permit reliable materials analysis due to trajectory aberrations caused by the rough nature of the surface. However, in the local electrode atom probe, LEAP<sup>TM</sup>, a funnel-shaped aperture is positioned close to the apex of the standard needle-shaped specimen, as shown in Fig. 1<sup>29-31</sup>. As a

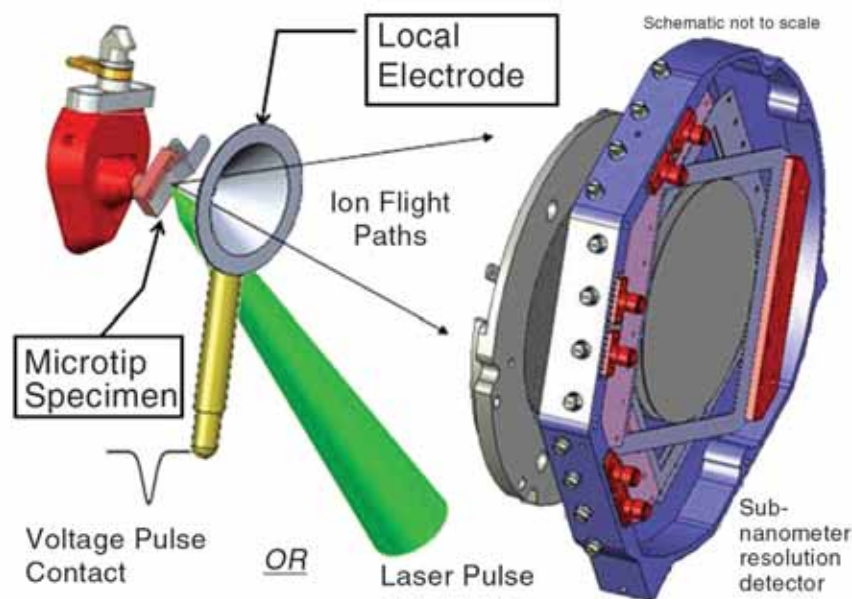


Fig. 1 Schematic diagram of a local electrode atom probe with a cryogenically-cooled multi-tip array specimen, local electrode, and crossed delay line, position-sensitive, single atom detector. Individual tips may be field evaporated with a voltage pulse superimposed on the standing voltage or by a laser pulse that momentarily increases the temperature of the apex region so that field evaporation occurs on the standing voltage.

close proximity (20 – 50  $\mu\text{m}$  separation) counter electrode with a small aperture (20 – 50  $\mu\text{m}$  in diameter) reduced the voltage required for field evaporation, the use of lower voltage pulses was practical. This enabled a new generation of solid state high voltage pulse generators with an order of magnitude higher pulse repetition rates (up to 200 kHz) and high speed position-sensitive detectors to be used which significantly reduced the data acquisition time. Both non-energy-compensated<sup>31</sup> and energy-compensated<sup>27,29</sup> versions of the LEAP® are in commercial production. This local electrode design also permitted the use of multi-tip arrays of specimens that are fabricated by ion milling methods<sup>32,33</sup> in a dual-beam focused-ion-beam (FIB)/scanning electron microscope. The three-axis nanopositioning stage permits the individual tips on the array to be aligned with the aperture so that each one can be characterized in turn. The FIB-based milling technique also enables site-specific specimens to be fabricated from regions of interest so that features, such as grain boundaries and other interfaces, phases, multilayers, or structures that are present in low volume fractions or number densities, embedded or implanted regions, etc. can be analyzed. The method also permits the volume and hence activity of irradiated materials to be minimized and enables potential new high stability materials for advanced energy systems, such as future generations of fission and future fusion reactors, to be investigated.

Atom probe tomography is a destructive technique, as it consumes the specimen during the experiment. Fortunately, this nature is mitigated because the analysis and interrogation of the data are performed after the experiment is completed. This post processing procedure allows many different types of analyses to be performed on the same data<sup>24</sup>. Some different types of data visualizations and types of analyses that are possible with atom probe tomography are shown in Figs. 2 to 5.

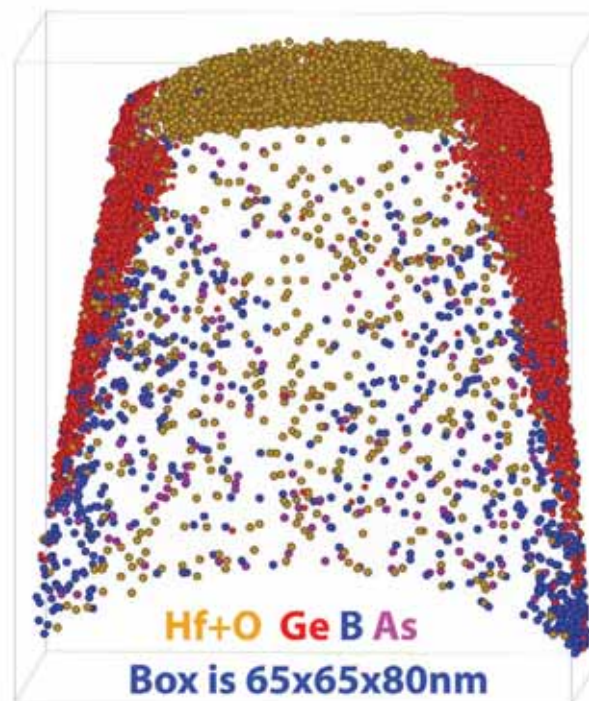


Fig. 2 The solute distributions for the gate oxide (80 at. % Hf+O 20 at. % Si), source and drain regions (25 at. % Ge maximum), and channel region of a 32 nm technology nFET transistor extracted by a focused ion beam-based technique from a commercial Intel® i5-650 microprocessor. The distributions of the B and As are clearly shown. Courtesy Dr D. J. Larson<sup>34</sup>.

The solute distributions across a 32 nm technology nFET transistor extracted by a focused ion beam-based technique from a commercial Intel® i5-650 microprocessor is shown in an atom map in Fig. 2<sup>34</sup>. The gate oxide was found to be 80 at. % Hf+O 20 at. % Si, the source and

drain regions either side of the channel region contained a maximum of 25 at. % Ge. The distributions of the B and As atoms are clearly shown in relationship to the source and drain regions. In the mechanically alloyed 14YWT nanostructured ferritic steel, Ti-, Y-, Cr- and O-enriched nanoclusters are present, as shown in Fig. 3<sup>35</sup>. The solute distribution within these 1 to 2 nm diameter nanoclusters is clearly non-uniform

with a Y-enriched core region, possibly indicating the initial nucleus. The grain boundaries are also decorated with nanoclusters and other precipitates as well as chromium and tungsten segregation, as shown in Fig. 4. The nanoclusters, precipitates, and solute segregation pin the grain boundaries and thereby minimize creep at elevated temperatures. Ultrafine 2 nm diameter copper-enriched precipitates and phosphorus

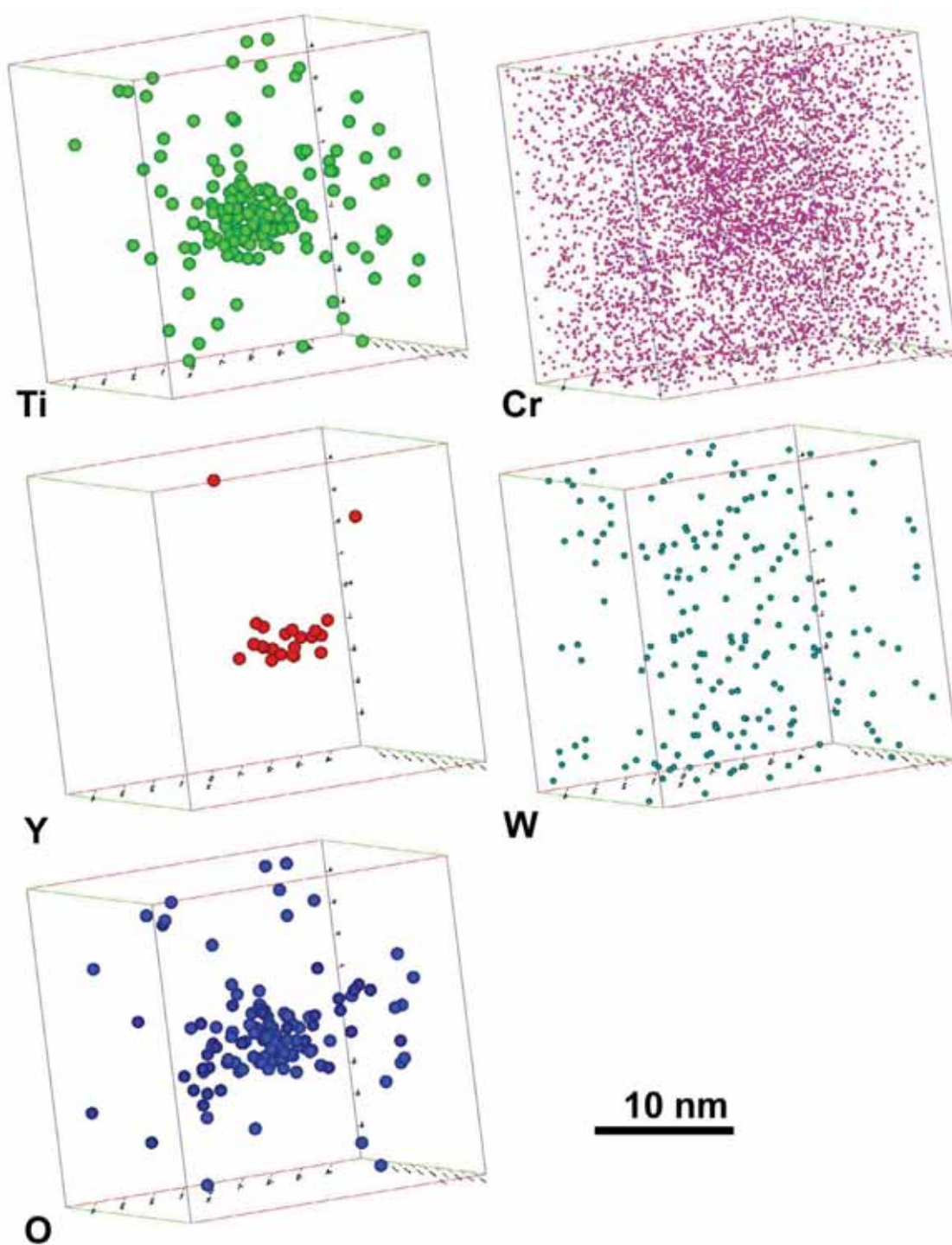


Fig. 3 A set of atom maps of a 2 nm diameter Ti-, Y-, Cr-, and O-enriched nanocluster selected from an atom probe tomography dataset of a 14YWT nanostructured ferritic steel. Each sphere represents the position of a single atom. W does not partition to the nanocluster. The extents of the Ti and O are larger than that of Y.

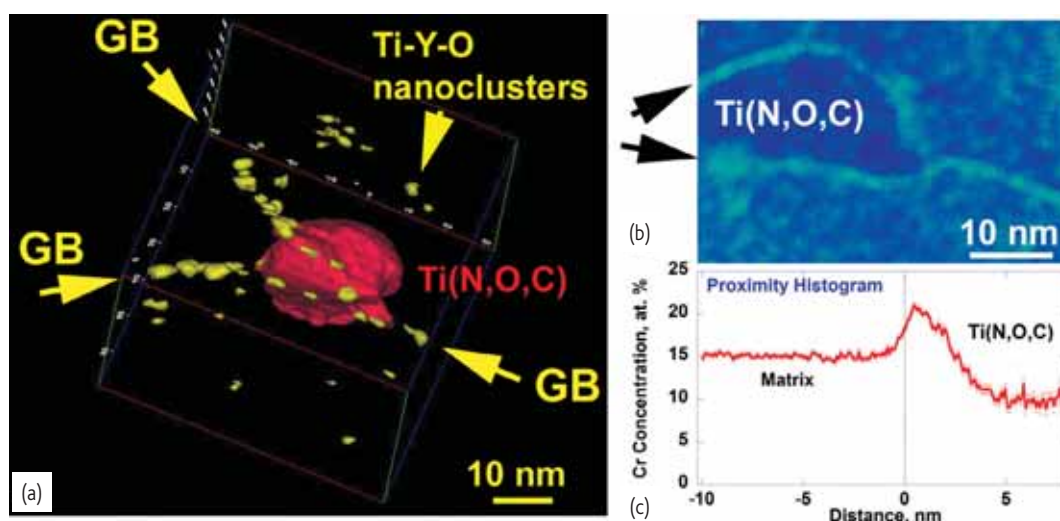


Fig. 4 (a) Isoconcentration surfaces in a 14YWT nanostructured ferritic steel revealing the nanoclusters (yellow isoconcentration surface) in the matrix and along the grain boundaries, and a (red isoconcentration surface) 20 nm diameter Ti(N,O,C) precipitate on the grain boundaries. The positions of the grain boundaries were indicated by the high number density of nanoclusters and chromium segregation. (b) A two-dimensional chromium concentration map showing chromium enrichment at the surface of the Ti(N,O,C) precipitate and along the grain boundary, and (c) a proximity histogram<sup>37</sup> quantifying the chromium enrichment at the precipitate-matrix interface.

segregation to dislocations are evident in the neutron irradiated pressure vessel steels, in Fig. 5<sup>36</sup>. These, and other examples<sup>14-16,38-45</sup> demonstrate that the state-of-the-art local electrode atom probe is a powerful instrument, capable of resolving nanoscale phases, as well as the clustering and segregation of individual atoms in complex multi-element engineering materials. The results clearly are quite stunning and demonstrate atomic resolution both spatially and elementally.

### The future of ultimate materials characterization

A tantalizing peek at the prospective future of atomic-scale microscopy is shown in Fig. 6 in which a high resolution transmission electron microscopy (HRTEM) image is juxtaposed to atom probe tomography

data from the same Al-Cu-Mg alloy. The HRTEM image provides a 3D projection image with lattice resolution along the  $\langle 110 \rangle$  zone axis, although convolutions in the scattering processes from the different elements make unequivocal, quantitative distinctions between the various atomic species impossible. This is because this alloy, and many such engineering materials of technological importance are multi-component solid solutions with a non-periodic solute architecture. The atom probe tomography data shown in Fig. 6 is a 3D tomographic image that has been oriented in a similar 'side-on' orientation to facilitate the comparison. The 3D perspective of a subset of the APT data shows the tomographic nature of the data better. The enormous possibilities for data-mining are showcased by a series of species-specific radial distribution functions, Fig. 6, whereby the relative frequency of incidence

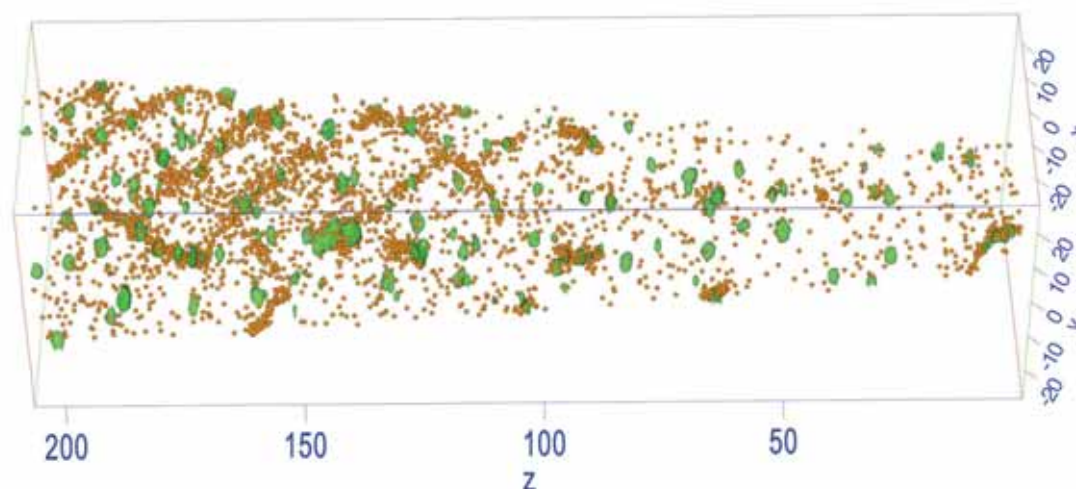


Fig. 5 Atom map of a dislocation tangle and isoconcentration surfaces of 2 nm diameter copper-enriched precipitates in a neutron irradiated pressure vessel steel. Phosphorus atoms (indicated by the brown dots) are segregated to the dislocation. The copper-enriched precipitates, denoted by the green copper isoconcentration surfaces, are also preferentially nucleated on the dislocation segments.

of particular solutes, both individual and combined, are plotted as a function of distance from the reference atom. The spatial resolution of the APT data can be improved because of the recent development of the so-called lattice rectification (LR) technique<sup>46</sup>. The potential for the atom probe to record both crystallographic and chemical information is clear, and the opportunities to hybridize APT and TEM data are the very frontier of atomic scale microscopy. Whilst we anticipate further refinements to the LR technique, there are other exciting frontier areas of atom probe besides what can be done to improve the tomographic reconstruction, most particularly in the hardware, and data analysis methods.

The most obvious hardware improvement is to increase the detection efficiency of the single atom detector to a point where every atom is detected. Current single atom detectors use a pair of microchannel plates to provide the ion-to-electron conversion and the subsequent electron multiplication process, and a crossed delay line detector (with 2 or 3 serpentine anodes) to provide the position information. The mechanical strength of current glass-based microchannel plates dictates that they have a significant area in between the channels in which the electron multiplication process occurs. The area does not contribute to the electron multiplication process so the detection efficiency is primarily defined by the open channel area which is approximately 60%. In addition, the field-defining mesh on the entrance/exit to the energy-compensating reflectron lens further reduces the detection of the ions. Therefore, nearest neighbors in the data are not necessarily nearest neighbor atoms in the sample. This uncertainty prohibits or

limits the effectiveness of certain types of analyses, such as element-specific radial distribution functions, and methods to investigate short and medium range order. The importance of detection efficiency for analyzing short range order is shown for simulated data in Fig. 7<sup>47</sup>. Larger signal-to-noise ratios would also improve the minimum detection level which is particularly important for small features. New types of microchannel plates are under development that use a stronger and thinner support structure on which a secondary electron emitting (SEE) layer of  $\text{Al}_2\text{O}_3$ ,  $\text{SiO}_2$ ,  $\text{ZrO}_2$  or  $\text{MgO}$  are atom layer deposited<sup>48</sup>. Also, new types of superconducting materials<sup>49-52</sup> may be suitable for these applications.

The mass resolution and high signal-to-noise ratio of modern instruments is currently sufficient to resolve all the isotopes of every element. However, several elements have isotopes with the same isobar, e.g.,  $^{54}\text{Fe}$  and  $^{54}\text{Cr}$ . In order to distinguish these cases, almost two orders of magnitude increase in the mass resolution would be required. It is currently not possible to achieve this increase without sacrificing detection efficiency and, in most cases, these overlaps can be deconvoluted for compositional analyses by taking into account the isotopic abundances of the other isotopes of the overlapping elements. However, it is not possible to uniquely identify the atom for these cases. As the instrument estimates the mass-to-charge state ratio, overlaps between elements in different charge states are also common and more problematical, e.g.,  $^{48}\text{Ti}^{3+}$  and  $^{16}\text{O}^+$ . Some of these cases can be distinguished from the other isotopes but in a few cases, such as  $^{28}\text{Si}^{++}$  and  $^{14}\text{N}^+$ , neither element has other isotopes in sufficient

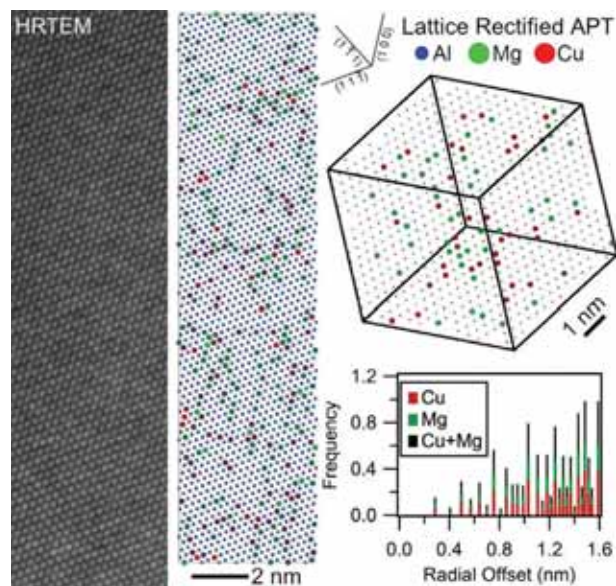


Fig. 6 Towards new frontiers in atomic resolution microscopy. High resolution transmission electron microscope (HRTEM) image and corresponding lattice-rectified atom probe tomography from an Al-Cu-Mg alloy. The precise solute architecture is available both for visualization and mathematical analysis by, for example, radial distribution functions for the individual species. The APT data and analyses are courtesy of Drs Michael Moody and Leigh Stephenson of The University of Sydney.

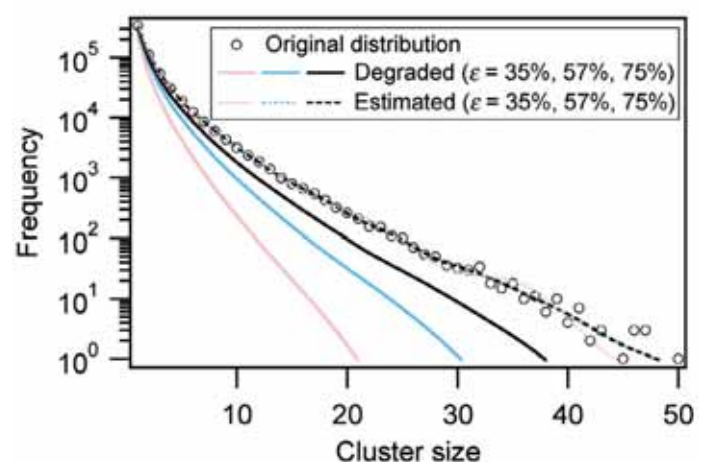


Fig. 7 The cluster-size frequency distribution within simulated APT data were calculated from model data wherein the solute exhibits a short-range order parameter of  $\alpha = 0.10$ . Cluster 'size' is measured in number of atoms. Thus, the effects of detector efficiency,  $\epsilon$ , on cluster analysis is modeled. It is seen that decreasing detector efficiency reduces both the distribution and measured size of observed clusters. Using expectation-maximisation methods to fit a mixture of binomial distributions, an estimation of the original distribution can be deconvoluted from APT measurements and the success of this approach in the simulated data is demonstrated by the convergence between the 'estimated' and 'original' distributions. Courtesy Dr Leigh Stephenson, University of Sydney.

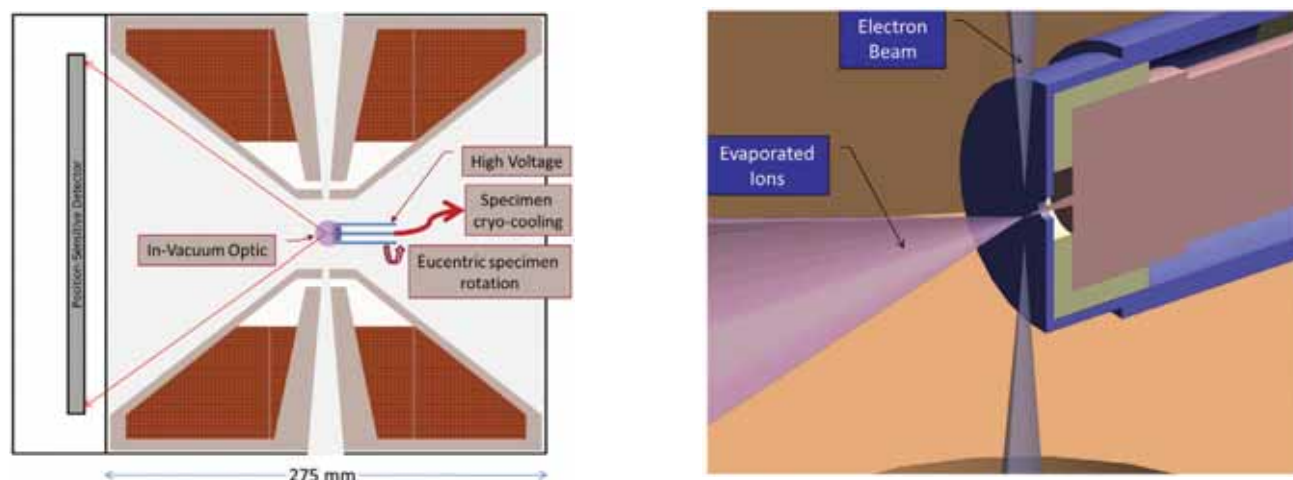


Fig. 8 Conceptual drawing of the components of a local electrode atom probe installed within the polepiece of an ultra-high vacuum scanning transmission electron microscope. The needle-shaped specimen is mounted on the central connection to the stage and protrudes through the local electrode. Field evaporation is performed either by laser pulsing (not shown) the cryogenically-cooled atom probe specimen or voltage pulsing the local electrode.

abundances for this deconvolution procedure to be fully quantifiable. This problem is further complicated by the occurrence of  $MX^{n+}$  ions, where M is a metal atom and X is a C, N, or O atom. As these ions have different charge states, they also have different kinetic energies. Therefore, as suggested by Kelly<sup>53</sup>, new types of single-atom sensitive detectors that can also measure the kinetic energy would be able to distinguish these cases. If kinetic energy resolution is available, ions that evaporate on the pulse could be distinguished from those ions that evaporate on the standing voltage and appear as noise. Filtering may be able to eliminate the need for background noise subtraction and thereby improve the signal-to-noise ratio and hence the quality of the composition determinations. In addition, the background noise atoms from random field ionization and evaporation of residual gas atoms in the vacuum system could be used to produce digital field ion images which could provide information on the shape of the surface of the specimen at the time of the evaporation of each ion. This information would enable more accurate reconstructions of the atom positions and improve the spatial resolution.

One of the most serious deficiencies of the technique that limits the spatial resolution is the quality of the reconstruction algorithm for the atom positions combined with the exact nature of the field evaporation process and the resulting trajectories of the ions as they leave the surface. The current reconstruction method is based on an algorithm developed by Blavette *et al.*<sup>54</sup> and Bas *et al.*<sup>25</sup> that assumes the specimen has a hemispherical end cap. However, some additional refinements for the wider field-of-view have been incorporated and proposed<sup>54-60</sup>. A recent analysis of the origins of resolution in atom probe tomography demonstrate that the resolution is anisotropic, as may be expected in a truly 3D technique: it is routinely below 0.15 nm in the lateral x-y direction and routinely below 40 pm in the depth direction for some materials<sup>59</sup>. However, the spatial resolution is not quite to the level where the crystal structure can be determined. The well-known issues of

the different evaporation fields of second phases and the resulting local magnification effects<sup>61</sup> together with their different atomic densities and crystal structures, and trajectory aberrations at the atomic terraces of crystallographic poles and zone lines have not been successfully solved.

A bold concept has been suggested to improve the spatial resolution by combining a local electrode atom probe (LEAP<sup>®</sup>) into the objective lens of a scanning transmission electron microscope (STEM)<sup>62</sup>, as shown in Fig. 8 and to improve the detection efficiency through the use of new types of single atom position-sensitive detectors. The resulting instrument, called the atomscope, would take advantage of the two data streams to reproduce a volume that is close to achieving the ultimate goal of detecting, identifying and correctly positioning all the atoms in the sample as well as determining the bonding and oxidation states, and obtaining chemical, electronic, and magnetic information. It is envisaged that the atomscope could be used in at least four unique modes of operation in addition to conventional stand-alone operation as a STEM and a LEAP. In all modes, an initial STEM characterization is performed to evaluate the features of interest in the microstructure and the suitability of the specimen for further analysis. Mode I: an asynchronous experiment would involve performing the TEM characterization followed by the destructive APT experiment. In this mode, there are no limitations on the type of STEM experiments that may be performed prior to the APT characterization, and these experiments might include electron tomography, phase identification, or characterization of the general microstructural, grain boundaries, dislocations, etc. Mode II: a user-driven asynchronous experiment would consist of repetitions of short sections of electron tomography combined with other types of characterizations as appropriate (electron energy loss spectroscopy (EELS), energy dispersive spectroscopy (EDS), high resolution electron microscopy (HREM), diffraction, high angle angular dark field (HAADF), etc.) followed by short sections of APT. This mode should result in sub-nanometer resolution three-

dimensional datasets. Mode III: a more time-intensive experiment that would involve sequential collection of both streams of data under full computer control. In this sub-Ångstrom resolution mode, a time-sliced method would be applied to perform short sequences of electron tomography, including HREM and/or surface profiling, followed by short APT sections. Mode IV: a synchronous experiment would involve the simultaneous and continuous EDS/EELS or spectrum imaging of the near-surface regions of the sample while analyzing the sample by APT. However, at this point, the influences of the positive voltage on the needle-shaped specimen during electron microscopy and of the up to 200 keV electron beam on the APT experiment are largely unknown<sup>63</sup>. Not only would this volume of material be suitable for the standard data analysis methods, but it could also be used as the input data to modern modeling methods and simulations so that the properties of the material could be predicted and experimentally verified. Informatics-

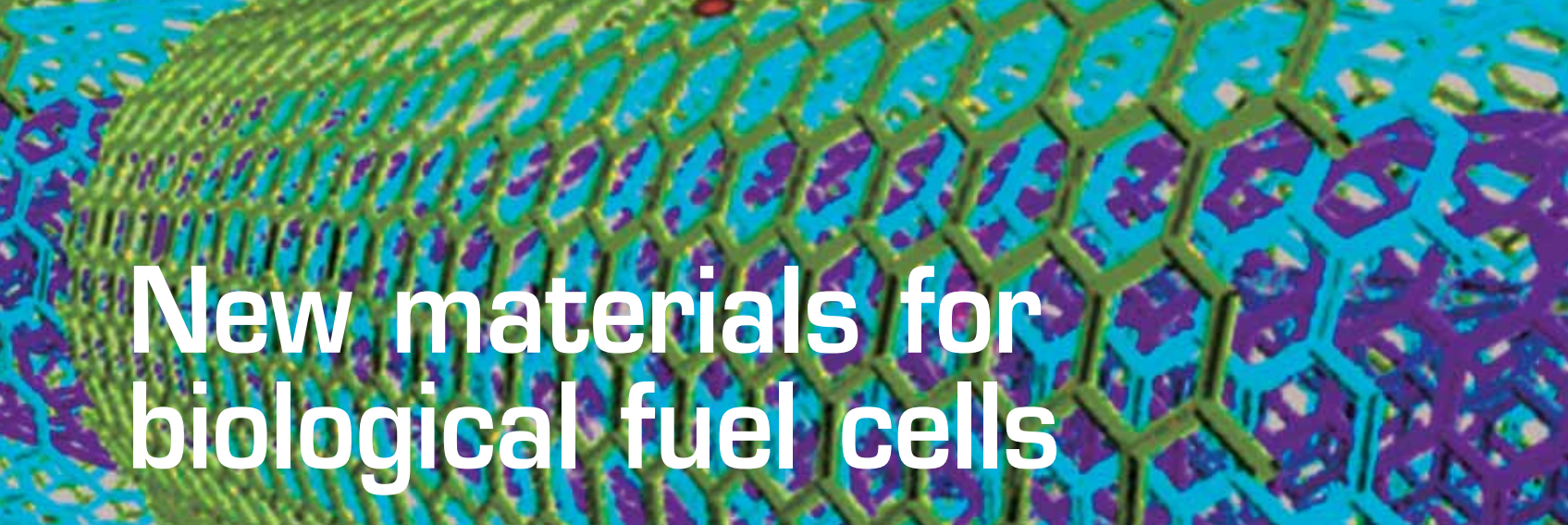
based computational strategy is critical to address the uncertainty and high dimensionality of parameters influencing image formation and spatial/chemistry correlations in the data streams<sup>64</sup>. We anticipate that this new concept instrument has the potential to herald a new era in microscopy, as the dream of every atom in three dimensions starts to be realized, enabling a merger between microscopy and computational modeling approaches. 

## Acknowledgements

*MKM and atom probe tomography were supported by ORNL's Shared Research Equipment (ShaRE) User Facility, which is sponsored by the Office of Basic Energy Sciences, US Department of Energy. MKM was also sponsored by the Materials Sciences and Engineering Division, Office of Basic Energy Sciences, U.S. Department of Energy. SPR acknowledges support from the Australian Research Council and technical and scientific support from ammr.org.au.*

## REFERENCES

- Hirsch, P. B., et al., *Philos Mag* (1956) **1**, 677.
- Bollmann, W., *Phys Rev* (1956) **103**, 1588.
- Hirsch, P., et al., *Philos Mag* (2006) **86**(29-31), 4519.
- Müller, E. W., *Z Phys* (1951) **31**, 136.
- Müller, E. W., *Z Naturforsch* (1956) **11a**, 88.
- Müller, E. W., *J Appl Phys* (1956) **27**, 474.
- Melmed, A. J., *Appl Surf Sci* (1996) **94/95**, 17.
- Müller, E. W., et al., *Rev Sci Instrum* (1968) **39**, 83.
- Poschenrieder, W. P., *Int J Mass Spectrom Ion Phys* (1972) **9**, 83.
- Kudryavtsev, A. N., et al., *Sov Tech Phys Lett* (1989) **15**, 261.
- Cerezo, A., et al., *J de Physique*, (1984) **45**(C2) 329.
- Miller, M. K., et al., *Atom Probe Field Ion Microscopy*, Clarendon Press, 1996, pp. 377-473.
- Kellogg, G. L., and Tsong, T. T., *J Appl Phys* (1980) **51**, 1184.
- Inoue, K., et al., *Ultramicroscopy*, (2009) **109**, 1479.
- Galtrey, M. J., et al., *Phys Stat Sol B* (2008) **245**, 861; *J App Phys* (2008) **104**, 861; *Appl Phys Lett* (2008) **92**, 041904.
- Marquis, E. A., et al., *Materials Today* (2010) **13**(10), 42.
- Panitz, J. A., *Rev Sci Instrum* (1973) **44**, 1034.
- Panitz, J. A., Field desorption spectrometer, US Patent No. 3,868,507, 1975.
- Cerezo, A., et al., *Rev Sci Instrum* (1988) **59**, 862.
- Miller, M. K., *Surf Sci.* (1992) **266**, 494.
- Deconihout, B., et al., *Appl Surf Sci* (1993) **67**, 444.
- Cerezo, A., et al., *Appl Surf Sci* (1994) **76/77**, 374.
- Deconihout, B., et al., *Ultramicroscopy* (1998) **73**, 253.
- Miller, M. K., *Atom Probe Tomography: Analysis at the Atomic Level*, Springer, New York, (2000).
- Bas, P., et al., *Appl Surf Sci* (1995) **87-88**, 298.
- Drachsel, W., et al. *J de Phys* (1989) **50-C8**, 541.
- Panayi, P., Atom probe, Patent WO 2006/134380, 2006.
- Nishikawa, O., et al., *J Vac Sci Technol B* (1995) **13**, 599.
- Kelly, T. F., et al., High mass resolution local-electrode atom probe, U S Patent 5440124, 1995.
- Kelly, T. F., et al., *Ultramicroscopy* (1996) **62**, 29.
- Kelly, T. F., et al. *Microsc Microanal* (2004) **10** (3), 373.
- Miller, M. K., et al., *Microsc Microanal* (2007) **13**(6), 428.
- Thompson, K., et al., *Ultramicroscopy* (2007) **107**, 131.
- Larson, D. J., et al., *J Phys: Conf Ser* (2011) 326, 012030.
- Miller, M. K., et al., *Materials Science Forum* (2010) **654-656**, 23.
- Miller, M. K., and Russell K. F., *J Nucl Mater* (2007) **371**, 145.
- Hellman, et al., *Microsc Microanal* (2000) **6**, 437.
- Blavette, D., et al., *Science* (1999) **286**, 2317.
- Kelly, T. F., and Miller M. K., *Rev Sci Instrum* (2007) **78**, 031101.
- Kelly, T. F., et al., *Annu Rev Mater Sci* (2007) **37**, 681.
- Cerezo, et al., *Microsc Microanal* (2007) **13**, 408.
- Seidman, D. N., *Annu Rev Mater Res* (2007) **37**, 127.
- Seidman, D. N., and Stiller, K., *MRS Bulletin*, (2009) 34 (10), 717; Marquis et al., *ibid*, 725; Larson et al., *ibid*, 732; Lauhon et al., *ibid*, 738; Kelly et al., *ibid*, 744.
- Gordon, L. M., and Joester, D., *Nature* (2011) **469**, 194.
- Miller, M. K., and Forbes, R. G., *Mater Character* (2009) **60**, 461.
- Moody, M. P., et al., *Microsc Microanal* (2011) **17**(2), 226.
- Stephenson, L. T., et al., *Microscopy Research & Technique*, **74** (2011) 799.
- Delendik, K., *Nucl Phys B – Proc Suppl* (2003) **125**, 394.
- Irwin, K.D., *Scientific American*, (Nov. 2006), 87.
- Estey, B. V., et al., *IEEE Trans Applied Superconductivity* (2009) **19**, 382.
- Casaburi, A., et al., *App Phys Lett* (2009) **94**, 212502.
- Zen, N., et al., *App Phys Lett* (2009) **95**, 172508.
- Kelly, T. F., *Microsc Microanal* (2011) **17**, 1.
- Blavette, D., et al. *Revue De Physique Appliquee* (1982) **17**, 435.
- Geiser, et al., *Microsc Microanal* (2009) **15**, 292.
- Gault, B., et al., *Ultramicroscopy* (2011) **111**, 448.
- Gault, B., et al., *Microsc Microanal* (2008) **14**, 296.
- Gault, B., et al., *J Appl Phys* (2009) **105**, 034913.
- Gault, B., et al., *Microsc Microanal* (2010) **16**, 99.
- Haley D., et al. *J Microscopy* (2011) **244**, 170.
- Miller, M. K., and Hetherington, M. G., *Surf Sci* (1991) **246**, 442.
- Miller, M. K., and Kelly, T. F., *Microsc Microanal* (2010) **16** (suppl. 2), 1856.
- Larson, D. J., et al., *Appl Surf Sci* (1993) 67, 473
- Suram, S. K., and Rajan, K., Informatics for Quantitative Analysis of Atom Probe Tomography Images. In - *Advanced Microscopy and Spectroscopy Techniques for Imaging Materials with High Spatial Resolution*, M. Ruehle, et al. (eds.) Mater. Res. Soc. Symp. Proc. Warrendale, PA, (2010) **1231E**, 1231-NN03-14.



# New materials for biological fuel cells

Major improvements in biological fuel cells over the last ten years have been the result of the development and application of new materials. These new materials include: nanomaterials, such as nanotubes and graphene, that improve the electron transfer between the biocatalyst and electrode surface; materials that provide improved stability and immobilization of biocatalysts; materials that increase the conductivity and surface area of the electrodes; and materials that aid facile mass transport. With a focus on enzymatic biological fuel cell technology, this brief review gives an overview of the latest developments in each of these material science areas and describes how this progress has improved the performance of biological fuel cells to yield a feasible technology.

Shelley D. Minteer<sup>a,\*</sup>, Plamen Atanassov<sup>b</sup>, Heather R. Luckarift<sup>c,d</sup>, and Glenn R. Johnson<sup>d</sup>

<sup>a</sup>Department of Chemistry and Materials Science and Engineering, University of Utah, 315 S 1400 E Rm 2020, Salt Lake City, UT 84112, USA

<sup>b</sup>Center for Emerging Energy Technologies, University of New Mexico, Albuquerque, NM 87131, USA

<sup>c</sup>Universal Technology Corporation, 1270 N. Fairfield Drive, Dayton, OH, 45432, USA

<sup>d</sup>Airbase Sciences, Air Force Research Laboratory, Tyndall Air Force Base, Florida 32403, USA

\*Email: [minteer@chem.utah.edu](mailto:minteer@chem.utah.edu)

Over the last decade, there has been renewed interest in biological fuel cells<sup>1-6</sup>; a subset of fuel cells, where the cathode and/or anode catalysts are biocatalysts. This biocatalyst could be a living cell (microbial fuel cells) or a subcellular biological component (enzymatic or mitochondrial biological fuel cells). The first biological fuel cells were microbial and employed microbes at the anode to catalyze the oxidation of fuel<sup>7</sup>. Over the last century, the technology (frequently referred to as bio-electrochemical systems in the research community) has expanded to include microbial cathodes, with applications including wastewater treatment, underwater power, and the production of electrofuels<sup>8-12</sup>. Enzymatic biological fuel cells were first introduced in the 1960s, where

oxidoreductase enzymes were used with mediators to catalyze the oxidation of amino acids, alcohol, and glucose at the anode of a fuel cell<sup>13</sup>. Continued development led to the use of enzymes at the cathode; where oxygen or peroxide is reduced to water in solution by an enzyme catalyst<sup>14,15</sup>, or where oxygen is reduced directly in an air-breathing biocathode<sup>16</sup>. The choice of subcellular biocatalyst has since expanded to include organelles; with mitochondria, for example, used at the anode of pyruvate/air biological fuel cells<sup>17</sup>.

Over the last decade, major improvements in biological fuel cells have actually been due to the incorporation of new materials, as well as the general move away from traditional H-cell designs toward engineered electrochemical cells. The specific improvements may be divided into

four types of materials that will be discussed herein: (1) nanomaterials that improve the electron transfer from the biocatalyst to the electrode surface, (2) materials that offer greater stability and immobilization of the biocatalysts, (3) materials that increase the conductivity and surface area of the electrodes, and (4) materials that offer superior facile mass transport.

## Nanomaterials that improve electron transfer

One key parameter of biological fuel cell performance is effective charge transfer; particularly in respect to enzymatic systems that rely on electron transfer between the electrode and the redox center of the enzyme. Electron transfer in biological fuel cells can occur via two general mechanisms: mediated electron transfer (MET) and direct electron transfer (DET).

MET occurs when the biocatalyst transfers electrons to a diffusible redox molecule or a redox polymer that in turn shuttles electrons between the biocatalyst and the electrode<sup>4</sup>. MET can be an efficient process when applied using reversible redox species with appropriate standard reduction potentials and defined concentrations of the mediator. There are drawbacks of MET, however, that must be rationalized in respect to fuel cell output and design. The primary limitation of diffusible mediators (more common in microbial biological fuel cells than enzymatic) is that most redox mediators are labile, imposing a limited lifespan that is further complicated by leaching during continuous operation of the cell. In addition, the half-cell potential is inherently limited by overpotential losses due to intermediate mediators, such as cofactors. The fuel cell design must also provide an absolute separation between half-cells in order to eliminate any crossover. Crossover is a common problem in all fuel cells, but can be circumvented by employing biological fuel cells that utilize selective, DET mechanisms by both anode and cathode catalysts.

DET processes eliminate many of the issues related to mediator use, since the electrons hop or tunnel directly between the biocatalyst and the electrode without any intervening *shuttle* molecules<sup>4</sup>. Designing bioelectrodes that carry out effective DET, however, is a challenge. In enzymatic fuel cells, for example, the enzyme must be arranged in such a way that its redox center is near the conductor electrode but not shielded by the enzyme structure, which acts as a non-conductive shell to limit electron transfer. Advances in nanomaterial synthesis and characterization are beginning to allow for specific control of the interaction; classed as the bio-nano interface. Defined protein assembly, combined with advances in bioelectrode architectures can significantly enhance DET processes and ultimately yield a realistic technology for small-scale biological fuel cells<sup>18</sup>.

Various conductive and functionalized nanomaterials have been examined as bioelectrode materials<sup>18,19</sup>. The criteria for developing architectures that are suited to microbial and/or enzymatic systems are inherently different. Herein, in the interest of clarity and brevity, discussion is related primarily to materials architectures that facilitate effective electron transfer with proteins, although some overlap does exist with microbial systems and pertinent examples will be highlighted

throughout. Development of microbial fuel cell electrodes typically requires a macroporous structure that is conducive to attachment of a large population of cells. Interestingly, microbes have been demonstrated to produce their own conductive nanowires (called pilli) that aid in the transfer of electrons via DET between the microbe and the electrode surface<sup>20</sup>. For enzymatic fuel cell electrodes, protein interaction and orientation at the nanoscale becomes more critical. As the aspect ratio of the nanomaterials approaches the molecular scale, the redox protein catalyst can establish a close association with the material, effectively decreasing the electron tunneling distance.

Primarily, the major enhancement in conductive interfaces for biomolecular electron transfer can be attributed to carbon-based materials; specifically: carbon black, carbon nanotubes (CNTs), and graphene.

### Carbon black

Carbon black nanomaterials (CBN) are widely used to fabricate enzyme-functionalized electrodes as they possess characteristics well suited to a biological interface, i.e., a high porosity and relatively high surface area, coupled with high conductivity. Protein molecules adsorb onto CBN principally via hydrophobic-hydrophobic interactions: the interaction can be close enough to allow DET if the redox enzymes are preferentially orientated<sup>21</sup>. As such, multiple examples of CBN-based bioelectrodes are found in the literature. Ma *et al.* immobilized hemoglobin on standard carbon black powders (reportedly 30 – 100 nm diameter) and subsequently demonstrated direct oxidation and reduction of the heme-iron using cyclic voltammetry<sup>22</sup>. Kano and his colleagues at Kyoto University combined another model redox protein, cuprous oxidase (CueO) with Ketjen black to form a bioelectrocatalyst that could use atmospheric oxygen as a terminal electron acceptor and provide a modest cathodic current<sup>23</sup>. The addition of Ketjen black allowed current densities of the biocathode to increase from 3 – 4 mA/cm<sup>2</sup> for CueO on highly ordered pyrolytic graphite electrodes (HOPGE) to ~20 mA/cm<sup>2</sup> for Ketjen black incorporated electrodes. Similarly, increases in power density of 5 to 10-fold have been observed when Vulcan® XC-72 CBN are incorporated into PQQ-dependent alcohol dehydrogenase and PQQ-dependent glucose dehydrogenase-based biological fuel cells<sup>18</sup>.

CBN are readily modified to create composites; emulsions of Teflon® and CBN, for example, are amenable to attachment on metallic, glassy carbon or other conventional electrode surfaces<sup>24</sup>. The combination of CBN and Teflon polymer provides a material matrix with the appropriate balance of hydrophobic-hydrophilic properties to yield a functional “electrolyte-carbon-air” tri-phase interface needed for gas diffusion electrodes (GDE)<sup>25</sup>. The CBN architecture has been demonstrated for the assembly of such GDE and recent advances have further improved upon the Ketjen-black based architectures<sup>16,26,27</sup>.

### Carbon nanotubes

The introduction of carbon nanotubes (CNTs) provided a novel tool for combining the bio-nano interface, due to inherent properties and

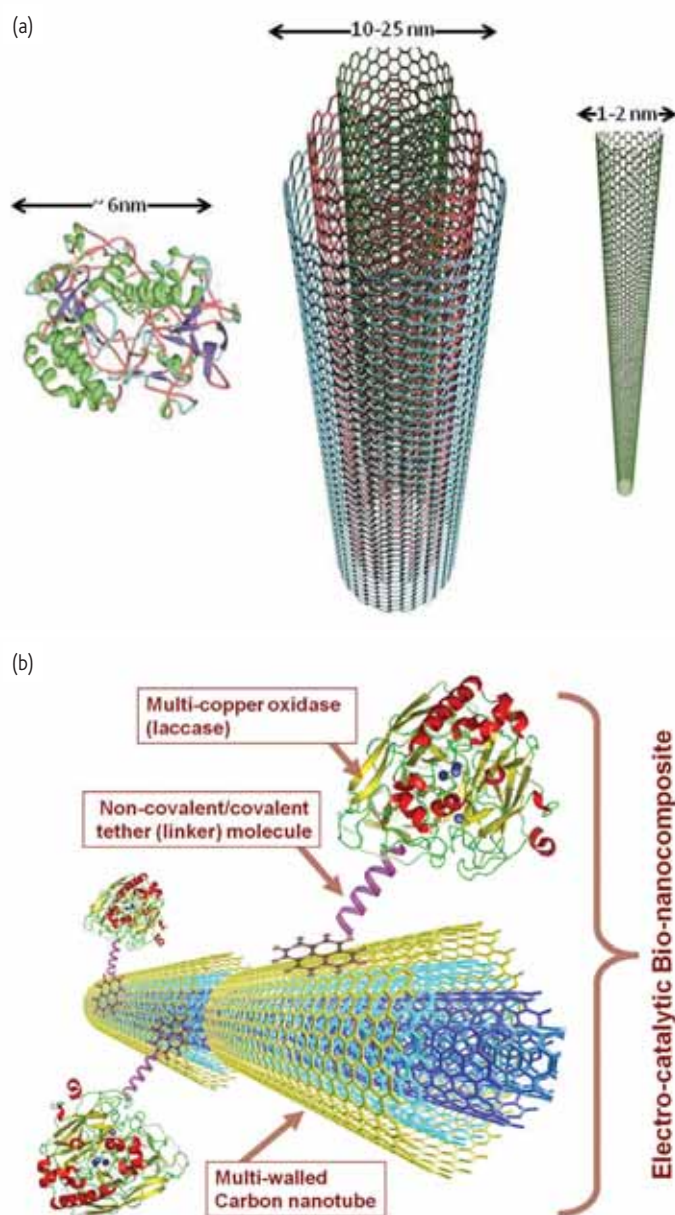


Fig. 1 (a) Relative dimensions of a glucose oxidase molecule and typical multiwall and single wall carbon nanotubes. (b) Schematic of the design of a bionanocomposite utilizing the phenol oxidase and multiwalled carbon nanotube material.

conductivity that provide a niche architecture well suited to fuel cells, sensors, and bio-electronics<sup>28-30</sup>. Both multi-wall carbon nanotubes (MWNTs) and single-wall carbon nanotubes (SWNTs), for example, have dimensions that are uniquely amenable to close physical, and then direct electronic interactions with redox proteins. A simple two-dimensional depiction of the materials and protein molecules gives a sense of scale and the potential interactions between redox enzymes and CNTs (Fig. 1). Further chemical functionalization of CNTs (e.g., amine-, carboxyl-, hydroxyl-groups) can be attained that maintain conductivity and provide additional sites for specific redox protein attachment. The typical dimensions of MWNTs would likely limit deep penetration

toward the redox-center of the enzyme, instead the MWNT curvature is considered to be essentially “flat” from the perspective of the enzyme as a surface for attachment. Accordingly, there is an opportunity to take advantage of multiple surface moieties of a protein in order to link with the CNTs at specific and strategic tethering points. The options include both non-covalent (van der Waals, hydrophobic-hydrophobic, and ionic) and covalent interactions between unmodified and modified nanotubes<sup>30</sup>. By comparison, the dimensions of SWNTs may allow the conductive surface of the nanotube to physically access redox active sites, further decreasing the electron tunneling distance between the catalyst and electrode significantly.

Examples of CNT- and CNT-hybrid materials for bioelectrodes abound in the recent literature including materials architectures that are specifically advantageous for microbial fuel cells<sup>18,31</sup>. Many researchers, for example, have utilized CNTs to increase the surface area of electrodes, to improve the conductivity of porous scaffolds for biofilm growth, or to increase direct bioelectrocatalysis. For enzyme architectures, in the simplest case, a redox protein may contact a CNT surface by physisorption, with the protein adhering to the hydrophobic CNT surface, largely via van der Waals forces. Non-covalent interactions are somewhat labile, but have been used for establishing DET with a variety of redox enzymes<sup>32-34</sup>. The most common method of functionalizing CNTs is chemical oxidation to yield carboxylic acid groups at defect points on the CNT surface. The carboxyl groups can subsequently be activated by carbodiimide chemistry, which forms an unstable ester that will then react with accessible amino groups on the protein surface and form covalent amide bonds. The covalent link stabilizes the interactions and minimizes the distance between the protein and CNT surface, promoting electronic connectivity and DET. An example of this methodology is reported by Vaze *et al.*; with SWNTs-based electrodes and glucose oxidase (GOx) as the bioelectrocatalyst, the half-cell potential approached the theoretical redox potential for FAD/FADH<sub>2</sub> (−0.45V vs SCE) and current densities correlated to glucose concentration<sup>34</sup>. The results confirmed DET between the protein and electrode surface, and catalytic activity of the enzyme was retained<sup>35</sup>. There are caveats to this approach however, as the oxidation creates defects in the CNTs that decreases the conductivity of the material. Additionally, the short covalent link can result in steric constraints on the protein structure that reduce its catalytic activity<sup>36</sup>. Further experimental materials have combined CNTs with metal colloids and metal nanoparticles in an attempt to take advantage of the properties of each material for superior electrocatalysis<sup>37,38</sup>.

## Graphene

The emergence of graphene in research and its transition into a technologically viable material has provided a new dimension for bio-nanomaterials. Although it still remains to be determined if it is a practical material for constructing electrodes, initial studies demonstrate the potential for a less-explored, but electrochemically compelling material. Like CNTs,

graphene is amenable to covalent and non-covalent functionalization of the surface. The functionalization, if done correctly, does not appear to change the ballistic conductivity of the pristine graphene<sup>39</sup>.

As such, the coupling of biocatalysts with graphene is beginning to receive interest in the literature. In one report, GOx was contacted with a graphene-glassy carbon electrode through simple physisorption and demonstrated catalytic activity and a characteristic DET response attributed to the flavin adenosine nucleotide (FAD) cofactor at  $-454$  mV vs SCE<sup>40</sup>. The biopolymer chitosan, aids dispersion of various nanomaterials, including graphene, easing the formation of thin film electrodes. Again the model bioelectrocatalyst, GOx, was used to demonstrate the utility of the hybrid nanocomposite. GOx adsorbed to a chitosan/graphene thin film showed DET characteristics and a sensitive amperometric response to glucose concentrations ( $37.93 \mu\text{A mM}^{-1}\text{cm}^{-2}$  versus  $7.36 \mu\text{A mM}^{-1}\text{cm}^{-2}$  for chitosan/MWNT). Using a chitosan architecture, the detection sensitivity increased two-fold compared to immobilization of GOx on graphene alone<sup>41</sup>. In other work, the same approach was demonstrated to combine cytochrome C, chitosan, and graphene on a glassy carbon electrode and DET was observed for the biocatalytic reduction of nitric oxide<sup>42</sup>. Further credence toward the utility of graphene-based bioelectrodes was provided by a side-by-side comparison against SWNT-based electrodes using GOx as the anode catalyst and bilirubin oxidase as the oxygen reduction catalyst in the cathode. The current density of the assembled graphene-based fuel cell was double that observed for a SWNT architecture; moreover the power density with graphene was 3x greater than for a comparable SWNT fuel cell<sup>43</sup>.

In parallel studies, graphene has recently found application in the development of microbial fuel cells. Li and co-workers, for example, have utilized the bacterium *Shewanella sp.* to reduce graphene for direct electron transfer<sup>44</sup>.

## Materials for stabilizing and immobilizing biocatalysts

As described above, the crux of effectively utilizing biomolecules in biological fuel cells is the effective orientation and interaction between an enzyme and a conductive transducer surface. Enzymes *ex situ* typically exhibit poor longevity, particularly when the local physiological

environment pushes the optimal activity range of the enzyme. Particularly in bio-electronics applications, poor biocatalyst stability results in low power density and short lifetimes, because enzymes dissolved in solution at room temperature typically only have activity for a few hours and catalytic material is needed at the surface of the electrode to transport electrons efficiently<sup>19</sup>. Stabilization of the enzyme integrity is therefore essential to the efficiency and is typically achieved by various means of enzyme immobilization<sup>45</sup>. Immobilization serves to preferentially anchor the biomolecules in a manner that retains the native tertiary structure. Enzyme stabilization can also provide increased selectivity and may improve mass transfer kinetics. Immobilization strategies typically involve physical adsorption (primarily by electrostatic binding), entrapment in conducting polymer matrices, or covalent attachment to functionalized polymers<sup>46</sup>. Physical adsorption is attractive in its simplicity and although electrocatalytic activity can be retained, the power density is often low due to poor protein loading and leaching is a concern that limits lifetime. In contrast, covalent immobilization strategies provide superior electrocatalytic characteristics, but can sometimes hinder protein conformation<sup>47</sup>. In addition, the functional groups on the enzyme that are used for tethering should not be essential to catalysis or enzyme inactivation losses will occur.

Alternatively, methods of enzyme encapsulation can provide a means to stabilize proteins in a 'protective' environment by either trapping the protein, wiring the protein to the polymer backbone, or by specifically depositing enzymes within micellar pockets<sup>48-50</sup> (Fig. 2). Enzymes immobilized within the pockets of hydrophobically modified micellar polymers such as Nafion® and chitosan, for example, have been shown to effectively stabilize enzymes at electrode surfaces and promote operation lifetimes of more than two years<sup>48</sup>.

A wide variety of redox catalysts can be stabilized by encapsulation during silica sol-gel formation<sup>51-53</sup>. Conductivity of the silica matrix can be achieved by co-immobilization of a conductive material, such as CNTs. The cationic protein, lysozyme for example, catalyzes and templates the formation of silica directly onto a conductive carbon paper electrode. Inclusion of CNTs and GOx into the reaction mixture results in a catalytic composite that becomes encapsulated as the silica forms<sup>54</sup>. The CNTs can act as nanowires within the silica matrix, essentially providing an electrical connection between the enzyme and the

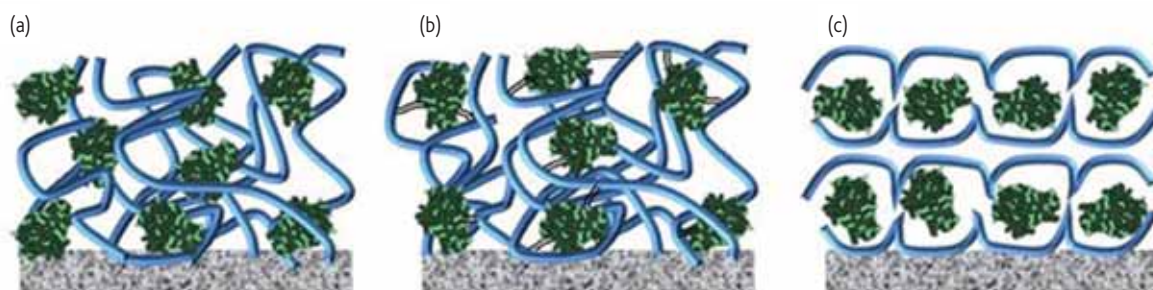


Fig. 2 Enzymes immobilized on an electrode surface via (a) physical adsorption to a polymer, (b) covalent attachment to a polymer (as shown by the black and white tethers), or (c) encapsulation in polymer micelles.

electrode and providing additional surface area for adsorption of active GOx as indicated by an increase in the electrochemically active surface area of a commercially available screen printed electrode to 3.7 cm<sup>2</sup>. Similarly, enzymes can catalyze the reduction of metal salts to form discrete metal structures, such as gold nanoparticles. GOx, for example, will catalyze the reduction of gold (III) chloride with size-controllable formation of gold particles, into which the protein becomes entrained as the metal structure forms. The resulting GOx/gold composite retains the catalytic activity of the protein and DET is observed between the FAD cofactor and the electrode as shown voltammetrically via a peak at -0.44V vs Ag|AgCl; as such, a catalytic current is observed in response to glucose, which increases non-linearly from 5 mM to 25 mM glucose<sup>55</sup>.

Direct interaction between the enzyme and electrode is a particular challenge for enzymes such as GOx where the cofactor is buried deep within the protein structure. This limitation can be overcome by anchoring the cofactor, FAD, directly to the electrode surface. The apoenzyme (enzyme without cofactor) is subsequently added and reforms around the anchored FAD; ensuring that the enzyme is in close communication with the electrode. The cofactor anchor is typically achieved by linking to gold nanoparticles or CNTs that serve as an electron bridge<sup>56,57</sup>. FAD, for example, can be linked to SWNT and used to position the apoenzyme of GOx; whereby the length of the CNTs directly influences the resulting electrical connectivity<sup>58</sup>. Similarly, Ivnitski *et al.*, demonstrated the anchoring of GOx to CNT and observed DET between the active site of the enzyme and MWNT that were grown directly on a Toray<sup>®</sup> carbon electrode<sup>59</sup>.

The introduction of CNT as a conductive material has provided a means to develop new conductive architectures, and a range of buckypaper (CNT paper), buckygel (CNT gels), and carbon nanofiber electrodes have since been reported that demonstrate a significant enhancement in electron transfer characteristics for both anodic and cathodic catalysts<sup>60-63</sup>. Cathodic oxygen reduction catalysts, for example can be immobilized to buckypaper, by simple physical adsorption<sup>64</sup>, but preferential orientation is encouraged by using a bifunctional cross linking agent (1-pyrenebutanoic acid, succinimidyl ester; PBSE) that interacts with CNT via  $\pi$ - $\pi$  stacking<sup>62</sup>. The tethering of laccase via PBSE results in stable cathodic currents and potential losses of < 0.1 V. Buckygels, in comparison incorporate ionic liquids and CNT in a composite material, into which NAD(P)H electrocatalysts (such as methylene green) can be added to help regenerate the enzyme cofactor NAD(P)<sup>+</sup> at moderate overpotentials<sup>60</sup>.

Arguably one of the most significant contributions to improvements in biosensors and biological fuel cell development was the introduction of redox hydrogels, typically based on osmium or ruthenium complexes, into which enzymes could be effectively co-immobilized. This technical direction helped demonstrate the utility of biological fuel cells as implantable devices and with implications in diabetes management<sup>65,66</sup>. Enzyme catalysts are typically covalently bound to the hydrogel, and initial issues of long-term stability have been overcome by further

anchoring the hydrogel to electrodes using surface carboxylates or amines<sup>67,68</sup>. Osmium-based redox hydrogels have been used for both anodic and cathodic electrodes. Although hydrogels are typically considered fragile, lifetimes greater than 14 days have been reported for enzymes in hydrogel matrices. Redox hydrogels have similarly been employed for microbial bioelectrocatalysis<sup>69</sup>. These types of combined immobilization and mediation strategies, however, have been much less common in microbial fuel cells due to the ability of the microbes to self-immobilize and grow nanowires/pili to communicate directly with the electrode<sup>20</sup>.

## Materials for increased conductivity and surface area of electrodes

In the field of biological fuel cells, there are two types of conductivity that are important to performance, conductivity of the electrode and electrode components, and ionic conductivity between the electrodes. Ionic conductivity between the electrodes is typically separated into two types: ionic conductivity of the electrolyte solutions and ionic conductivity of the polymer electrolyte membrane separating the catholyte from the anolyte. Low conductivity results in large ohmic losses in biological fuel cell performance, so improving the conductivity of the overall system is important. Early in the development of traditional metal-catalyzed fuel cells, researchers designed fuel cells specifically to minimize the distance between electrodes. Many of these strategies have also been applied to biological fuel cells over the last decade, as the original H-cell setup has transitioned toward membrane-free strategies and membrane electrode assembly (MEA)-style biological fuel cells<sup>70</sup>. Fig. 3 shows the transition from H-cells to membrane-free electrochemical cells to MEA-style fuel cells. Interestingly, MEA-style fuel cells permit the incorporation of a bipolar plate design, which has also been demonstrated for microbial fuel cells<sup>71</sup>. H-cells typically have a minimum of distance of 1 cm between the anode and the cathode (although many cell designs have distances of greater than 10 cm) and typically the majority of that distance will be filled with low conductivity electrolyte solution (such as a biological buffer). The membrane-free strategy allows for closer electrode separation (typically less than 5 mm), and the separation is filled with a low conductivity electrolyte solution<sup>72</sup>. In comparison, MEA-style fuel cell designs typically have less than a 1 mm separation between the cathode and anode and the whole gap is a polymer electrolyte membrane<sup>73,74</sup>.

From a materials perspective, researchers have focused on improving ionic conductivity by studying different polymer electrolyte membranes. Most polymer electrolyte membranes used in biological fuel cells are Nafion<sup>®</sup>, but most biological fuel cells operate at neutral pH, so a proton exchange membrane is non-ideal, because it has a higher resistance in potassium or sodium buffers at near neutral pH, than it would in the normal acidic environment of traditional fuel cells. For this reason, recent studies have addressed the development of alternative cation exchange membranes (i.e., Ultrex)<sup>70</sup> and alkaline exchange membranes<sup>75</sup>. They

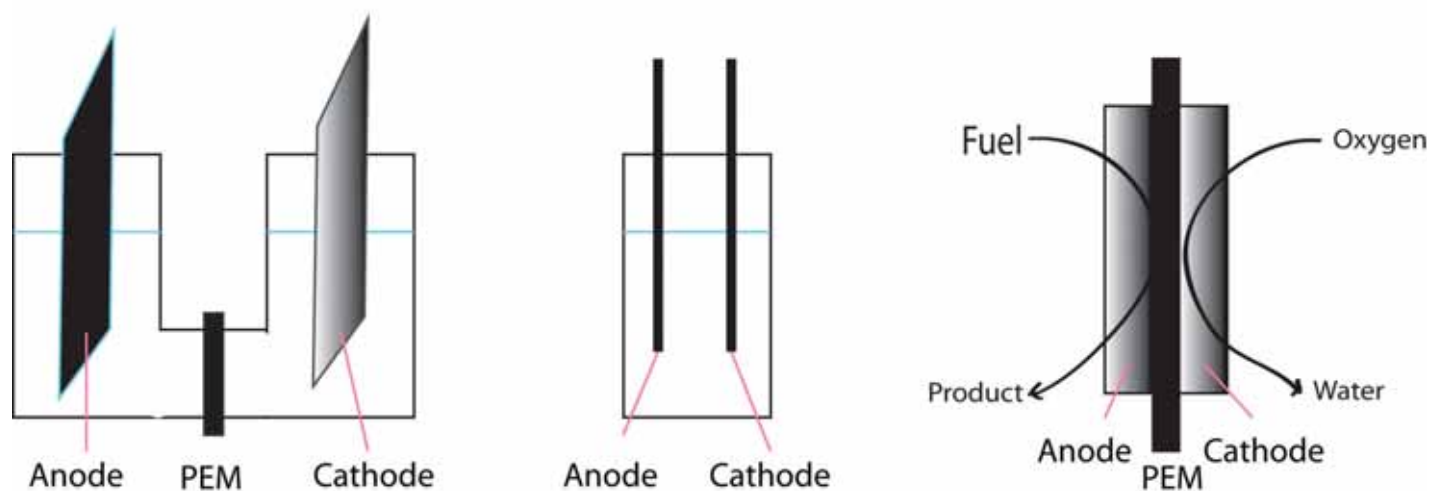


Fig. 3 Schematics showing the transition from the original biological fuel cell design (left figure, often called an H-cell) where the two electrodes are submerged in two different solutions that are separated by a polymer electrolyte membrane (PEM), to the membrane-less biological fuel cell (center figure) where the two electrodes are submerged in the same solution and there is no separator/PEM, to the membrane electrode assembly (MEA) design (right figure) where the anode and cathode are in contact with the PEM.

have also studied bipolar membranes for microbial fuel cells<sup>76</sup>. As of yet, a polymer electrolyte membrane with high conductivity at near neutral pH or that can handle pH differences at the anode and cathode has yet to be achieved. The lack of polymer electrolyte membrane with high ionic conductivity at neutral pH and lack of a polymer electrolyte membrane that can effectively handle pH gradients between the anode and the cathode are major issues that will need to be addressed over the next period of materials research in biological fuel cells.

There is no easy way to compare differences in conductivity between electrochemical cells, in the absence of a standardized fuel cell design. The enzymatic biological fuel cell field typically does not determine ohmic resistances of cells, whereas this parameter is frequently reported for microbial fuel cell systems. There is, however, no standard practice for comparable reporting of this type of performance information. For instance, some reports document ohmic resistance per cubic meter of the bioelectrochemical system and other report ohmic resistance per square meter. In addition, resistance will be a function of the thickness as well as the properties of each membrane. Sleutels *et al.* began to address this bottleneck by directly comparing the differences between cation and anion exchange membranes. An internal resistance of 192 m $\Omega$ /m<sup>2</sup> was reported for a biological fuel cell fabricated with an anion exchange membrane, versus 435 m $\Omega$ /m<sup>2</sup> for a comparable cation exchange membrane-based cell<sup>77</sup>.

The second issue associated with conductivity is the electrode or current collector conductivity, which is closely related to the development of high surface area materials. Since the volumetric catalytic activity of proteins, organelles, and living cells is low, it is important to have high surface area materials to load larger quantities of biocatalyst. The goal has been to maintain conductivity while increasing surface area. These high surface area materials focus on having a high surface area to volume

or mass ratio. Most early biological fuel cell designs were glassy carbon, graphite, or reticulated vitreous carbon (RVC). The transition to higher surface area materials has included the incorporation of nanomaterials (discussed above) as well as the use of mesoporous carbon<sup>19</sup>, carbon foams, buckypaper, and buckygels.

### Hierarchical materials for improved mass transport

Most biological fuel cells currently reported in the literature are actually "bio-batteries"; they are either catalytic bio-electrodes immersed in a solution of the fuel or are meant to incorporate the fuel as a part of their design and as a result there is no continuous supply of fuel to the reactive layer. Lately, true "biological fuel cells" have been starting to emerge where the need to improve mass transport to and from the biocatalysts has become necessary<sup>31,78,79</sup>. Naturally, the design of materials for biological fuel cell applications followed the need to match the transport properties at the corresponding scale. At a macro-scale, the fluid flow needs to be accommodated and this results in design solutions with large void volumes (preferably more than 0.6), pore sizes in the range of 10 – 100  $\mu$ m (and even up to 1 mm) and low tortuosity of the porous media. This scale of design is aimed to accommodate convective flow with rates below 1 cm<sup>3</sup>/s. Such materials are preferred to have high electrical conductivity and are usually expected to provide the mechanical stability (rigidity) that is associated with building them into the biological fuel cell design as a structural component. Among the most widely used materials are different types of carbon (graphite) felts and carbon papers (Toray® paper being among the traditional sources). RVC and metal foams have also been introduced as a material of choice, particularly where 3D, bulk designs (such as cylindrical flow-through electrodes operating in a plug-flow regime) are being pursued<sup>31,78,79</sup>.

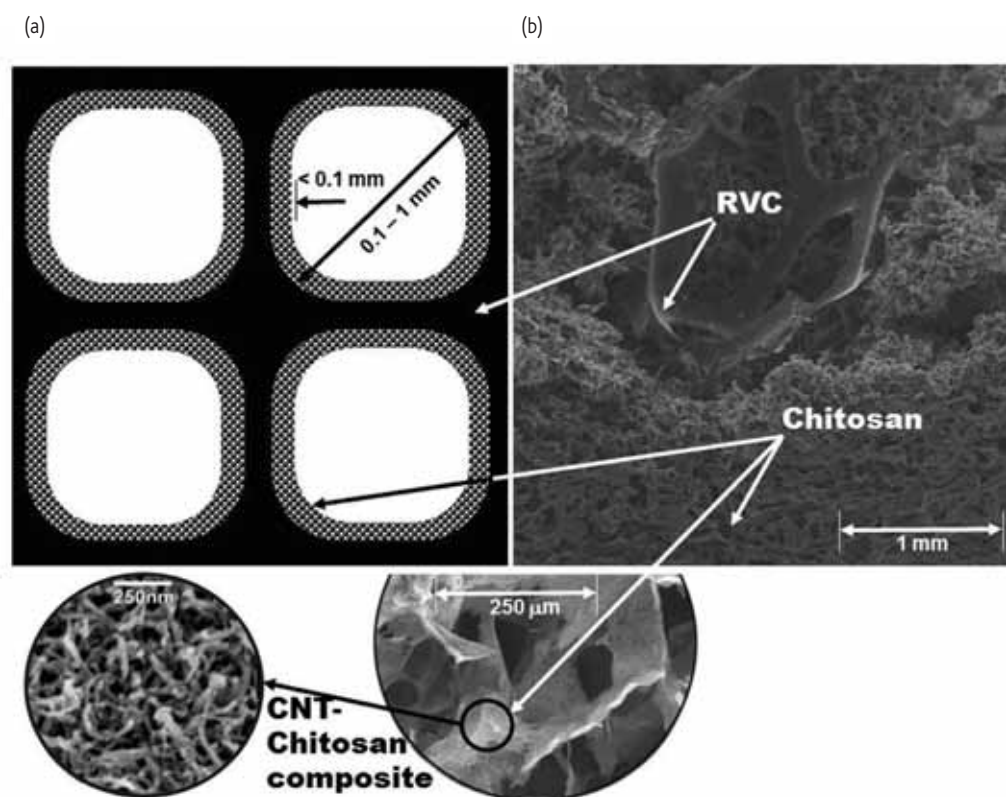


Fig 4 Schematic of a flow-through electrode material for a biological fuel cell that contains macropores in the reticulated vitreous carbon (RVC), micropores due to freeze drying of chitosan, and nanopores from the chitosan/CNT composite.

These macro-porous materials, however, cannot provide enough surface area for the immobilization of biocatalysts. Their intrinsic surface area is usually below  $10\text{ m}^2/\text{g}$  (and often less than  $1\text{ m}^2/\text{g}$ ). This fact, combined with the practical enhancement of biocatalysts interactions with nano-materials (described above), calls for the integration of such materials with micro-porous or nano-scale, high-surface area materials. One example of such integration is the direct grafting of nano-materials onto open-pore structured substrates, such as CNT grown on Toray® paper<sup>80, 54</sup>. This macro-nano composite structure allows both substantial enzyme loading and promotes the desired nano-material/biocatalyst interactions. In a general case, however, such integration is difficult and much research has been focused on building hierarchically structured materials where all three levels of scale will be present: macro-scale porosity responsible for convective flow and fuel delivery; meso-scale architecture designed for the integration of materials properties; and the addition of nano-materials such as CNTs or gold nanoparticles, in the case of GDE<sup>16</sup>, to smooth the progress of gaseous reactants (oxygen from ambient air) towards the reaction zone and micro-porous components<sup>54,55,81</sup>. The mesoporous component of such a composite matrix is usually responsible for interconnectivity and thus ensures the electrical conductivity of the matrix<sup>82,83</sup>. Fig. 4 represents both a schematic representation of an idealized material that embodies all three levels of porosity/structure along with an SEM

microphotograph of an example of one such composite bioelectrode. In this case RVC is used as a conductive, macro-porous matrix, on the wall of its "foam-like" structure a conductive CNT/chitosan polymer composite layer is being formed that has its own porosity derived through a freeze-drying process and optimized for CNT content such as to demonstrate substantial conductivity and expose the "surface" of the CNT for immobilization of the biocatalysts. Such hierarchically-structured electrodes have been shown to be advantageous when used as enzyme anodes with immobilized oxidases or dehydrogenases or with microorganisms colonizing their inner space in microbial fuel cell anodes.

It is important to note that there are a variety of important factors to consider when designing a porous electrode for flow, including the hydrophobicity/hydrophilicity of the high surface area material to ensure wetting and avoid dead zones as well as the diffusional transport properties of the material. Paying close attention to these factors will result in improved biological fuel cell performance.

## Conclusions

This review illustrates the strides in materials engineering that have contributed significant advancements in enzymatic and microbial biological fuel cell performance in the last decade. Further innovation is still needed, however, to fully harness the full potential of biological

fuel cells. These materials engineering advances have included the incorporation of high surface area materials to improve the loading of biocatalysts and to facilitate DET, materials for improved enzyme immobilization and stabilization, and the design of hierarchical material structures for advanced electrode design. Research is needed in the design of materials to improve the bio-nano interface to be more amenable to biocatalysts, as well as the production of structures that aid DET, so that high current density electrodes with long term stability can be

realized. Secondly, a paradigm shift in the development of ion exchange membrane materials is needed to create membrane materials that are specifically designed for biological fuel cells rather than for typically highly acidic or highly alkaline environments of traditional fuel cells. 

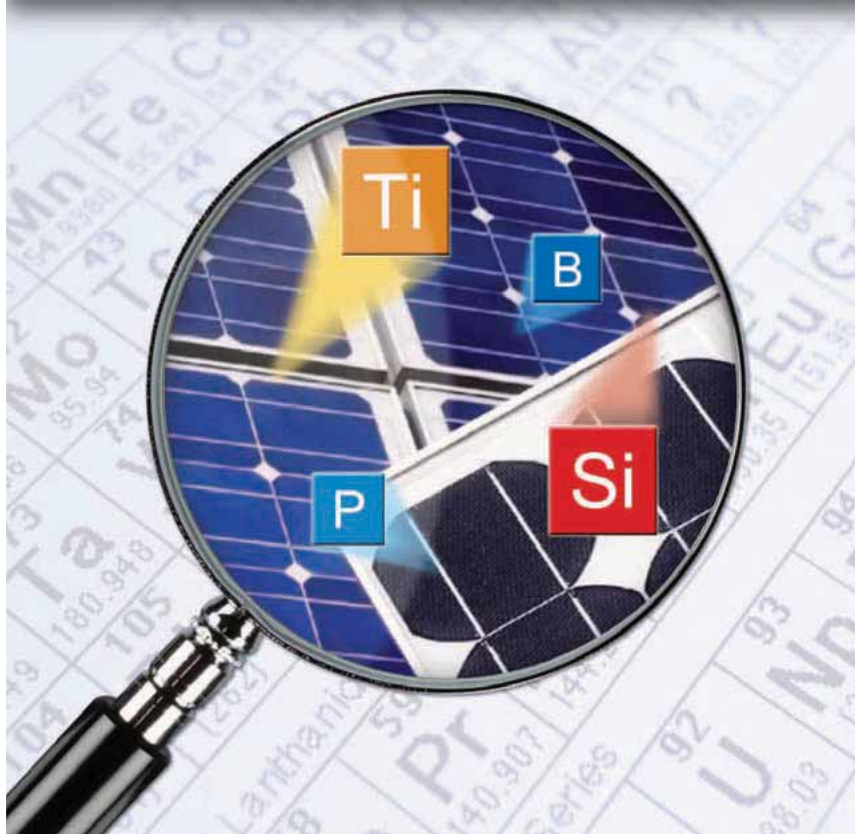
## Acknowledgements

The authors would like to thank the Air Force Office of Scientific Research and the Air Force Research Laboratory for funding.

## REFERENCES

- Shukla, A. K., et al., *Curr Sci* (2004) **87**(4), 455.
- Calebrese Barton, S., et al., *Chem Rev* (2004) **104**, 4867.
- Bullen, R. A., et al., *Biosens Bioelectron* (2006) **21**, 2015.
- Cooney, M. J., et al., *Energy Environ Sci* (2008) **1**, 320.
- Heller, A., *Phys Chem Chem Phys* (2004) **6**(2), 209.
- Willner, I., et al., *Fuel Cells* (2009) **9**(1), 7.
- Potter, M. C., *Proc Royal Soc London* (1912) **84**, 260.
- Balat, M., *Energy Sources, A: Recovery, Utilization, Environ Effects* (2010) **32**, 26.
- Du, Z., et al., *Biotechnol Adv* (2007) **25**, 464.
- Logan, B. E., *Appl Microbiol Biotechnol* (2010) **85**, 1665.
- Nevin, K. P., et al., *mBIO* (2010) **1**(2) 1.
- Rabaey, K., et al., *Bio Tech International* (2010) **22**, 6.
- Yahiro, A. T., et al., *Biochim Biophys Acta* (1964) **88**(2), 375.
- Brunel, L., et al., *Electrochem Comm* (2007) **9**, 331.
- Pizzariello, A., et al., *Bioelectrochemistry* (2002) **56**(1-2), 99.
- Gupta, G., et al., *Electrochem Comm* (2011) **13**(3), 247.
- Arechederra, R. L., et al., *Electrochim Acta* (2008) **53**, 6698.
- Arechederra, R. L., et al., in *Nanomaterials for Energy Storage Applications, Vol 1* ed.; H. S. Nalwa: American Scientific Publishers, Stevenson Ranch, CA, **2009**, pp. 287.
- Kim, J., et al., *Biotechnol Adv* (2006) **24**(3), 296.
- Gorby, Y. A., et al., *Proc Natl Acad Sci* (2006) **103**(30), 11358.
- Tominaga, M., et al., *Chem Lett* (2006) **35**(10), 1174.
- Ma, G.-X., et al., *Bioelectrochemistry* (2007) **71**(2), 180.
- Kontani, R., et al., *Bioelectrochemistry* (2009) **76**(1-2), 10.
- Bidault, F., et al., *J Power Sources* (2009) **187**(1), 39.
- Shteinberg, G. V., et al., *J Power Sources* (1982) **8**(1), 17.
- Gupta, G., et al., *Electrochim Acta* (2011) **56**(28), 10767.
- Shleev, S., et al., *Fuel Cells* (2010) **10**(4), 726.
- Gong, K., et al., *Anal Sci* (2005) **21**(12), 1383.
- Hu, S., et al., *J Sensors* (2009) **2009**, 187615
- Jia, H., et al., *Biomol Catalysis*, (2008) 18, ACS symposium series, 986, pp. 273
- Higgins, S. R., et al., *Enzy Micro Technol* (2011) **48**, 458.
- Luong, J. H. T., et al., *Electroanalysis* (2005) **17**(1), 47.
- Zebda, A., et al., *Nature Commun* (2011) **2**. Doi: 10.1038/ncomms1365
- Zhao, Y.-D., et al., *Sensors Actuators B: Chemical* (2002) **87**(1), 168.
- Vaze, A., et al., *Electrochem Comm* (2009) **11**(10), 2004.
- Vashist, S. K., et al., *Biotechnol Adv* (2011) **29**(2), 169.
- Luo, X., et al., *Electroanalysis* (2006) **18**(11), 1131.
- Wang, Y., et al., *J Mol Catalysis B: Enzymatic* (2011) **71**(3-4), 146.
- Malig, J., et al., *Interface* (2011) **20**(1), 53.
- Wu, P., et al., *Electrochim Acta* (2010) **55**(28), 8606.
- Kang, X., et al., *Biosens Bioelectron* (2009) **25**(4), 901.
- Wu, J. F., et al., *Electrochem Comm* (2010) **12**(1), 175.
- Liu, C., et al., *Biosens Bioelectron* (2010) **25**(7), 1829.
- Wang, G., et al., *Nano Research* (2011) **4**(6), 563.
- Osman, M. H., et al., *Biosens Bioelectron* (2011) **26**, 3087.
- Moehlenbrock, M. J., et al., in *Enzyme stabilization and immobilization: Methods and protocols, Vol 679* (Ed.: S. D. Minter) Humana Press, **2011**.
- Noll, T., et al., *Chem Soc Rev* (2011) **40**, 3564.
- Besic, S., et al., *Methods in molecular biology (Clifton, NJ)* (2011) **679**, 113.
- Kim, H., et al., *Biosens Bioelectron* (2011) **26**, 3908.
- Tan, Y., et al., *Biosens Bioelectron* (2009) **24**, 2225.
- Lim, J., et al., *Phys Chem Chem Phys* (2007) **9**(15) 1809.
- Sarma, A. K., et al., *Biosens Bioelectron* (2009) **24**(8), 2313.
- Wang, J., *Analytica Chimica Acta* (1999) **399**(1-2), 21.
- Ivnitski, D., et al., *Small* (2008) **4**(3), 357.
- Luckarift, H. R., et al., *Electroanalysis* (2010) **22**(7-8), 784.
- Willner, B., et al., *Curr Opin Biotechnol* (2006) **17**(6), 589.
- Xiao, Y., et al., *Science* (2003) **299**(5614), 1877.
- Patolsky, F., et al., *Angewandte Chemie* (2004) **43**(16), 2113.
- Ivnitski, D., et al., *Electrochem Comm* (2006) **8**(8), 1204.
- Yu, P., et al., *Anal Chem*, (2011) **83**(14), 5715.
- Hussein, L., et al., *Electrochim Acta* (2011)doi: 10.1016/j.electacta.2011.06.067.
- Ramasamy, R. P., et al., *Chem Comm* (2010) **46**(33), 6045.
- Kim, B. C., et al., *Biosens Bioelectron* (2011) **26**, 1980.
- Hussein, L., et al., *Biosens Bioelectron* (2011) **26**, 4133.
- Heller, A., et al., *Acc Chem res*(2011) **43**(7), 963.
- Heller, A., *Anal Bioanal Chem* (2006) **385**(3), 469.
- Boland, S., et al., *Electrochim Acta* (2009) **54**, 1986.
- Boland, S., et al., *J Electroanal Chem* (2009) **626**, 111.
- Timur, S., et al., *Bioelectrochemistry* (2007) **71**, 38.
- Logan, B. E., et al., *Environ Sci Technol* (2006) **40**, 5181.
- Shin, S. H., *Bull Korean Chem Soc* (2006) **27**, 81.
- Mano, N., et al., *ChemBioChem* (2004) **5**(12), 1703.
- Bhatnagar, D., et al., *Phys Chem Chem Phys* (2011) **13**, 86.
- Hudak, N. S., et al., *J Electrochem Soc* (2005) **152**, A876.
- Kim, J. R., et al., *Environ Sci Technol* (2007) **41**, 1004.
- Heijne, a. T., et al., *Environ Sci Technol* (2006) **40**, 5200.
- Sleutels, T. H. J. A., et al., *Int J Hydrogen Energy* (2009) **34**, 3612.
- Rincon, R. A., et al., *Electrochim Acta* (2011) **56**, 2503.
- Rincon, R. A., et al., *Biosens Bioelectron* (2011) **27**, 132.
- Calabrese Barton, S., et al., *Electrochem Solid-State Lett* (2007) **10**, B96.
- Lau, C., et al., *Langmuir* (2008) **24**(13), 7004.
- Lee, J., et al., *Adv Mater* (2006) **18**, 2073.
- Wen, Z., et al., *J Mater Chem* (2009) **19**, 8707.

**Do you really know the purity of your materials?**



**Take Control of Contaminants**

**Analytical Services Worldwide**

**Composition**

**Trace Elements**

**Thermal Properties**

**Full Range of Analytical Services**

**Innovative Analytical Solutions**

**You Request - We deliver!**

**315-431-9900**

**materialstoday@eaglabs.com**

**www.eaglabs.com**



# materialstoday

**The latest materials science news  
at your fingertips...**

*Download the new iPad app to read the latest news, views and opinions from around the World brought to you by **Materials Today**.*

*Now available free of charge from the App Store.*



iPad is a trademark of Apple Inc.

# An inorganic puzzle



## Aerogel gives rise to nano-boomerangs with a high return

Sergey V. Balakhonov\*, Eugene A. Goodilin, Anton I. Gavrillov, Daria Y. Gavrillova, and Bulat R. Churagulov

\*E-mail: [balakhonov@inorg.chem.msu.ru](mailto:balakhonov@inorg.chem.msu.ru)

The continued evolution of various high-tech gadgets dictates that it is necessary to reduce the size of chemical power sources whilst retaining their extraordinary electrochemical performance characteristics, such as their discharge capacity and power density. Cathode materials must intercalate and deintercalate lithium ions thousands of times and maintain high electronic conductivity between tiny particles of material undergoing huge stress relaxation. Obviously, a high surface area favors fast ion exchange between the cathode and the surrounding electrolyte, and a low particle size or thickness of the cathode material preserves the stability of the crystal structure.

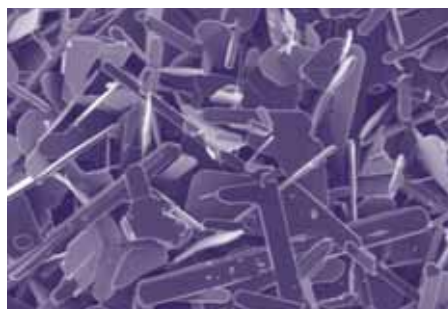
Traditional 2D cells aren't able to support the energy and size requirements of microdevices such as "smart dust" or intelligent medical implants<sup>1</sup>. Therefore, researchers must look towards the third dimension, and have already proposed several types of 3D cell. Most of them consist of arrays of nanorods, interconnected networks, or nanoparticles with unusual, complex morphologies. Other examples of 3D cells consist of porous materials, providing better electrochemical performance because of the faster and "deeper" lithium intercalation<sup>2</sup>.

The best porous materials for this type of application can be discovered amongst the family of aerogels based on vanadium oxide. It is a commonly held notion that aerogels are composites of "being and nothingness"<sup>1,3</sup>. Aerogels are mesoporous materials with a nano-scale inorganic framework providing a very high surface area, low density, and access for electrolytes to their interior space. This morphology facilitates fast ion transport and electrochemical intercalation/deintercalation reactions since the thickness of the walls is just several nanometers. Thus these aerogels meet most of the necessary requirements and are considered as one of the more suitable cathode materials for future electronic and medical gadgets.

Depending on the preparation conditions, different compositions of  $\text{VO}_x$  survive with various ratios of  $\text{V}^{4+}/\text{V}^{5+}$ . However, to increase the discharge capacity,

vanadium (IV) ions can be oxidized by annealing in air to recycle the  $\text{V}_2\text{O}_5$  phase. Generally, annealing at 100 – 300 °C introduces no changes in the original morphology of the material, maintaining its very high porosity. However, higher temperatures liberate an excess of the free Gibbs' energy of the system and this starts irreversible morphology evolution.

Today, R&D in the field of Li-ion batteries is carried out in Lomonosov Moscow State University by several groups. Materials with different composition



and morphology are studied using the facilities of the Inorganic Materials Laboratory (Department of Materials Science, Chemistry Department), and the Faculty of Materials Science is celebrating its 20<sup>th</sup> anniversary this year. The students of the Faculty have successfully investigated 1D systems with record aspect ratios (nanowires, whiskers), 2D layered structures (xerogels and hybrid materials), as well as 3D systems of aerogels and smart composites all based on mysterious, rich structures of vanadium oxide<sup>4,5</sup>.

The use of the unique equipment available allows the synthesis of aerogels from a wide variety of experimental parameters. For example, the preparation is not limited to a pair of solvents and a simple isothermal heating zone: it is instead possible to vary the pumping and relief velocities of solving, or the sequence of exchanged solvents. It is also possible to control the application and combination of pumping regimes. Thus, aerogels with different morphologies have been formed under conditions controlled and selected by the researcher.

This month's cover image shows an SEM micrograph of an annealed vanadia aerogel. The image was captured using a field emission LEO Supra 50 VP scanning electron microscope. The real size of the image is 52.6 × 34.4 square microns. The sample was obtained by annealing of as-prepared aerogel based on vanadium oxide at 500 °C in air and consists of plate-like particles with boomerang and other complex shapes. We assume that these particles are formed because of a thermally triggered recrystallization and agglomeration processes. The length of the plates is approximately 2 – 10 μm, and the width is about 2 – 5 μm. Outwardly, the sample resembles a randomly scattered puzzle. Although this material has an interesting morphology, its discharge capacity is low due to the destruction of the initial porous structure.

### FURTHER READING

1. Long J. W., et al., *Chem Rev* (2004) **104**, 4463.
2. Dong W., et al., *Science and Technology of Advanced Materials* (2003) **4**, 3.
3. Rolison D. R., et al., *J Mater Chem* (2001) **11**, 963.
4. Balakhonov S. V., et al., *Mendeleev Commun* (2010) **20**, 153.
5. Balakhonov S. V., et al., *Mendeleev Commun* (2011) **21**, 315.



The SUPRA® is a general purpose ultra high resolution FE-SEM based on the unique ZEISS GEMINI® Technology. Excellent imaging properties combined with analytical

capabilities makes this high end FE-SEM suitable for a wide range of applications in materials science, life science, and semiconductor technology. The large specimen chamber for the integration of optional detectors and accessories enables the user to configure the SUPRA® for specific applications without sacrificing productivity or efficiency.

For more information about Carl Zeiss Microscopy and our comprehensive product portfolio ranking from light- and laserscanning microscopes to a uniquely broad electron- and ion beam portfolio, go to [www.zeiss.com/microscopy](http://www.zeiss.com/microscopy).

## FORTHCOMING EVENTS

14 May 2012 - 18 May 2012

**E-MRS 2012 Spring Meeting**

Strasbourg – France

The 2012 Spring Meeting will include 25 parallel symposia, one plenary session, one exhibition and much more.

[www.emrs-strasbourg.com/index.php?option=com\\_content&task=view&id=428&Itemid=160](http://www.emrs-strasbourg.com/index.php?option=com_content&task=view&id=428&Itemid=160)

15 – 18 May 2012

**Biosensors 2012**

Cancun – Mexico

Biosensors 2012 is a three-day event, organized by Elsevier in association with Biosensors & Bioelectronics, consisting of daily plenary presentations followed by parallel sessions comprising a rigorously refereed selection of submitted papers. In addition to invited lectures, selected oral contributions will be included as extended plenary presentations.

[www.biosensors-congress.elsevier.com](http://www.biosensors-congress.elsevier.com)

20 – 24 May 2012

**Glass & Optical Materials Division Spring Meeting**

St. Louis – Missouri, USA

GOMD 2012 highlights state-of-the-art scientific research and application of glass, including fiber optics, encapsulation of nuclear/hazardous wastes, bioglass & biotechnology, super high-strength glasses, and more.

<http://ceramics.org/dates-deadlines/division-event-gomd-2012-glass-optical-materials-division-spring-meeting-2>

23 – 25 May 2012

**Strategies in Tissue Engineering**

Würzburg – Germany

As in 2004 and 2006, the meeting sets out to bring researchers from all over the world together to discuss the latest developments in the rapidly expanding field of Tissue Engineering and Regenerative Medicine. As for the previous conferences, the high level of the scientific program will be determined by more than 30 keynote lecturers, invited from all over the world to present their latest research and clinical results.

[www.wite.org](http://www.wite.org)

23 – 25 May 2012

**Cell Symposia: Genetics and Chemistry Sharing a Language of Discovery**

Cambridge – MA – USA

These days, genome sequencing is becoming cheaper and more accessible by the hour. This wealth of human DNA sequence data offers insight into genomic structure and organization as well as clues to how disease states like cancer alter and are altered by DNA. This meeting will look at interpreting this information, appreciating its implications for basic cellular mechanisms and using this resource to inform therapies to promote human health.

[www.cell-symposia-geneticsandchemistry.com](http://www.cell-symposia-geneticsandchemistry.com)

1 – 5 June 2012

**World Biomaterials Conference**

Chengdu – China

The theme for this congress is "Innovative Biomaterials and Crossing Frontiers in Biomaterials and Regenerative Medicine". The scientific program will feature 81 symposia, 5 workshops, and 3 forums.

[www.wbc2012.com](http://www.wbc2012.com)

3 – 8 June 2012

**Lehigh Microscopy School**

Bethlehem – PA – USA

This course is designed for individuals who use scanning electron microscopy and x-ray microanalysis in academic, governmental, or industrial laboratories: engineers, technicians, physical and biological scientists, clinicians, geologists, forensic scientists and technical managers.

[www.lehigh.edu/microscopy/courses/sem\\_xray.html](http://www.lehigh.edu/microscopy/courses/sem_xray.html)

10 – 13 June 2012

**The 2nd International Conference on Algal Biomass, Biofuels and Bioproducts**

San Diego – California – USA

The 2nd International Conference on Algal Biomass, Biofuels and Bioproducts provides a new level of direct interaction between the leaders in the scientific field, the strategic partners and the attending delegates. Emphasis will be placed on latest unpublished technical and scientific results, discussion and direct interactions with strategic partners and leaders in the field. The conference is designed to facilitate extended discussion periods with dedicated networking sessions.

[www.algalbbb.com](http://www.algalbbb.com)

25 – 29 June 2012

**8th Coatings Science International 2012**

Noordwijk – The Netherlands

Welcome to The Leading European Conference on Coatings Science & Technology. This conference is intended for researchers and research managers, active in the field of Science and Technology of Coatings both from industry and academia.

[www.coatings-science.com](http://www.coatings-science.com)

30 June 2012 – 5 July 2012

**7th International Conference on Materials for Advanced Technologies**

Singapore

The Materials Research Society of Singapore (MRS-S) was created in 1999 as a not-for-profit organization to serve a rapidly emerging materials science community in Singapore. The founding President of the Society was Prof Shih Choon Fong. The Society is affiliated with the International Union of Materials Research Societies (IUMRS).

[www.mrs.org.sg](http://www.mrs.org.sg)

1 – 4 July 2012

**ICEFA V – Fifth International Conference on Engineering Failure Analysis**

The Hague – The Netherlands

The modern innovation cycle now demands that component design involves a whole-of-life approach, incorporating an awareness of manufacture, safety, reliability, environmental sensitivity and disposal. This has focussed attention on the pivotal role of failure analysis as an essential tool to improve equipment availability, help prevent accidents and disasters and to inform the processes of design, manufacture, operation and maintenance of key plant and equipment.

[www.icefaconference.com](http://www.icefaconference.com)

8 – 13 July 2012

**CSM-2012 — International Conference on Science and Technology of Synthetic Metals 2012**

Atlanta – GA – USA

ICSM is the longest-running conference series in the field of conducting and semiconducting organic materials. It started in the mid-1970s with the advent of highly electrically conducting molecular crystals and conjugated polymers (hence, the original reference to synthetic metals!). It has now become a premiere venue for discussion of the latest developments in the areas of organic electronics and photonics, from synthesis to characterization, computational modeling, device fabrication, and real-world applications.

[www.icsm2012.com](http://www.icsm2012.com)

9 – 13 July 2012

**12th International Conference on Inorganic Membranes**

Enschede – The Netherlands

The International Conference on Inorganic Membranes (ICIM) is the premier venue for reporting and discussing the latest developments in the field of inorganic membranes.

[www.icimconference.com](http://www.icimconference.com)

15 – 19 July 2012

**4th International Congress on Ceramics, including 3rd Ceramic Leadership Summit Track**

Chicago – Illinois – USA

ICC4's global platform fosters discussion of and solutions for issues facing the global ceramic and glass communities, thus shaping the future of ceramics.

<http://ceramics.org/4th-international-congress-on-ceramics-icc4>

15 – 17 July 2012

**Colloids and Nanomedicine 2012**

Amsterdam – The Netherlands

Following the successful Colloids and Materials 2011, this second event in the "Colloids" series of conferences will have a focus on the rapidly growing nanomedicine area.

[www.colloidsandnanomedicine.com](http://www.colloidsandnanomedicine.com)

materials**today**

ELSEVIER

Events  
diary

If you are organizing a future conference or workshop and would like to have it listed in *Materials Today* please contact Stewart Bland – [s.bland@elsevier.com](mailto:s.bland@elsevier.com).

Events *Materials Today* has a contra deal with and that are relevant to the current issue of the magazine are listed below.

If, as an organizer, you would like to discuss a contra deal, please contact Lucy Rodzyska – [lucy.rodzyska@elsevier.com](mailto:lucy.rodzyska@elsevier.com)

6 – 10 August 2012

**Denver X-ray Conference**

Denver – Colorado, USA

[www.dxcicdd.com](http://www.dxcicdd.com)

12 – 16 August 2012

**SPIE Optics + Photonics 2012**

San Diego – California, USA

<http://spie.org/x30491.xml>

14 – 18 May 2012

**E-MRS 2012 Spring Meeting**

Strasbourg – France

[www.emrs-strasbourg.com/index.php?option=com\\_content&task=view&id=428&Itemid=160](http://www.emrs-strasbourg.com/index.php?option=com_content&task=view&id=428&Itemid=160)

26 – 30 November 2012

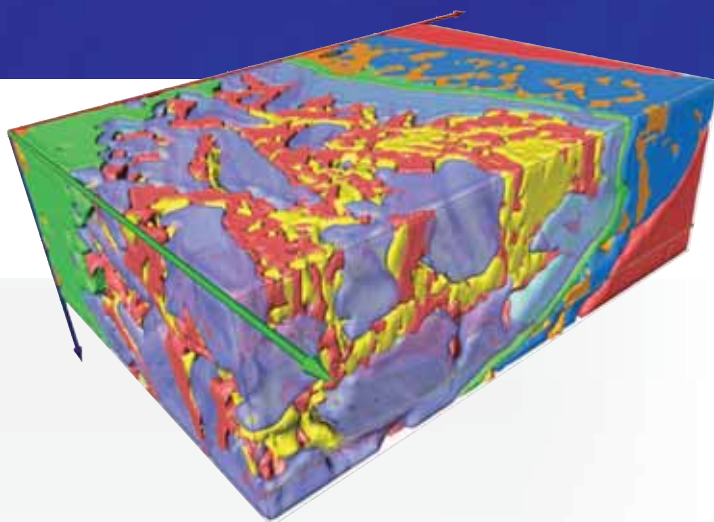
**2012 MRS Fall Meeting & Exhibit**

Boston – Massachusetts, USA

[www.mrs.org/fall2012](http://www.mrs.org/fall2012)

# TOMOGRAPHY

## Add the 3rd dimension to your EDS and EBSD data!



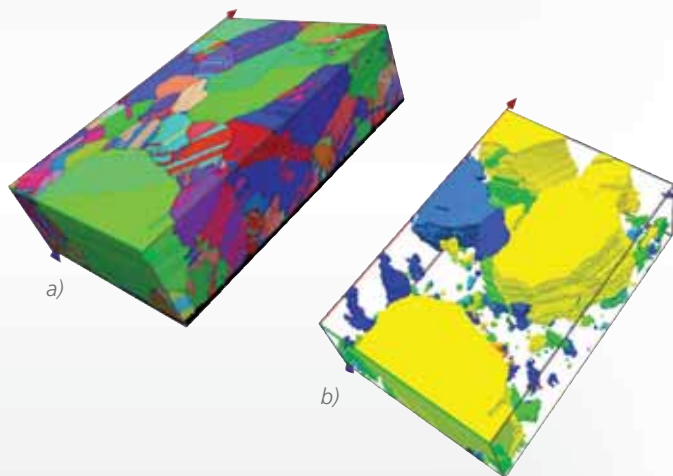
3D EDS data showing different intermetallic phases in the molten region of a NiTi and stainless steel laser weld. Courtesy of P. Burdet, CIME, EPFL.



# 1

### INTEGRATED

Unattended acquisition of 3D datasets of compositional (EDS) and crystallographic (EBSD) data using serial sectioning in a FIB-SEM.



3D EBSD result showing (a) an IPF map and (b) a fibre texture subset in a CdTe layer. Courtesy of Dr. D. Abou-Ras, Helmholtz Zentrum, Berlin.

# 2

### FAST

Rapid data acquisition enabled by large area SDD detectors and fast EBSD cameras.

# 3

### ACCURATE

Reliable results with Oxford Instruments' advanced quantitative and indexing algorithms.



Email: [3Dmicroanalysis@oxinst.com](mailto:3Dmicroanalysis@oxinst.com)

[www.oxford-instruments.com](http://www.oxford-instruments.com)

[facebook.com/oxinst](https://facebook.com/oxinst) • [twitter.com/oxinst](https://twitter.com/oxinst) • [youtube.com/oxinst](https://youtube.com/oxinst)



The Business of Science®



# Publish

## your

results in

PHYSICS

EDITOR-IN-CHIEF

**K.H.J. Buschow**

MANAGING EDITOR

**G. Lupo**

INTERNATIONAL  
ADVISORY BOARD

**M. Baxendale**

**A. Bellosi**

**B. Bokstein**

**F.R. de Boer**

**C.R. Doering**

**W. Fahrenholtz**

**V.V. Kharton**

**X.G. Li**

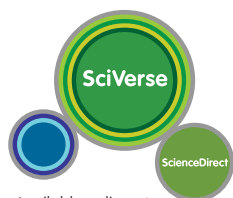
**W. Prellier**

**W. Strek**

**T.G. Woodcock**

**Y.-F. Zheng**

**C. Zollfrank**



Available online at  
[www.sciencedirect.com](http://www.sciencedirect.com)



YOUR PAPER,  
YOUR WAY

SUBMIT NOW AT [www.journals.elsevier.com/results-in-physics/](http://www.journals.elsevier.com/results-in-physics/)